Wavefield methods to analyze passive ocean bottom seismic data

Application to the Tyrrhenian Sea

Dissertation
zur Erlangung des Doktorgrades
der Naturwissenschaften im Fachbereich
Geowissenschaften
der Universität Hamburg

vorgelegt von

Martin Thorwart

aus

Nürtingen

Hamburg

2006

Als Dissertation angenommen vom Fachbereich Geowissenschaften der Universität Hamburg

auf Grund der Gutachten von Prof. Dr. T. Dahm

und Dr. C. Hübscher

Hamburg, den 28.Juni 2005

Prof. Dr. H. Schleicher
(Dekan des Fachbereiches
Geowissenschaften)

Contents

Abstract

In this study different full waveform techniques was developed for the investigation of seismic ocean bottom single station data. These techniques were applied to data obtained in a pilot ocean bottom experiment in the Tyrrhenian Sea/Italy (TySea experiment) from December 2000 to May 2001. A network of broadband seven ocean bottom seismometers and seven ocean bottom hydrophones was installed above the subducting Ionian plate which descends from Southeast to Northwest. Local and teleseismic earthquakes were recorded by the stations. The newly developed techniques produce very promising results in reconstructing the sea floor structure beneath the stations and in attenuating waveform effects generated by water layer multiples. Additionally the techniques offer a possibility to determine the orientation of free fall ocean bottom seismometers. The main results are:

1. The waveform recorded at the seafloor differs from waveforms recorded at land stations. This is primarily due to multiple reflections in the water layer. These multiple reflections show different patterns on seismometer and hydrophone recordings depending on the seafloor structure. This opens the possibility to constrain the P-wave velocity structure beneath the station by means of a full waveform inversion. Seismometer and hydrophone traces of 13 local deep earthquakes were used to resolve the seafloor structure below the single stations of the experiment in terms of P-wave velocity. It was found that the average P-wave velocity of the uppermost gradient layer varies from 1630 m/s to 1690 m/s. The layer itself is 95 m to 190 m thick. The results are well determined and comparable with findings of other studies undertaken in this region of the Tyrrhenian Sea.

2. The multiple reflections of waves in the water layer also influence the analysis of teleseismic events, in receiver function studies or for tomographic studies where relative arrival times are usually estimated by cross correlation techniques. The wavefield decomposition using seismometer and hydrophone traces separates the up- and downgoing wavefield. The effects of multiple reflections can be attenuated and the signal-to-noise-ratio can be improved with a decomposition analysis. As a by-product an in situ calibration of the sensors is possible as well as the estimation of the impedance contrast at the seafloor. The impedance contrast was found to have a value of 1.1 to 1.3. With these improvements the data of land and ocean bottom stations may be combined in future.

3. In the recorded seismograms an energy signal which is mainly horizontal linearly polarized occurs between 0.4 s and 1.2 s after the P-onset from local deep earthquakes. This is interpreted as a converted P to S-wave which is trapped in the upper sediments. This energy signal is used to estimate the orientation of the

ocean bottom seismometer and to resolve the seafloor structure in terms of S-wave velocity. For the TySea experiment the obtained S-wave velocity in the uppermost 10m to 50m deep layer is in the range of 10 m/s to 100 m/s.

Chapter 1

Introduction

1.1 Methods of waveform analysis and approach of this thesis

In this thesis the full waveform of recorded signals is analyzed with waveform methods (WM) in contrast to parameter studies like seismic tomography (e.g. Ritter et al., 2001). WM require broadband data and true ground motion.

WM are commonly used for dealing with two main type of tasks:

1. source studies like centroid moment tensor inversions or source tomography (e.g. Braunmiller et al., 1994) or

2. structural studies to resolve the velocity and density structure beneath single stations (e.g. Ammon et al., 1990).

This thesis presents different WMs for tasks of type 2. One aim is to resolve the velocity structure beneath a ocean bottom station. It concentrates on the upper most layer of the seafloor because it is generally assumed that these layers have a major influence on waveforms which are recorded on ocean bottom stations. The thesis develops and applies models to understand signals which are generated by multiple reflections in the water layer above the station. Additionally parameters like the impedance contrast at the ocean bottom, the thickness of the seafloor mud layer, the orientation of the sensor and the calibration of the hydrophone are estimated by modeling or investigating waveforms.

After a small chapter on important preprocessing steps like data restitution and sensor orientation, the thesis presents three major methods, (1) the modeling of multiple reflections in the water layer, (2) a wavefield decomposition technique and (3) a model to

understand strong and delayed resonating signals on the horizontal components (ringing phases).

The first method presented in chapter 3 follows the approach of modeling the coda waveform after the P-phase onset from deep earthquakes which are recorded on the vertical component of the seismometer and on the hydrophone component. The coda is influenced by multiple reflections in the water layer and in layers beneath the station and its waveform is different for the seismometer and hydrophone channels. The approach is similar to an approach used in reflection seismology which is described by Aki and Richards (1980). Their approach directly resolves the layered velocity structure beneath the ocean bottom station from the waveform data. In this thesis the transitivity instead of the reflectivity is used, since in contrast to reflection seismology the source time function is unknown. A simultaneous inversion of seismometer and hydrophone waveform data of several events is performed to resolve the subbottom structure.

The second method which is presented in chapter 4 applies waveform decomposition to the earthquake data. Waveform decomposition is applied in marine reflection seismology to attenuate disturbances by multiple reflection in the water layer (e.g. Muijs et al., 2004). Relative calibration between hydrophone and seismometer is done and the impedance contrast at the sea floor is estimated. The effect of the wave decomposition is shown for synthetic and real data of local and teleseismic events.

In chapter 5 the third method has the aim to explain ringing phases occurring shortly after the P-phase. They are observed at ocean bottom seismometers during reflection seismology experiments as well as during local earthquakes in the Tyrrhenian Sea. They are horizontal linearly polarized and are explained as a converted P-S-wave. They depend on the shear velocity structure of the subsurface.

For further experiments and studies the work presented in this thesis brings several innovations. The investigation of the coda waveform of the P-wave and the analysis of the ringing phases produces a structural model of the layers beneath a ocean bottom station and of the spatial distribution when using a network. The wavefield decomposition enhances the waveforms and attenuates the effects of the multiple reflections in the water layer. Hence, results from land and ocean bottom stations can be compared and investigation of combined networks are possible. The investigation of the ringing phases provides an alternative method to estimate the orientation of the deployed sensors which is important in various applications.

1.2 Ocean bottom seismometer

Ocean bottom seismometers (OBS) have been used in exploration seismology for more than 30 years. They are typically deployed along profiles (maximum several hundreds of kilometer) for days or a week. Therefore power supply by batteries is not a problem. The sources of seismic sources can be explosions or air-guns which are fired in the water column. These sources are moved along profiles. Typical sampling rates are between 100 Hz and 10000 Hz. Short period sensors are requested and often deployed in external packs.

Figure 1.1: Ocean bottom station type Hamburg. Four glass floating spheres are located in the orange plastic shells. One of the glass spheres contains the seismometer. Datalogger and Battery packs are placed in pressure tubes (blue). Hydrophone, flash light, radio beacon and release transponder are attached to the edges of the frame.

Figure 1.2: Ocean bottom station from GEOMAR, Kiel. A large floating body is located on top of a tripod. The seismometer is placed in an additional glass sphere as an external pack (yellow plastic sphere). Datalogger and Battery packs are placed in pressure tubes. Flash light and radio beacon are attached to top of the floating body.

In recent years passive seismological ocean bottom experiments have received an ever increasing attention. But the sensors and stations which are needed in passive seismology have to meet different demands in contrast to those used in exploration seismology. It is important to have long deployment periods due to the low seismicity rate in most regions. Broadband sensors (0.01 Hz - 50 Hz) are needed to analyze both weak and strong earthquakes and to estimate reliable source parameters.

Broadband stations which were designed in Hamburg for longterm passive seismological experiments were deployed for the first time in the "Tyrrhenian Sea" project for a period of 6 month (Fig. 1.1). Power was supplied by alkaline batteries. The data recorder (SEND GEOLON) and the sensor (PMD 113) have a low power consumption to enable deployments up to one year.

The GEOLON datalogger is especially designed for long term measurements and has a consumption of 250 mW. A large time accuracy is achieved by using two internal clocks: one for the sample rate and the other for the total time. The time drift is less than 1 s in a year, i.e. the time accuracy is better than $3 \cdot 10^{-8}$. In the data analysis the time drift is assumed to be linear in order to correct the time drift. The data recorder has 4 channels, meaning a three-component seismometer and a hydrophone can be used. Each channel has a resolution between 18 and 21 bits depending on the sample rate. The resolution is 21 bits at a sample rate of 5 Hz. It decreases to 18 bits at a sample rate of 50 Hz. In general we use a sample rate of 50 Hz. The signal-to-noise-ratio for a sample rate of 50 Hz is about 100 dB.

The PMD 113 sensor has a consumption of 90 mW. The signal of the sensor is proportional to ground velocity between 0.033 Hz and 50 Hz. The transfer function is provided by the manufacturer (see appx. B and C). The sensor is passively gimbaled. An OAS hydrophone is used as pressure sensor. Parallel to the preamplifier of the hydrophone a resistor is soldered. The transfer function of the system is then a one-pole high-pass. In the Tyrrhenian Sea a resistor of 1 MΩ was used, meaning that the transfer function is a high pass filter with a corner frequency of 1 Hz.

To minimize noise by current and tilt a flat frame for holding the sensors was designed. The frame was 1.40 m long, 1.20 m wide and about 0.60 m high.

In addition to the Hamburg type stations ocean bottom seismometers and ocean bottom hydrophones (OBH) from the marine research institute GEOMAR were deployed (Fig. 1.2). These stations were originally designed for shortterm active marine experiments and were modified to meet the demands of the longterm deployment. They also used the datalogger SEND GEOLON. The sensors were manufactured by WEBB and consisted of a Differential Pressure Gauge (DPG) and a Mark L-4 seismometer. The seismometer was mounted in a glass sphere in an external pack. It had an active leveling.

1.3 The Tyrrhenian sea experiment

All the data which are used in this thesis were collected in the Tyrrhenian sea experiment. Here follows a short introduction to the Tyrrhenian sea experiment.

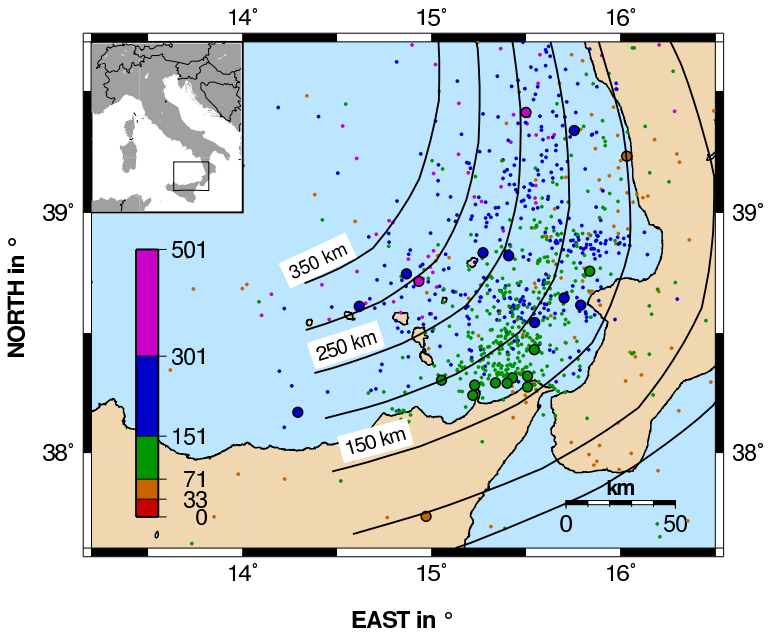

Figure 1.3: Deep seismicity below 50 km since 1981 (small dots) provided from the Istituto Nazionale di Geofiscia e Vulcanologia (INGV,http:waves.ingv.it). Large circles indicate events which occurred during the experiment and are relocated with the combined ocean bottom and land network (Wittwer, 2004). Contour lines indicates the subducting Ionian slab. Event color declare hypocentral depths in km.

The tectonic history of the Tyrrhenian Sea and the Mediterranean Sea is related to collision between the continental plates of Europe and Africa and is complex in its structure. Several mircoplates exist in the Mediterranean Region such as the Adriatic plate, Ionian plate and the Tyrrhenian plate.

The opening of the Tyrrhenian Sea and the creation of the Tyrrhenian oceanic crust began 35 Ma ago (Goes et al., 2004) and has been caused by the rollback of the Ionian subduction. Today the subduction zone is beneath Calabria and dips to the north-west. The volcano in the Aeolian Islands (Lipari, Volcano, Stromboli) are related to the subduction zone. Etna, also located in the region, is however not a typical subduction zone volcano. Deep seismicity in the region images the subduction zone. Earthquakes occur down to a depth of 400 km. Shallow seismicity indicates recent faults like the Volcano fault and Sisifo fault (Neri et al., 1996).

Other important tectonic features are the large sediment basins between the Aeolian Islands and Sicily respectively Calabria: the Celafù and the Giola Basin. Both basins contain more than 1000m of sediment. Continental sediments from the north of Sicily are deposited mainly in the basin (Gennesseaux et al., 1998). Therefore only thin sediment layers exists on the lower continental slope and in the bathyal plain on the other side of

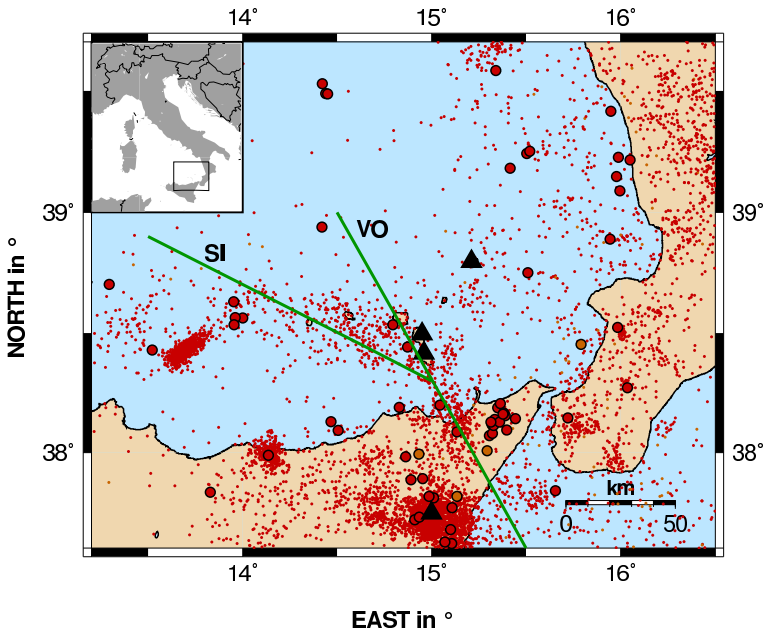

Figure 1.4: Shallow seismicity above 50 km provided from the INGV (http:waves.ingv.it). Large circle indicates events which occurred during the experiment and are relocated with the combined ocean bottom and land network. Black triangles represent active volcano: Etna, Volcano, Lipari and Stromboli. Green lines indicate prominent faults: Volcano fault (VO), Sisifo fault (SI). Prominent features of seismicity are at Etna in the south, the Volcano-fault on a line south-west of Volcano, the Sisifo fault in the west of the Aeolian Islands and two clusters, one at at 38.0N and 14.1E and one at 38.5N and 13.7E.

the Aeolian Islands.

7 ocean bottom seismometer and 7 ocean bottom hydrophones were installed from December 2000 to May 2001 around the Aeolian island north of Sicily (Fig. 1.5). OB07, OB08, OB10 and OB11 were Hamburg type ocean bottom seismometer and OB05, OB06, OB14 ocean bottom seismometer from GEOMAR. All ocean bottom hydrophones were from GEOMAR. The stations formed a triangular array fitting in the gap between the Italian peninsula and Sicily. The ocean bottom seismometer continuously recorded ground motions between 0.03 and 15 Hz at a sampling rate of 50 Hz on four channels (e.g. Dahm et al., 2002, 2004). The ocean bottom stations were deployed in the region of the sediment basins as well as at the lower continental slope and the bathyal plain.

About 88 earthquakes were recorded on the OBS-network and were able to be relocated with the combined ocean bottom and land station network (Wittwer, 2004). Localizations are listed in appx. D. The largest earthquake which occurred during the deployment was a Ml=4.4 earthquake on the 4th of January 2001 at a depth of 320 km. The

majority of the deep seismicity occurred at depths between 50 and 150 km north-west of the Straight of Messina.

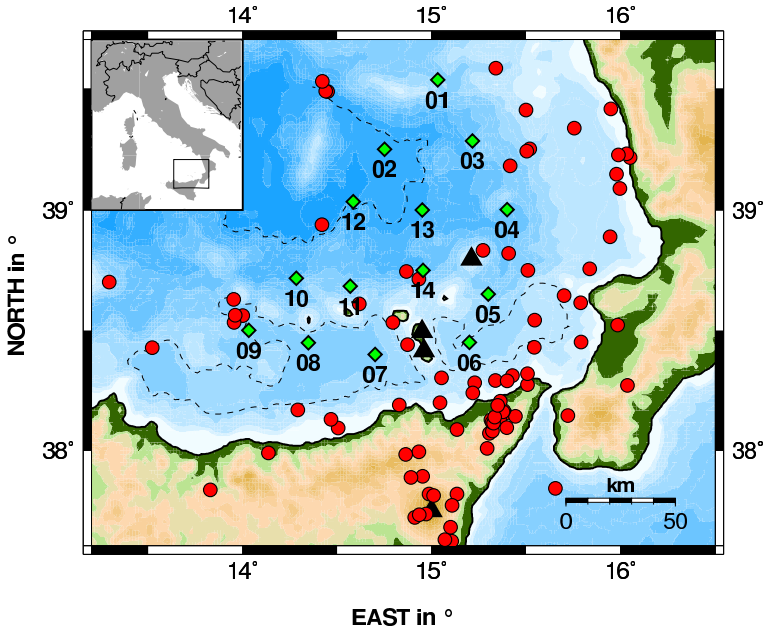

Figure 1.5: Temporary ocean bottom network, deployed from December 2000 until May 2001. **Green diamonds**: OBS/H stations. **Black triangles**: volcano. **Red circles**: earthquakes (Dec. 2000 - 05.2001). **Dashed lines**: border of the sediment basins and the bathyal plain.

Chapter 2

Characterization and orientation of the sensors

2.1 Transfer function of the sensors

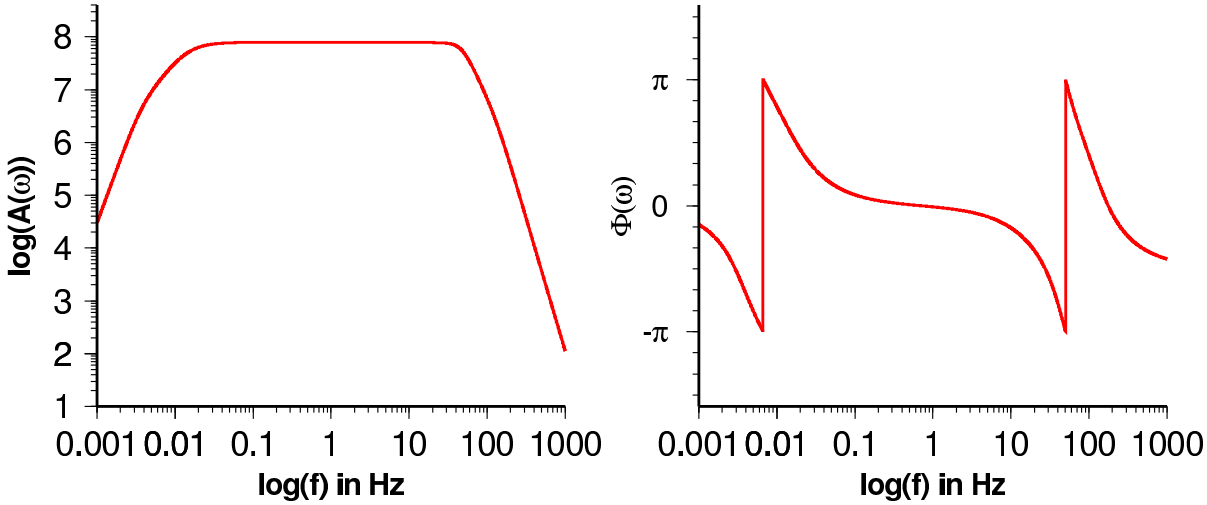

Figure 2.1: Amplitude and phase spectra of the transfer function of the PMD seismometer. Amplitude are in (counts/(m/s))/Hz

The output of the data recorder are digital counts and not true ground motion. The sensor modifies the ground motion by a filter described as impulse response (time domain) or transfer function (frequency domain). The transfer function of the sensor is frequency dependent. It is important for a lot of applications to have real ground motion data. Therefore the OBS data are restituted, i.e. the impulse response is deconvolved.

Data sheets with the transfer function of the seismometer (Fig. 2.2) are commonly given by the manufacturer. However, when comparing our measurements with those of nearby

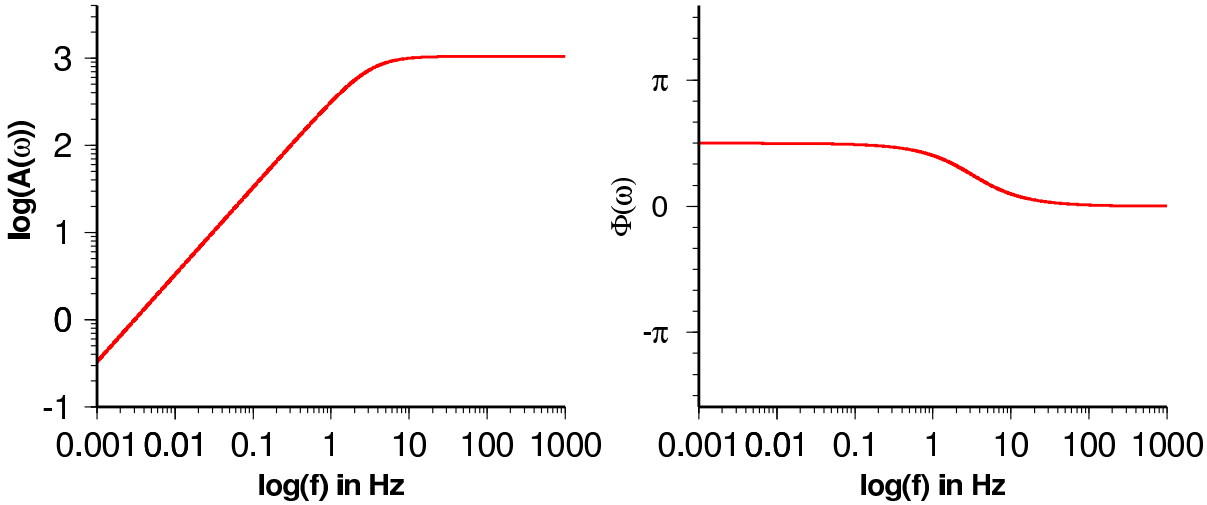

Figure 2.2: Amplitude and phase spectra of the transfer function of OAS hydrophone. Amplitude are in (counts/Pa)/Hz

land stations, we noticed that amplitudes are possibly not correct. Therefore a calibration measurement of the sensors has been performed (appx. B).

The hydrophone data have also to be restituted to pressure for further analysis of the waveform. The transfer function of the OAS hydrophone (Fig. 2.2) is derived from theoretical estimations (appx. B).

We restituted the data in frequency domain by our own programs. To avoid numerical instabilities due to the devision of the small amplitudes of the transfer function at low frequencies a high pass filter with a corner frequency at 0.01 Hz has been applied.

Raw and restituted data of the 26.Jan 2001, Mw=7.7 India earthquake are shown in Fig. 2.3 as an example . The restituted traces of the seismometer show relatively strong amplitudes at low frequencies. This is because restitution to ground displacement resembles integration of seismogram. Raw hydrophone and pressure data are similar because both are velocity proportional. But amplitudes below 1Hz are increased on the pressure traces. Therefore surfaces waves are recognizable on the pressure traces but not on the raw hydrophone traces. There are also some indication of numerical instabilities on the pressure traces in Fig 2.3.

More examples can be found in Dahm et al. (2002); Thorwart and Dahm (2005); Polster (2004); Dahm et al. (2004)

2.2 Orientation of the seismometer

The ocean bottom seismometer are free fall units as described before. Therefore it is impossible to control the orientation of the seismometer. Knowing the orientation of the

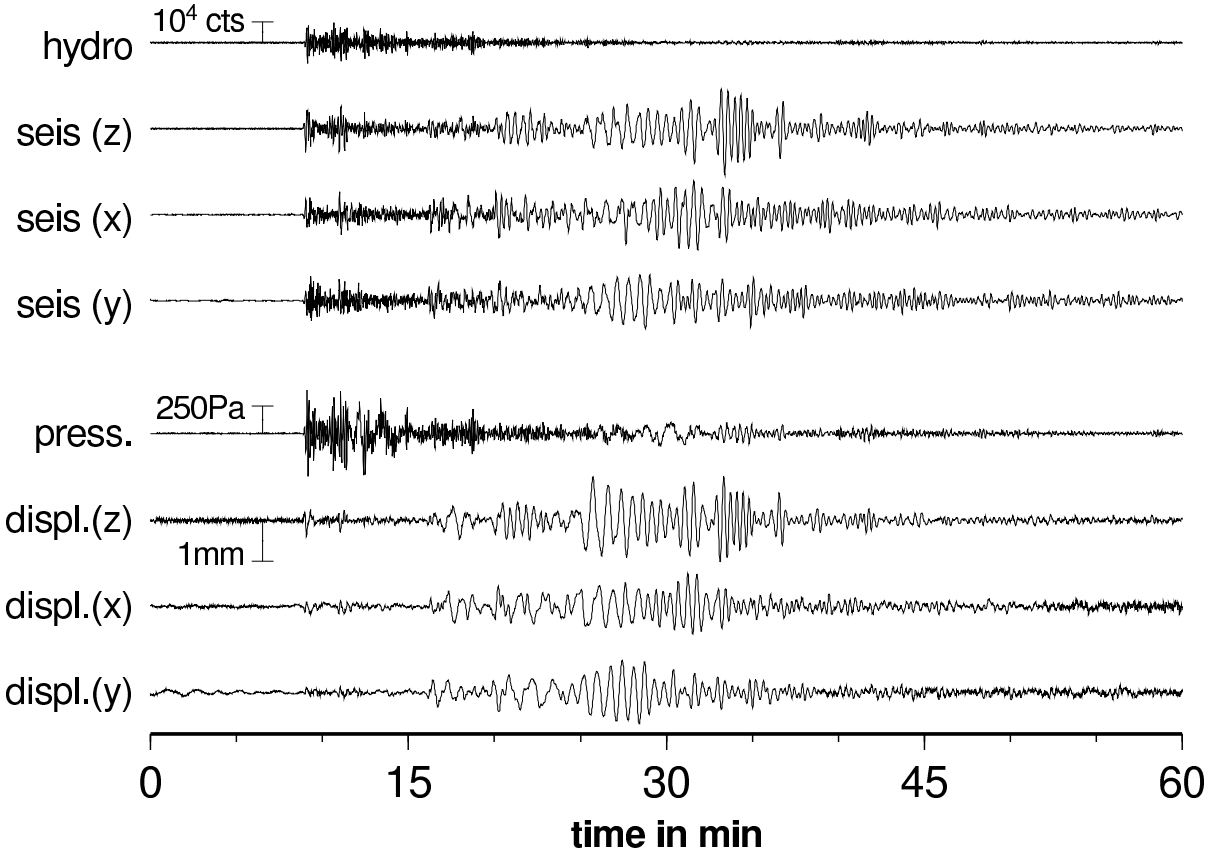

Figure 2.3: Data from 26.Jan 2001, Mw=7.7 India earthquake. **Top**: raw data in counts (cts). **Bottom**: restituted data. Pressure in Pa and displacement in mm.

sensor is important for a lot of geophysical applications like receiver functions, localization etc.. The orientation problem is divided in two parts: the vertical component and the two horizontal components.

2.2.1 Vertical component

The vertical components is in the direction of the gravitation of the earth. There are two ways to level one component into the vertical direction. Either an active leveling of the sensor is done, e.g. in intervals of days or weeks (e.g. GEOMAR OBS). The advantage is that the sensor is mechanically fixed to the glass housing during no-leveling terms. The disadvantages are the additional need of power supply, the necessity of a sophisticated leveling system and the impossibility of reaction to slow or continuous tilt.

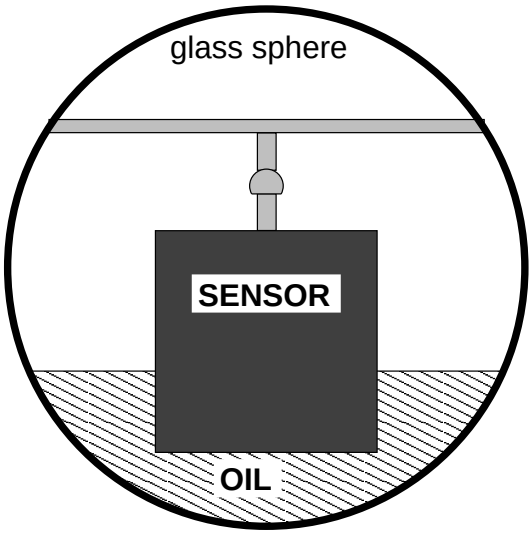

Figure 2.4: The Sensor is gimbal-mounted in the glass sphere. It hangs in a high-viscous oil.

Another method is to have the sensor passively gimbal-mounted in a highly-viscous oil. This is realized in the ocean bottom seismometer of the University of Hamburg (Fig. 2.4). After the relaxation time of some minutes the sensor has moved into the vertical position. The oil reacts at low frequencies like a fluid, at higher frequencies like an elastic medium. For the Tyrrhenian Sea deployment a oil with an dynamic viscosity of 160 Pa s and a kinematic viscosity of $1.6 \cdot 10^5$ cSt has been used leading to a relaxation time of more than 100 s. The measured frequency of influence is about 0.02 Hz (Miensopust, personal. communication). The advantage of the passive leveling is prompt reaction to any slow tilt. The sensor will reorient itself into the vertical direction. A disadvantage is that this construction acts like a high-pass filter with the reciprocal relaxation time as corner

frequency. Horizontal signals with a period in the range of the relaxation time or larger will be attenuated by the viscous reaction of the oil. Depending on the viscosity of the oil seismological signal are not affected by the reaction of the oil.

2.2.2 Horizontal components

There are different methods to determine the orientation of the horizontal components .

First of all it would be possible to add a calibrated compass to the instrumentation of the ocean bottom seismometer and measure the direction of north. Resolution of such a compass may be about ten degree (Osler and Chapman, 1998).
For the Tyrrhenian Sea Project no compass was used. We determined the orientation estimating the polarization of body wave phases from earthquakes and comparing the apparent back-azimuth with the real back-azimuth of events. Different methods using body and surface waves have been compared.

Figure 2.5 shows a sketch how the orientation is determined. The real back-azimuth β is the angle between the great circle of the event and the North direction. The apparent back-azimuth γ is the angle between the great circle and the Y-direction of the sensor. The orientation α is the difference between real and apparent back-azimuth $\beta - \gamma$. The real back-azimuth can be calculated by the event and station coordinates. In both cases, teleseismic and local events, a one-dimensional layered underground model is used. For the apparent back-azimuth the fact is used that P-phases and Rayleigh-waves are polarized in direction of the great circle between the event and the station. The 180°ambiguity is not resolved. Data need not to be restituted as long as the components have the same transfer function.

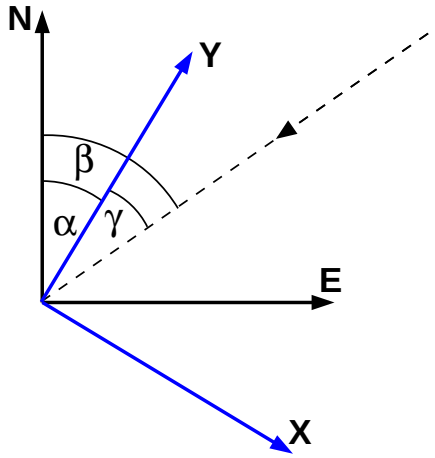

Figure 2.5: Orientation of the horizontal components: N, E are the geographical axes, Y, X the sensor components, dashed line is the great circle of an event. The orientation α is the difference between real and apparent back-azimuth $\beta - \gamma$.

Rectilinearity

Montabetti and Kanasewich (1970) designed a filter to determine the polarization of a body-wave and the rectilinearity of a 3-component seismogram with N samples. They define the covariance matrix V by:

$$V_{ij} = \frac{1}{N}\sum_{k=1}^{N}(X_{ik} - \bar{X}_i)(X_{jk} - \bar{X}_j) \tag{2.1}$$

X_{ik} is the k-th sample of the i-th component, $\bar{X}_i$ is the mean of the i-th component, defined by:

$$\bar{X}_i = \frac{1}{N}\sum_{k=1}^{N} X_{ik} \tag{2.2}$$

The main diagonal of the matrix gives the variance of each component. The matrix is symmetric and positive definite,

$$V_{ij} = V_{ji} \tag{2.3}$$

. The system of the principle axes for the matrix represents the particle motion of the seismogram. The eigenvector which belongs to the largest eigenvalue represents the polarization. All eigenvalues are positive, $\lambda_i \geq 0$. The unit of the eigenvalue is the square of the unit of the traces, e.g. $counts^2$ if the seismograms are in *counts*. If λ_1 is the largest eigenvalue and λ_2 the second largest one the dimensionless rectilinearity function R is defined as:

$$R(\lambda_1, \lambda_2) = 1 - \left(\frac{\lambda_2}{\lambda_1}\right)^n \tag{2.4}$$

The constant n can be any positive number. The value of 1 and 0.5 is often used for n. In this thesis n = 0.5 is used. The rectilinearity function varies between 0 and 1. If the signal is nearly linear polarized, λ_1 is much larger than λ_2 and the rectilinearity function is nearly 1. If the signal has no polarization, the eigenvalues are similar to each others and the rectilinearity function is close to 0.

Data

Different waves generated by earthquakes can be used to determine the polarization, i.e. body waves (P- and converted Ps waves) as well Rayleigh-wave. Common to both types of waves is that their polarization is in the direction of the great circle.

Teleseismic P-phases

The P-Phase is the first arrival in a seismogram. Therefore the particle motion is not disturbed by other phases. The rectilinearity method should derive the apparent back-azimuth. When using teleseismic events low frequencies are dominant. Then the particle motion is weekly disturbed by a local 3D-structure. The real back-azimuth is also not so sensitive to a mislocation of the event. However only few signals from teleseismic events with good signal-noise ratio can be used.

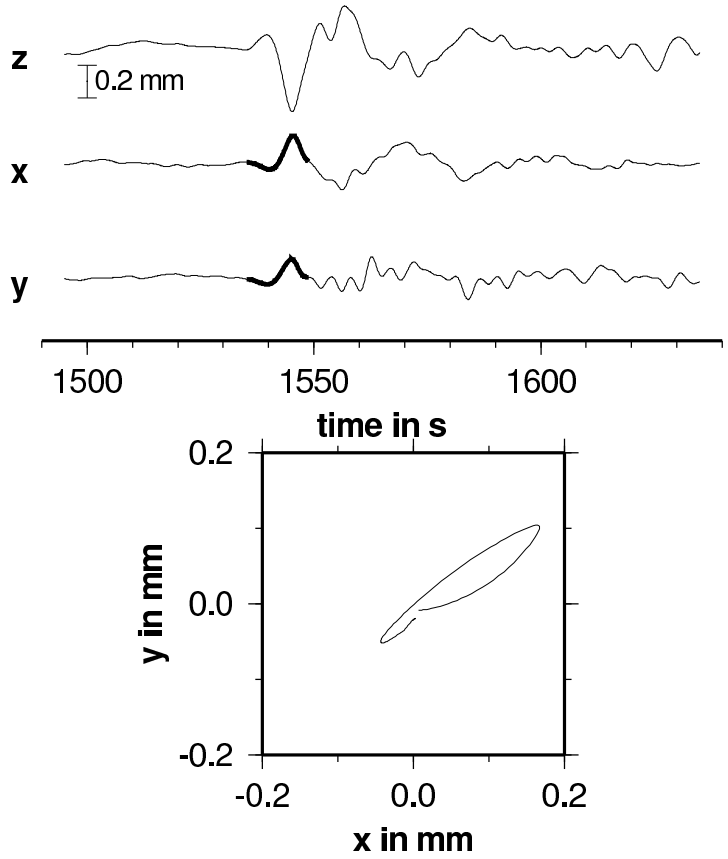

Figure 2.6: **Left**: P-phase of the 26.Jan 2001, Mw=7.7 India earthquake recorded on station OB10. Data is bandpass-filtered between 0.01 Hz and 0.3 Hz. Thick lined data is used to determined the orientation. **Right**: Particle motion plot of the P-phase.

Teleseismic surfaces-waves

It is not possible to estimate the sensor orientation from teleseismic surface waves by the rectilinearity approach because Love- and Rayleigh-waves cannot be easily separated. A synoptic approach is used instead. The horizontal components were rotated in 10 degree

steps and plotted with the vertical component. The Rayleigh wave is elliptically polarized in the vertical plane and there has the same amplitude envelope on the vertical and the radial component. The Love wave has a different group velocity and therefore a different amplitude envelope compared to the Rayleigh wave. It differs from the envelope of the love wave. The apparent back-azimuth of the earthquake is determined by a visual comparison of the amplitudes on the rotated traces and on the vertical component.

Ringing-phases

An additional, new approach which is developed in this thesis is to analyze the polarization of coda waves which follows the P-arrival. The coda energy after the P-onset occurs a few of seconds after the arrival time of the P-phase. It has relatively strong amplitudes on the horizontal components and a dominant frequency between 2 Hz and 7 Hz. Due to this description it is sometimes called ringing phase. The ringing phase is interpreted as a converted Ps-phase which is polarized in the radial-vertical plane (for a more detailed description see chapter 5). The ringing phases are best observed for local earthquakes which have a mean frequencies > 1 Hz. Because the inclination angle of the Ps-ray is small, the ringing phase has a large horizontal component. Hence, the ringing phases from local earthquakes can be used to estimate the orientation of the sensor by the method of the rectilinearity. Thresholds for $\lambda_1 = 10000$ cts^2) and rectilinearity R $= 0.5$ are applied.

Results

For each station a preselection for events with a good signal-to-noise ration (SNR) is done. Therefore, the number of used events varies between the stations. Because of the large noise on the horizontal components the station OB05 and OB08 have been excluded. The rose-diagrams in Fig. 2.9 -2.11 show the distribution of the estimated orientations. A 180°ambiguity of the orientation cannot be resolved. Therefore, every determined angle of orientation α and the opposite angle $\alpha + 180°$ are plotted. Each orientation value has been weighted by its rectilinearity to enhance data from linearly polarized waves.
Mean value and standard deviation for the distributions are calculated and compared in table 2.1with the orientations from the other methods. The Standard deviation of the orientation derived from the surface waves are larger than the given values in table 2.1. The standard deviation here does not regard the measurement error of about 10°.

However, the results of the three approaches for OB06, OB10 and OB11 are consistent within the one standard deviation range.

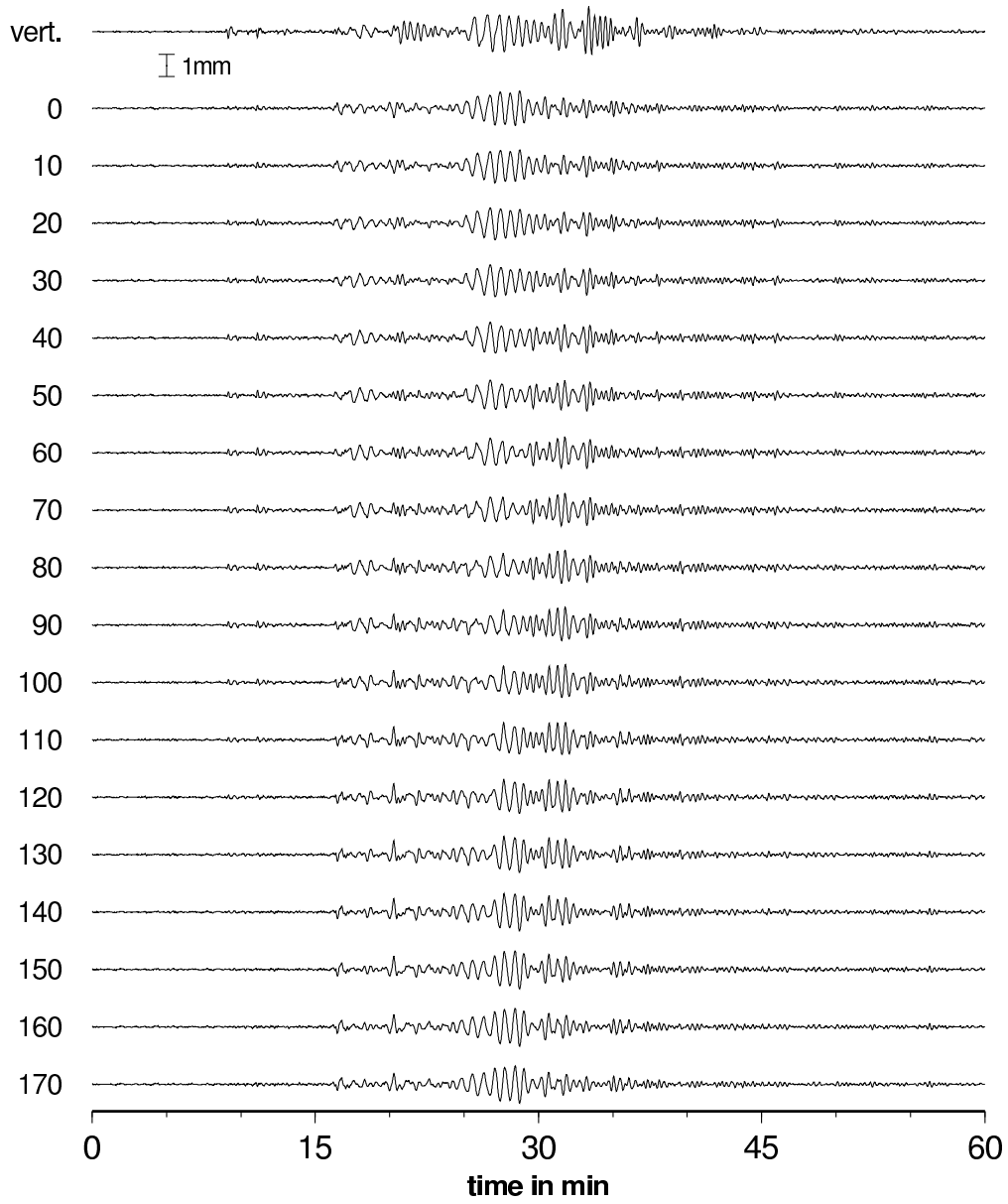

Figure 2.7: Example for estimation of the orientation using teleseismic surface waves. Rotated traces of the 26.Jan 2001, Mw=7.7 India earthquake recorded on OB10. Data is bandpass-filtered between 0.017 Hz and 0.1 Hz Time in minutes is after source time of the event. **Top**: vertical component. **Bottom**: rotated horizontal components in 10 degrees steps.
Surface waves are strong between 25 min and 40 min. Amplitude pattern between 40°and 60°is most similar to amplitude pattern on the vertical component.

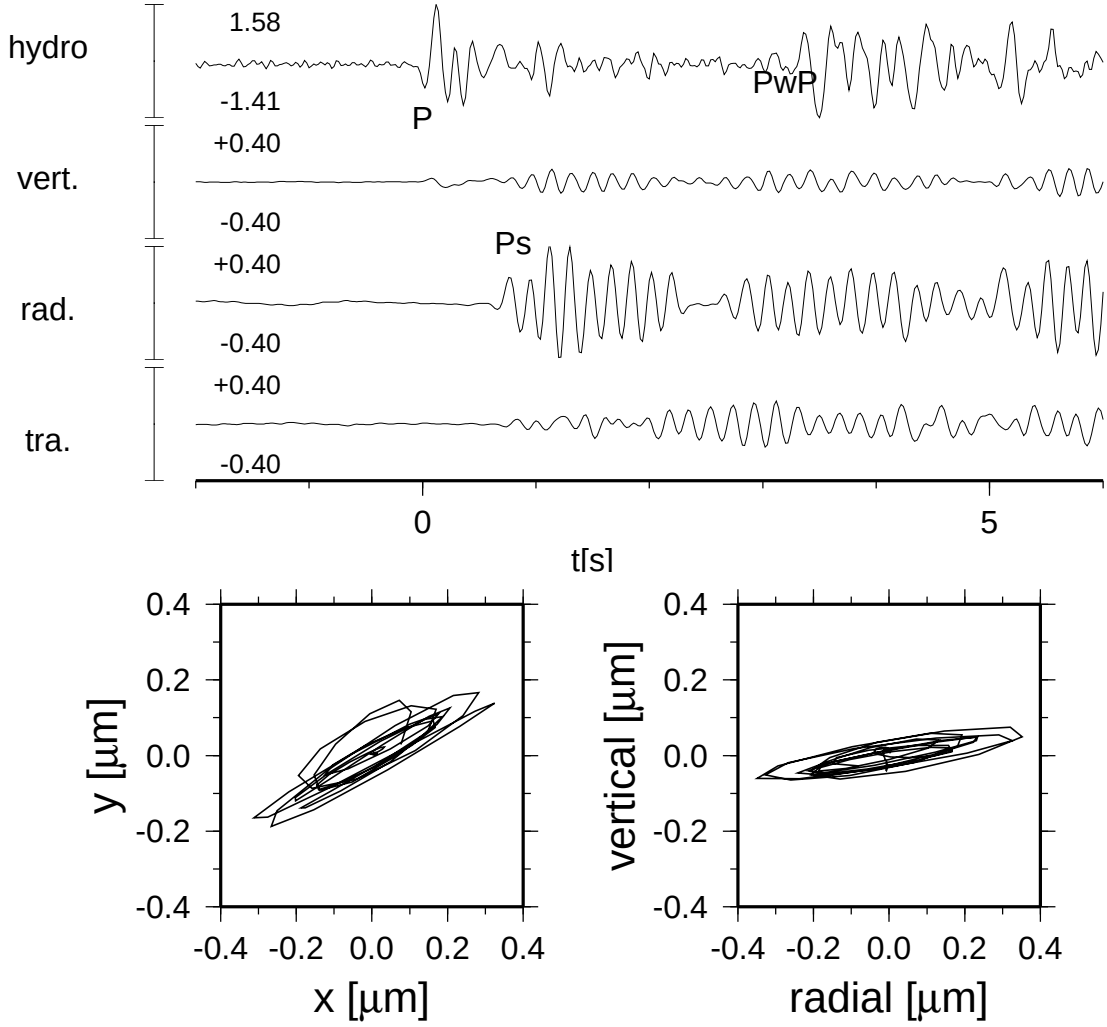

Figure 2.8: Example of a Ringing phase. Data of 07.12.2000, Ml 1.6 earthquake are recorded on OB10. **Top:** pressure trace in Pa (hydro) and displacement trace in μm (vertical, radial and transversal). Horizontal displacement is rotated in a radial and transversal component thus the energy of the Ringing phase is minimal on the transversal component. **Botton left:** horizontal particle motion. **Bottom right:** particle motion in the radial-vertical plane.

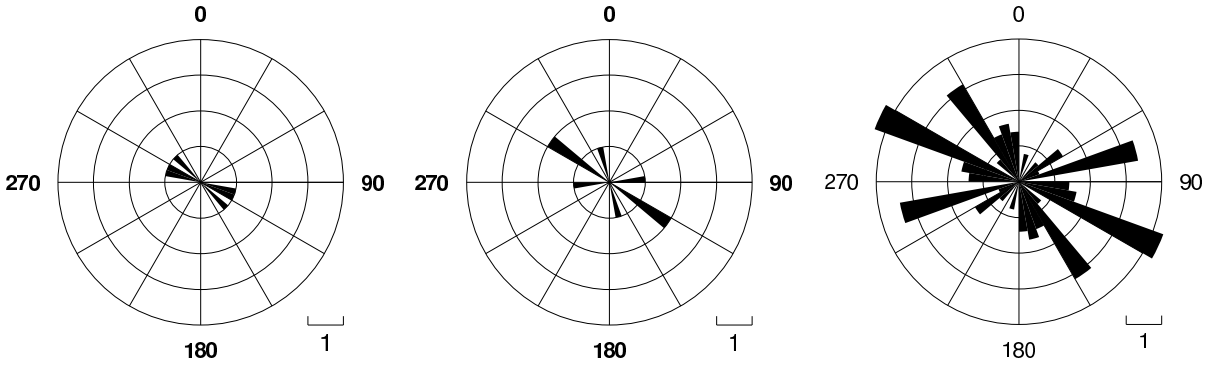

Figure 2.9: Results for OB06. **Left**: teleseismic P-phase (3 events). **Middle**: teleseismic surface-waves (4 events). **Right**: Ringing-phase (32 events).

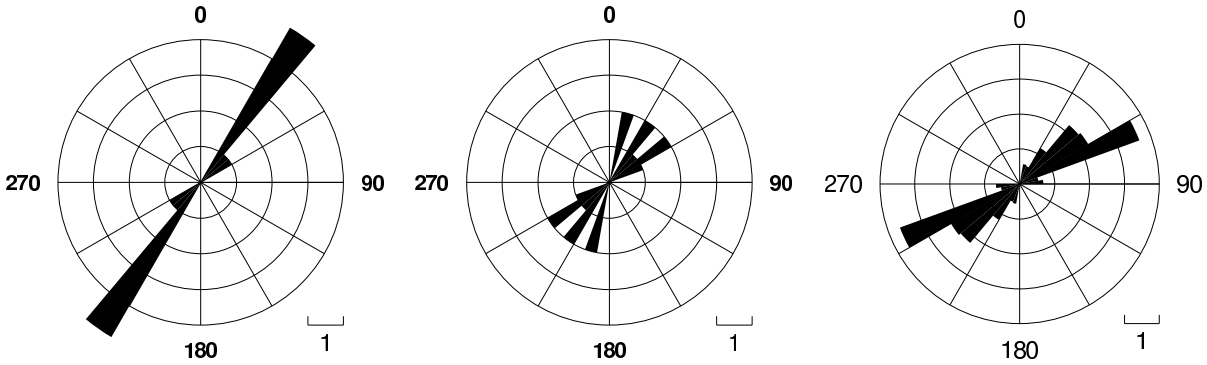

Figure 2.10: Results for OB10. **Left**: teleseismic P-phase (7 events). **Middle**: teleseismic surface-waves (8 events). **Right**: Ringing-phase (17 events).

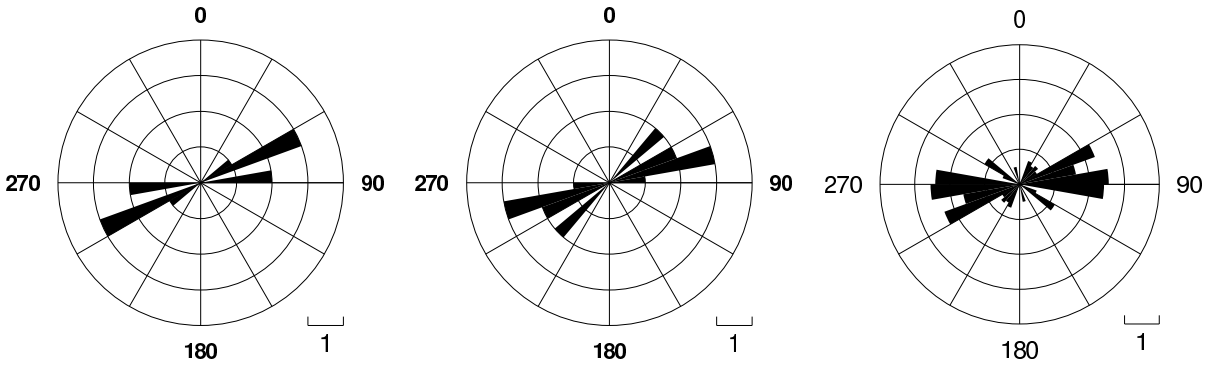

Figure 2.11: Results for OB11. **Left**: teleseismic P-phase (6 events). **Middle**: teleseismic surface-waves (8 events). **Right**: Ringing-phase (23 events).

The orientation of the sensors derived from Ringing Phase seem to have some systematic effects. Especially OB06,(Fig. 2.9) three dominant sectors are recognizable: 70°-80°,110°- 120°and 140°- 150°.

A large standard deviation of the distribution could be caused by mislocations of the event. Station OB06 is located near to the epicenter of the local events (see Fig 1.5). A small mislocation means then has a large effect on the back-azimuth β. The locations-error are not taken into account in the estimation of the orientation α.

Another effect is the non-consideration of 3D-structure of the underground. All three stations are located at the transition from continental to oceanic crust. The depth of the Moho decreases to the north. There is also the dipping slab which influences the wave propagation, especially for deep events. But there are also shallow structures: station OB06 is additional located in a sediment basin.

The real back-azimuth β is calculated with a 1D-model. In a 3D-model the ray-path differ from the ray path of the 1D-model. Therefore a incorrect estimation of the orientation is possible.

In Fig. 2.12 the real back-azimuth and the polarization of the Ringing phases of earthquake northeast of OB06 are plotted. There is a systematic shift towards the subduction zone. The orientation estimated from these events are between 50°and 80°.

If available a 3D-model of the region should be considered to calculate correct back-azimuths for local events.

Table 2.1: Results of the three different orientation analysis, i.e. from the teleseismic P-phase, from the ringing phases of the local earthquakes and from the teleseismic surface waves. For each station and approach mean value and one standard deviation is given. Number of events which were used in the analysis are given in brackets.

Station	P-phase	Ringing-phase	surface-wave
OB05	$50° \pm 22°$ (3)	-	-
OB06	$119° \pm 13°$ (3)	$117° \pm 41°$ (31)	$123° \pm 34°$ (4)
OB08	$28° \pm 44°$ (3)	-	-
OB10	$39° \pm 7°$ (7)	$53° \pm 19°$ (17)	$39° \pm 18°$ (8)
OB11	$70° \pm 13°$ (6)	$81° \pm 30°$ (23)	$65° \pm 15°$ (8)

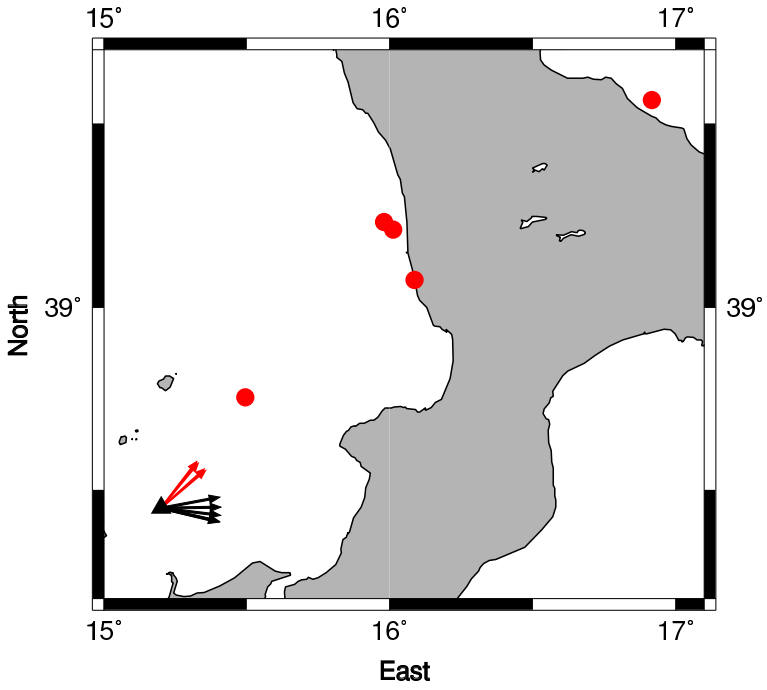

Figure 2.12: Real back-azimuth (red arrows) of selected events northeast of OB06 and polarization (black arrows) of the occurred Ringing phase.

Chapter 3

Multiple reflections in the water layer

In exploration seismology water layer multiples are well know. They have large amplitudes because of the large impedance contrast between water and basement. Water layer multiple reflection can also be seen on the OBS data in the Tyrrhenian sea (Figure 3.1). In passive seismology they are named PwP phases. While primary PwP phases have sharp sort and a large amplitude, second or higher multiple onsets are difficult to see in Fig 3.1.

In active seismic exploration multiple reflections are often attenuated by applying a normal-move-out (NMO) correction. First onset phase are superposed constructively but multiples destructively. In passive seismology, however, event or station number are often limited so that extensive stacking techniques are not possible. Therefore, single trace techniques and modeling approaches are of interest.

The delay time between the P- and PwP-phase depends on the depth of the ocean and the incidence angle of the incoming wave. The relative amplitudes between the P- and PwP-phase depends on the impedance contrast between water and seafloor. Therefore, modeling of waveforms can be useful to constrain the subsurface structure beneath the station.

The knowledge of the incidence angle of a ray arriving at a station, i.e. the ray parameter would be a benefit to locate earthquakes. In the first part of the chapter the question is discussed whether ray parameters can be estimated by the delay time between P-phase and multiple reflections. A careful analysis shows that the amplitude and the polarization of the PwP onset differ for the seismometer and the hydrophone. This is due to the different boundary conditions for displacements and pressure. For example the

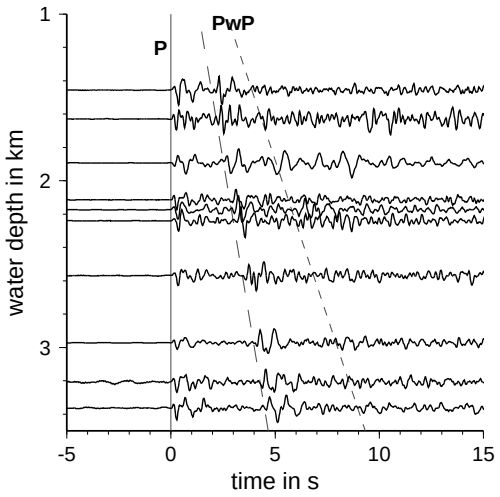

Figure 3.1: Record section of the deep 4th Jan. 2001 earthquake. The hydrophone traces restituted to pressure are plotted over the depth of the ocean. Solid line indicates the P-phase, long-dashed lines indicate the theoretical onset of the first multiple phase PwP in the water, short-dashed line of the second multiple.

reflection coefficient at a free surface has for displacement the value of 1 and for pressure the value of -1. The effect of the water layer and subsurface structure on seismometer and hydrophone traces is studied in the second part of this chapter. In a third part a simultaneous inversion of waveforms on seismometer and hydrophone is used to derive the subsurface velocity model of two stations.

3.1 Time-offset of the PwP-phase

The ray parameter $p = \sin(i_o)/\alpha_o$ depends on the takeoff-angle i_o and the P-velocity α_o in the local region of the earthquake and stays constant along the travel path. It is equal to the reciprocal P-velocity for horizontally propagating waves ($i = 90°$). The ray parameter constrains therefore the hypocenter of an earthquake. It is useful next to P-S travel time differences and depth phases to estimate the depth of an earthquake.

A way to estimate the ray parameter at a single station is by measuring the direction of the incoming longitudinal P-wave from amplitudes. However, this approach is not very stable at land stations and even more difficult at noisy ocean bottom stations. For ocean bottom stations another approach which uses time differences is possible.

The two-travel-time (TWT) of the PwP depends on the incidence angle i of the P-wave in the subbottom, the P-velocity and the depth of the ocean. Because P- and PwP-phase

have clear onsets it would be more reliable to measure the time difference between the PwP- and the P-phase and to calculate the ray parameter from the time difference.

Is this possible and how accurate is this estimate?

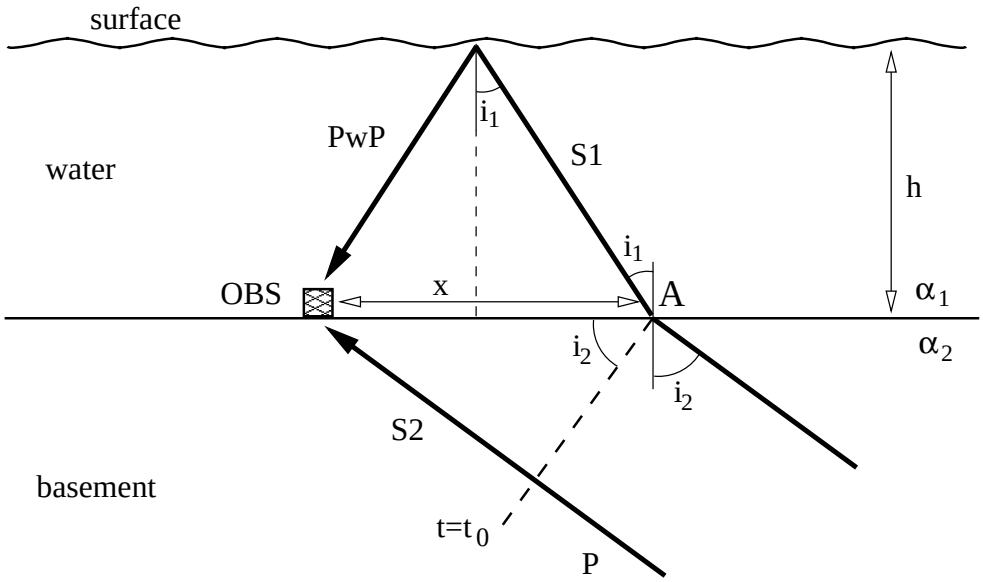

Figure 3.2:
The P-wave arrives from below under an inclination angle i_2. At point A the P-wave refracts in the water layer under the angel i_1. The dashed line indicate the plane wave front at the time of the refraction ($t = t_0$). S2 is the distance between the wave front at the time of the refraction and the OBS, S1 is the two-way-path (up and down) traveled of the PwP-phase after the refraction.

The time difference between P- and PwP-arrival times is (Fig 3.2):

$$\begin{aligned} \Delta t &= t_{\mathrm{PwP}} - t_{\mathrm{P}} \qquad (3.1) \\ &= (t_{\mathrm{PwP}} - t_0) - (t_{\mathrm{P}} - t_0) \\ &= t_{\mathrm{S1}} - t_{\mathrm{S2}} \\ &= \frac{\mathrm{S1}}{\alpha_1} - \frac{\mathrm{S2}}{\alpha_2} \qquad (3.2) \end{aligned}$$

t_0 is the arrival time of the P-wave at the refraction point A. The length S1 and S2 can be written as:

$$\begin{aligned} \mathrm{S1} = \; & 2 \cdot (x/2) \,/\, \sin(i_1) = \; x/\sin(i_1) = 2h/\cos(i_1) \qquad (3.3) \\ \mathrm{S2} = \; & x \cdot \sin(i_2) \end{aligned}$$

i_1 is the incidence angle in the water layer, i_2 in the basement. A plane wave front is assumed. Inserting both relations in equation 3.2 yields:

$$\Delta t = \frac{x}{\alpha_1 \sin(i_1)} - \frac{x \sin(i_2)}{\alpha_2} \qquad (3.4)$$

Using Snellius' law for the relation between the inclination angle i_2 and the refraction angel i_1:

$$\frac{\sin(i_2)}{\alpha_2} = \frac{\sin(i_1)}{\alpha_1} \tag{3.5}$$

the equation is transformed in:

$$\Delta t = \frac{x}{\alpha_1 \sin(i_1)} - \frac{x \sin(i_1)}{\alpha_1} \tag{3.6}$$

x can be written as:

$$x = 2\mathrm{h} \cdot \tan(i_1)$$

where h is the thickness of the water layer.

Inserting this in equation 3.6 yields :

$$\begin{aligned}
\Delta t &= \frac{2\mathrm{h}\tan(i_1)}{\alpha_1 \sin(i_1)} - \frac{2\mathrm{h}\tan(i_1)\sin(i_1)}{\alpha_1} \\
&= \frac{2\mathrm{h}}{\alpha_1}\left(\frac{\tan(i_1)}{\sin(i_1)} - \tan(i_1)\sin(i_1)\right) \\
&= \frac{2\mathrm{h}}{\alpha_1}\left(\frac{1}{\cos(i_1)} - \frac{\sin^2(i_1)}{\cos(i_1)}\right) \\
&= \frac{2\mathrm{h}}{\alpha_1}\frac{1-\sin^2(i_1)}{\cos(i_1)} \\
&= \frac{2\mathrm{h}}{\alpha_1}\frac{\cos^2(i_1)}{\cos(i_1)} \\
&= \frac{2\mathrm{h}}{\alpha_1}\cos(i_1)
\end{aligned} \tag{3.7}$$

The time difference depends only on the water depth h and the P-velocity in water α_1 and the incidence angle r in the water layer. For vertical incidence the time difference is $2\mathrm{h}/\alpha_1$. For non-vertical incidence the TWT in the water layer increases with $1/\cos(i_1)$ (equation 3.3) but the time difference between P and PwP decreases with $\cos(i_1)$ (equation 3.7).

How large is the variation of the time difference between PwP and P for passive seismological recordings?

The range of the incidence angle i_1 in the water layer is limited by the range of ray parameter. The maximum ray parameter p is controlled by the maximum P-velocity α along the ray path: $p = \sin(i_1)/\alpha_1 = \sin(i)/\alpha_p \leq 1/\alpha_{\max}$.

For example a local earthquake occurs in the lower crust with a velocity of $\alpha = 6.5$ km/s. The ray parameter ranges from 0 s/km to 0.1538 s/km and the incidence angle i_1 in water from 0° to 13.3° assuming a water velocity α_1 of 1.5 km/s. The time difference between P and PwP at a station in 2 km depth ranges between 2.67 s (vertical ray) and 2.60 s (horizontal ray at source). The maximum variation of the time difference between P and PwP is less than 3 per cent.
For deep events or events with a P_n-phase as a first arrival the maximum value of the ray parameter is smaller than in the example above because the P-wave travels through the mantle, where α is at least 8 km/s. Therefore the delay time varies between 2.65 s and 2.67 s. This means a variation less than 1 per cent.

In the Project "Tyrrhenian Sea" OBS stations with a sampling rate of 50 Hz were deployed, i.e. their sampling interval was 0.02 s. That means that for deep events and events with P_n as a first arrival the time difference between P and PwP varies only about one sample. The time difference between the P-phase and a nth multiple water reflection onset would be n-times the time difference between P and PwP (n is here the order of multiples). And thus the variation would be larger than one sample. But as the data show (Fig. 3.1) is only the first multiple water reflection PwP is strong and Easy to measure. Higher multiple water reflection are hardly recognizable.

Therefore it is hard to determine the incidence angle and the ray parameter out of the time difference. However, sampling OBS data with 250 Hz should allow reliable estimates of ray parameter in areas with a water depth larger than 2000 m.

3.2 The Modeling of PwP-phases

As mentioned above the multiple reflections produce different patters on seismometer and hydrophone traces. This pattern depends not only on the depth of the ocean but also on the impedance contrast at the seafloor and the seafloor structure. In order to study this pattern a reflectivity code was written to calculate synthetic seismograms for OBS stations. It calculates seismograms for both displacement and pressure seismograms. It is obvious that mainly shallow structures have an important influence on the pattern of multiple reflections. Therefore it is assumed that the source is below the layered media. For deep earthquakes below the station network, as in our case, vertical incidence can be assumed. The reflectivity methods assume a layered media. If the layering is horizontal, there is no conversion between P-and S-waves and it is adequate to simulate only P-waves. This is the reason why a plane wave front is assumed.

3.2.1 Relation between the pressure and displacement of an elastic plane P-wave

Only a P-wave produces a pressure signal since a shear wave is transversal polarized.

A harmonic plane P-wave is given by (e.g. Lay and Wallace, 1995):

$$\Phi(\vec{x},t) = B \cdot \exp(i(\omega t - \vec{k}\vec{x})) \tag{3.8}$$

$\Phi(\vec{x},t)$ is the displacement potential field of the P-wave, B the amplitude, $\omega = 2\pi f$ the angular frequency, t the time, $\vec{k} = \begin{pmatrix} k_x \\ k_y \\ k_z \end{pmatrix}$ the wave number and $\vec{x} = \begin{pmatrix} x \\ y \\ z \end{pmatrix}$ the spatial coordinates. The propagation velocity is $\alpha = \omega/|\vec{k}|$.

The ground motion $\vec{u}(\vec{x},t)$ of the P-wave is the gradient of the displacement potential field.

$$\vec{u}(\vec{x},t) = \nabla\Phi(\vec{x},t) = -i\vec{k}\, B \cdot \exp(i(\omega t - \vec{k}\vec{x})) \tag{3.9}$$

The pressure P is calculated by the trace of the stress tensor:

$$P = -(\sigma_{xx} + \sigma_{yy} + \sigma_{zz}) \tag{3.10}$$

The use of Hooke's law and the insertion of the displacement potential field (equation 3.8) of a P-wave for spatial derivatives of ground motion leads to the following formula:

$$\begin{aligned} P &= -(\lambda + 2\mu)\Delta\Phi = -(\lambda + 2\mu)\,(u_{xx} + u_{yy} + u_{zz}) = \\ &= -\rho\alpha^2\,(i^2(k_x^2 + k_y^2 + k_z^2)\, B \exp\left[i(\omega t - \vec{k}\vec{x})\right] \\ &= +\rho\alpha^2\, k^2\, B \exp\left[i(\omega t - \vec{k}\vec{x})\right] \end{aligned} \tag{3.11}$$

The temporal derivative of ground motion is the ground velocity $\vec{v}(\vec{x},t)$:

$$\begin{aligned} \vec{v}(\vec{x},t) = \frac{\partial\vec{u}}{\partial t} &= -i^2\, \vec{k}\, \omega\, B \exp\left[i(\omega t - \vec{k}\vec{x})\right] \\ &= \frac{\vec{k}}{k}\,\frac{\omega}{k}\, k^2\, B \exp\left[i(\omega t - \vec{k}\vec{x})\right] \\ &= \vec{n}\, \alpha\, k^2\, B \exp\left[i(\omega t - \vec{k}\vec{x})\right] \end{aligned} \tag{3.12}$$

with $\vec{n} = \frac{\vec{k}}{k}$ the normalized propagation vector standing perpendicular to the wave front. The length of $\vec{n}$ is 1.

The comparison of equation 3.11 and 3.12 yields the following relationship between pressure and ground motion:

$$P = \rho\alpha\, \vec{n}\, \frac{\partial \vec{u}}{\partial t} = \rho\alpha\, \vec{n}\, \vec{v}(\vec{x}, t) \tag{3.13}$$

Equation (3.13) shows that the pressure of a P-wave is proportional to the ground velocity. The scaling between pressure and ground velocity is the impedance $I = \rho\alpha$.

3.2.2 Reflectivity method for vertical plane waves and seafloor stations

For a vertical incidence the wave number vector can be simplified to a scalar:

$$\vec{k} = \begin{pmatrix} 0 \\ 0 \\ k_z \end{pmatrix} \tag{3.14}$$

As from now on the scalar k means k_z and $k = 2\pi/\lambda$ where λ is the wavelength. In this case the plane wave depends only on the spatial coordinate z and is independent of x and y.

The ground motion $\vec{u}(\vec{x}, t)$ of the P-wave (equation 3.9) is then:

$$\begin{aligned} \vec{u}(z,t) &= -ik_z\, B \cdot \exp(i(\omega t - k_z z)) \\ &= A(\omega) \cdot \exp(i(\omega t - k_z)) \end{aligned} \tag{3.15}$$

The amplitude of the ground motion $A = -ik_z\, B$ dependents generally on the angular frequency. Therefore $A(\omega)$ is used in stead of $-ik_z\, B$

An integration over all harmonic waves, i.e. over the angular frequency, yields the general description of a plane P-wave:

$$\begin{aligned} \vec{u}(z,t) &= \int_{-\infty}^{\infty} A(\omega) \cdot \exp\left[i(\omega t - k_z z)\right] d\omega \\ &= \int_{-\infty}^{\infty} A(\omega) \exp(-ik_z z) \cdot \exp(i\omega t) d\omega \end{aligned} \tag{3.16}$$

The second equation of 3.16 represents the inverse Fourier transformation of $\vec{u}(z, t)$. $A(\omega) \exp(-ik_z z)$ is the spectra of $\vec{u}$. $A(\omega)$ is the spectra at the depth z=0 and $\exp(-ik_z z)$ is the phase shift due to the propagation of the wave from the depth 0 to z.

In order to model the wave propagation in a layered media we use the reflectivity approach (Müller, 1969):
In each layer wave propagation can be described by two P-waves (equation 3.16), one is

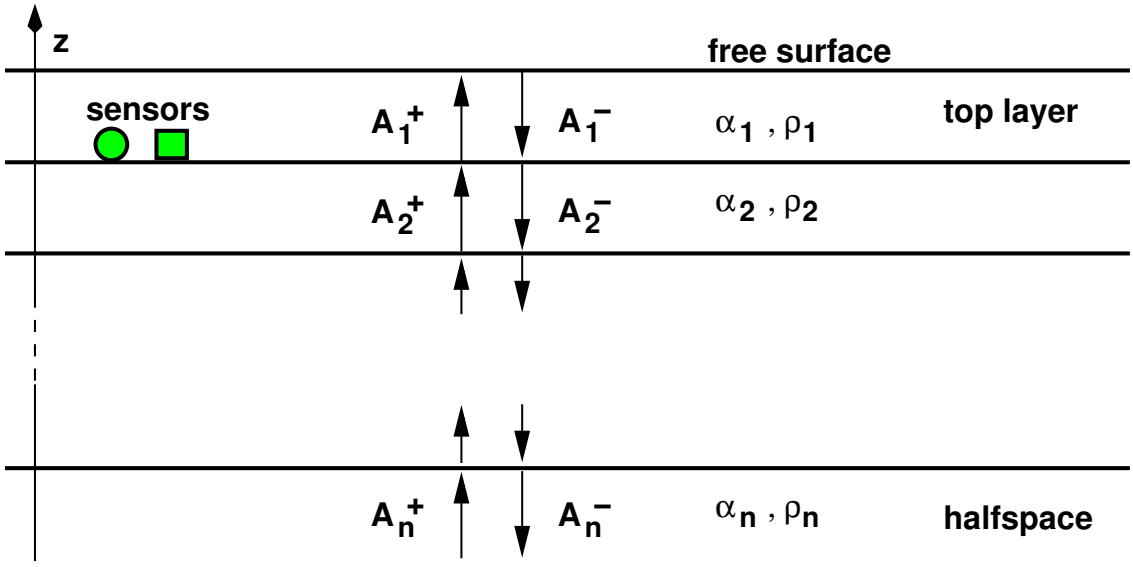

Figure 3.3: Sketch of the reflectivity method.

propagating in z-direction and the other one in $-z$-direction. This is expressed in the different sign of the $k_z z$ term. The reference depth of each layer is the depth of the upper boundary z_{l-1}.
The wave propagation in each layer is the superposition of the both waves:

$$\begin{aligned} u_l(z,t) &= \int_{-\infty}^{\infty} A_l^+(\omega)\, exp\left[i(\omega t - k_z(z - z_{l-1}))\right] \\ &\quad + A_l^-(\omega)\, exp\left[i(\omega t + k_z(z - z_{l-1}))\right] d\omega \end{aligned} \tag{3.17}$$

z_{l-1} is the depth of the upper boundary of the $l-th$ layer, α_l is the P-velocity in the $l-th$ layer, $u_l(z,t)$ is the ground motion in the depth z ($z_{l-1} < z \leq z_l$) at the time t, $A_l^+(\omega)$ and $A_l^-(\omega)$ are the amplitude of the upgoing and downgoing waves at the reference depth z_{l-1}. In general A is complex including amplitude and phase of the travelling waves.

In order to calculate a synthetic seismogram for the sensors in layer 1, the complex amplitudes of layer 1 $A_1^+(\omega)$ and $A_1^-(\omega)$ must be related to the amplitude of the incoming wave, i.e. to $A_n^+(\omega)$.

Through the introduction of boundary conditions complex amplitudes between the top layer and the half space are related to each other (see also appx. A) :

$$\begin{pmatrix} A_1^+ \\ A_1^- \end{pmatrix} = \begin{pmatrix} M_{11} & M_{12} \\ M_{21} & M_{22} \end{pmatrix} \begin{pmatrix} A_n^+ \\ A_n^- \end{pmatrix} \tag{3.18}$$

The reflection coefficient at the free surface is:

$$R_{surface} = \frac{A_1^+}{A_1^-} = -1$$

$$\Longleftrightarrow \qquad A_1^+ = -A_1^- \tag{3.19}$$

The amplitude A_n^- can now be expressed as a function of A_n^+:

$$\begin{pmatrix} A_1^+ \\ -A_1^+ \end{pmatrix} = \begin{pmatrix} M_{11} & M_{12} \\ M_{21} & M_{22} \end{pmatrix} \begin{pmatrix} A_n^+ \\ A_n^- \end{pmatrix}$$

$$\Rightarrow \qquad 0 = (M_{11} + M_{21}) \cdot A_n^+ + (M_{12} + M_{22}) \cdot A_n^-$$

$$\Leftrightarrow \qquad A_n^- = \frac{M_{12} + M_{22}}{M_{11} + M_{21}} A_n^+ \tag{3.20}$$

The equation system 3.18 can then be written as a function of A_n^+:

$$\begin{pmatrix} A_1^+ \\ A_1^- \end{pmatrix} = \begin{pmatrix} M_{11} & M_{12} \\ M_{21} & M_{22} \end{pmatrix} \begin{pmatrix} 1 \\ \frac{M_{12}+M_{22}}{M_{11}+M_{21}} \end{pmatrix} A_n^+ \tag{3.21}$$

where all values are complex and frequency-dependent.
The insertion of equation 3.21 in equation 3.17 yields the inverse Fourier transformation for the ground motion in the top layer (reference depth $z_{l-1} = z_0 = 0$ (surface)):

$$\begin{aligned} u_1(z,t) &= \int_{-\infty}^{\infty} A_1^+(\omega)\, exp\left[i\left(\omega t - k_z z\right)\right] + A_1^-(\omega)\, exp\left[i\left(\omega t + k_z z\right)\right] d\omega \\ &= \int_{-\infty}^{\infty} \left(M_{11} + M_{12}\frac{M_{12} + M_{22}}{M_{11} + M_{21}}\right) A_n^+(\omega) \\ &\qquad \left\{exp\left[i\left(\omega t - k_z z\right)\right] - exp\left[i\left(\omega t + k_z z\right)\right]\right\} d\omega \end{aligned} \tag{3.22}$$

where $z_0 = 0 < z \leq z_1$ and z_1 is the depth of the ocean.

During the study of the waveform of deep earthquakes the spectrum of the incoming wave of each event is assumed to represent to the upgoing wave ($A_n^+(\omega)$) in the lower half space. $\left(M_{11} + M_{12}\frac{M_{12}+M_{22}}{M_{11}+M_{21}}\right)$ is the transfer function of the layered media.

In order to derive the equation for the pressure in the top layer equation 3.13 is applied to equation 3.22:

$$P_1(z,t) = \alpha_1\rho_1 \int_{-\infty}^{\infty} \left(M_{11} + M_{12}\frac{M_{12}+M_{22}}{M_{11}+M_{21}}\right) i\omega A_n^+(\omega) \{exp\left[i\left(\omega t - k_z z\right)\right] + exp\left[i\left(\omega t + k_z z\right)\right]\} d\omega \quad (3.23)$$

where $z_0 = 0 < z \leq z_1$ and z_1 is the depth of the ocean.

Note the switch of the sign of the wave traveling in "$-z$"-direction. The pressure is the sum of up- and downgoing wave, ground motion is the difference between up- and downgoing wave. This is due to different types of sensors: a hydrophone is a isotropic sensor, a seismometer a directional one.

OBS and OBH stations are located at the seafloor. Thus the pressure and displacement measured by the stations are $P_1(z = z_1, t)$ and $u(z = z_1, t)$.

In order to study the pattern of the multiple reflections synthetic seismograms are calculated for three exemplary models.

3.2.3 Water layer above a half space

A simple model is a water layer above a half space (see tab. 3.1). The synthetic seismograms for vertical incidence and P-waves are shown in Fig. 3.6. The time scale is relative to P-onset. A regular pattern of onsets can be seen on both, pressure and vertical displacement trace. The onsets of multiple reflections occur with a period of the two way time $TWT = 2 * h/\alpha_w \approx$3.5 s (see also section 3.1). The main difference between the pressure and vertical displacement trace is the amplitudes and polarity of the first water reflections (see also Webb (1998)). This is due to the fact that a seismometer is a directional sensor whereas the hydrophone an isotropic one. Therefore the reflection coefficient is different for seismometer and hydrophone at the sea level and at the sea floor.

Table 3.1: one layer over half space model.

	thickness	P-velocity	density
water layer	3 km	1.5 km/s	1.0 g/ccm
half space		2.5 km/s	2.0 g/ccm

The P-wave is coming from below, transmits into the water layer, is then reflected at the sea level and reaches the OBS from above as the first water reflection PwP. The polarity of PwP depends on the reflection at the sea level, the amplitude of PwP depends, however, on the reflection at the sea floor. At the sea level the reflection coefficient is -1. The

direction of the first motion changes in respect to the wave propagation. A wave with a compressive onset would change into a wave with a tensile onset. Because the direction of the wave propagation changes also at the reflection at the sea level the direction of first motion does not change in respect to absolute motion (see Fig. 3.4). Therefore pressure shows a reverse polarization of the first water reflection relative to the P-phase, but the vertical displacement shows the same polarization.

The amplitudes of the first reflection depend on the reflection at the sea floor (see Fig. 3.5). In the case that the impedance of the subbottom is larger than the impedance of the water, the reflection coefficient at the sea floor $R_{seafloor}$ is positive with regard to a wave arriving from above the sea floor (like PwP). The station does not only record the arriving PwP-wave but also the reflected wave. As the reflection coefficient is positive the polarization of the PwP does not change in respect to the direction of the wave propagation. Therefore, the hydrophone does not measure the amplitude of the incoming wave but an amplitude multiplied with $(1 + R_{seafloor})$. The direction of first motion changes for the vertical displacement. Therefore, the vertical seismometer measures the difference between the incoming and reflected wave. The amplitude is $(1 - R_{seafloor})$ relative to the P-wave amplitude.

For the multiple reflections in the water layer the geometry is the same as the first water reflection. Therefore, the patterns are similar for the hydrophone and the seismometer. The polarity changes and the amplitudes decreases with the order of the reflections (see Fig. 3.6).

3.2.4 Three layer above a half space

In order to discuss the influence of sediment layers on the recordings a more complicated model was used to calculate synthetic seismograms. The model consists of a water layer, a first thin subbottom layer, a second thick subbottom layer and a half space (see tab. 3.2).

Table 3.2: Three layer model over half space.

	thickness	P-velocity	density
water layer	3.0 km	1.5 km/s	1.0 g/ccm
1th layer	0.1 km	1.6 km/s	1.6 g/ccm
2th layer	1.4 km	2.5 km/s	2.0 g/ccm
half space		4.4 km/s	2.5 g/ccm

Reflections from the tick subbottom layer are visible both, after the P-wave and the

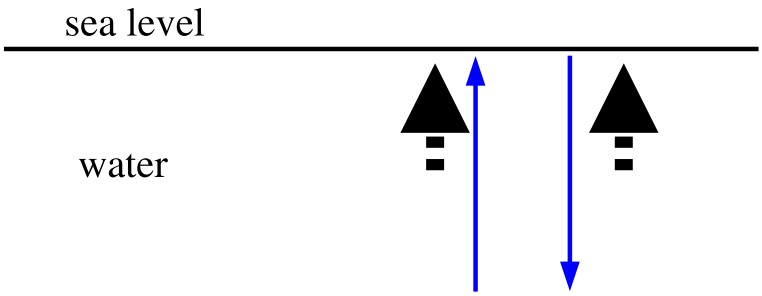

Figure 3.4: Reflection of P-wave at the sea level. Long blue arrows indicate the direction of the wave propagation for upgoing (left) and reflected waves (right) and thick black arrows indicate the first motion. The first motion changes in respect to the direction of wave propagation, but not in respect to the absolute motion.

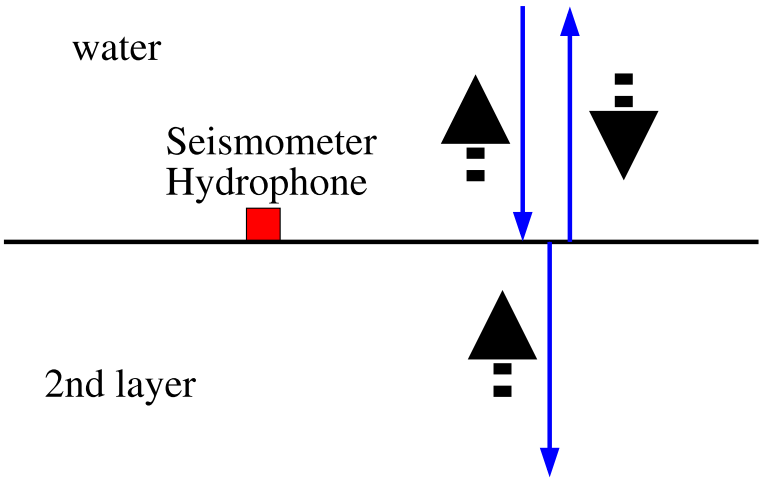

Figure 3.5: Reflection of the PwP-phase at the seafloor for an impedance contrast larger than 1. Long blue arrows indicate the direction of the wave propagation for the upgoing (left) and reflected waves (right) and thick black arrows indicate the first motion. The first motion does not change in respect to wave propagation, but in respect to the absolute motion.

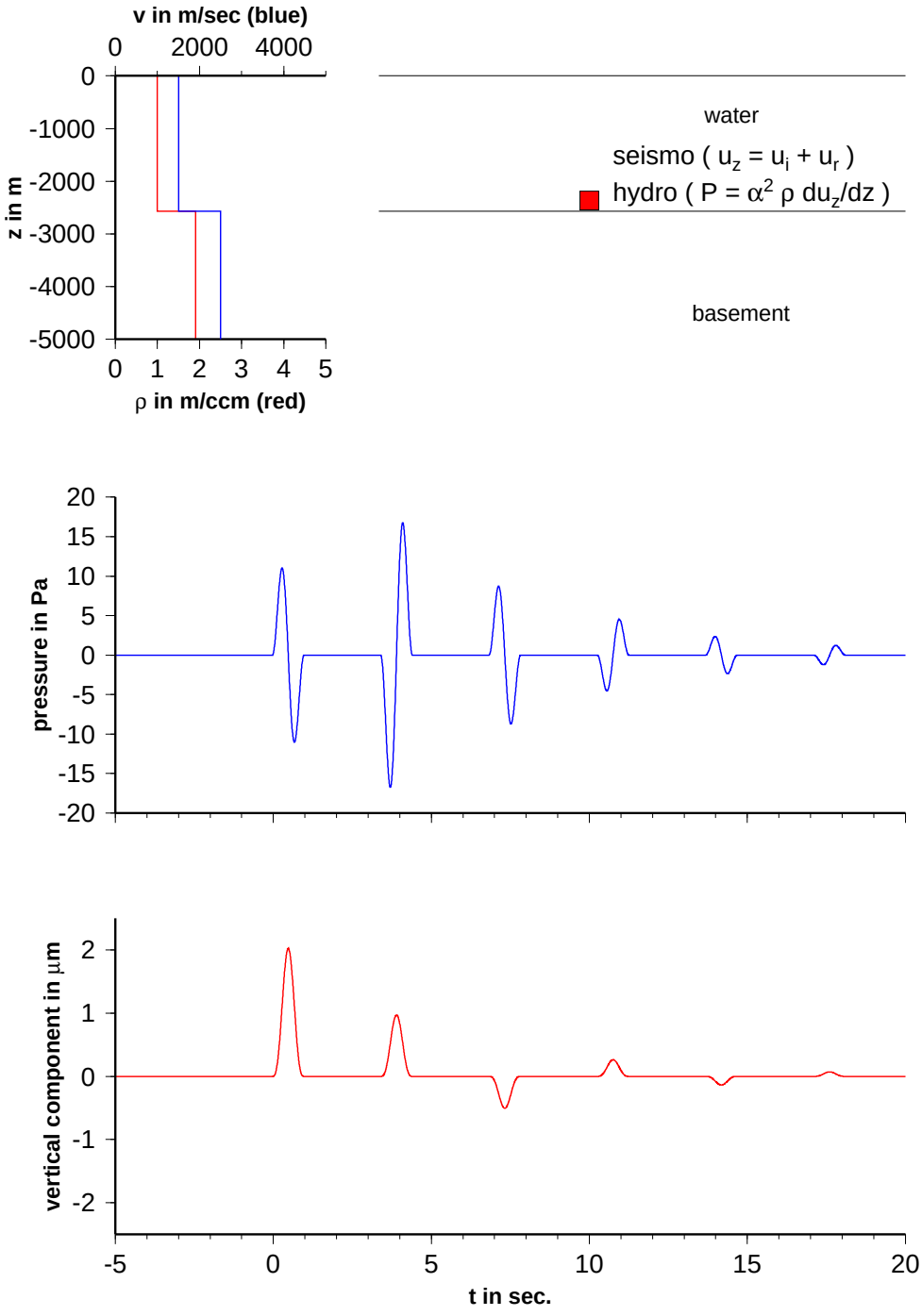

Figure 3.6: One layer over half space model: **Top**: model of the subsurface. Water depth corresponds to OBS OB10. **Middle**: synthetic seismogram for pressure. **Bottom**: synthetic seismogram for vertical ground motion.

multiple reflections in the water layer (see Fig. 3.8). The patterns of the reflections in the subbottom layer are equal after the P-wave for pressure and vertical displacement but differ after the multiple reflections in the water layer. The reflections of the subbottom layer after the first water reflections PwP are in general larger on the seismometer than on the hydrophone. The reflections of the subbottom layer are larger on the hydrophone than on the seismometer after the second water reflection PwwP.
This is due to the fact that there is more than one ray path. The first reflection of the subbottom layer after the PwP has two possible ray paths: firstly the reflection in the water layer and secondly the reflection in the subbottom layer and vice versa. The travel time of these two ray paths is the same. Therefore the arrival time of the waves is the same, but one wave is coming from above, the other one from below. Depending on the polarity the two waves superpose destructive on the hydrophone and constructive on the seismometer. The amplitude differs for both ray paths. The amplitude of the red ray path is: $A_{red} = R_{SW}R_{RH}T_{SW}R_{surface}$. For the other one is $A_{blue} = T_{SW}R_{surface}T_{WS}R_{SH}$ applicable. (see Fig. 3.7). R_{XY} means that a wave is traveling in X and is reflected at the interface to Y. T_{XY} means that a wave is traveling in X and is transmitted at the interface into Y. X and Y stand for W-water, S-subbottom layer and H-half space.
In general there are always several possible ray paths, and the waves are arriving from above and from below. Therefore there will always be different superposition for the hydrophone and the seismometer.

Reflections of the thin subbottom layer are not visible as own onsets because the wave length of the P-wave $\lambda = 1280m$ is much larger than the thickness of the layer. But there is a waveform effect of this layer. There is a small wiggle visible at the end of PwP-phase, which is an effect of the thin layer. The thin layer disturbs the waveform of the PwP-phase.

3.2.5 Subbottom gradient layer

A gradient layer on top of the subbottom is another relevant model. The velocity and density of a top sediment layer increase with the depth because the sediment is compacted by its own mass. The Water-filled pore space is closed with increasing depth. Therefore the parameter at the sea floor are similar to the parameter of the water. With increasing depth the parameters converge to the parameters of the dry sediment and the water-sediment transition is diffuse.

The simulation in Fig. 3.9 shows that the energy is transferred from the multiple reflections in the water layer to the sediment reflections. Therefore the second reflection in the water layer is nearly vanished at 7 s, but the first sediment reflection has a relative large amplitude.

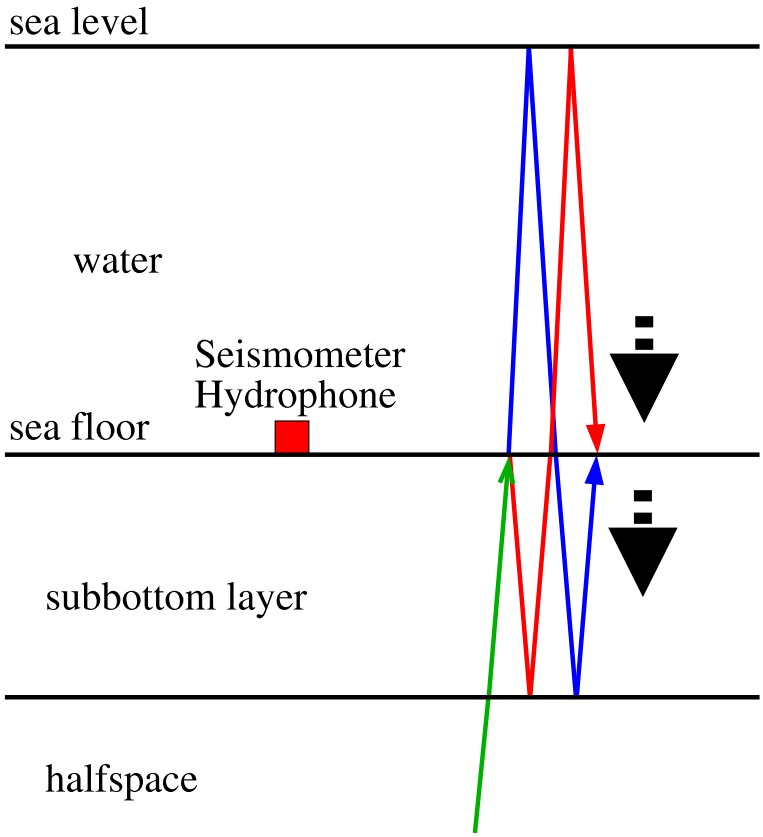

Figure 3.7: The ray paths for first reflection of subbottom layer after PwP. The green line indicates the P-wave, blue and red line the two possible ray paths. Both waves have the same direction of first motion. Therefore, they superpose constructively at the sea floor for the seismometer and destructively for the hydrophone.

Table 3.3: gradient layer model over half space.

	thickness	P-velocity	density
water layer	3.0 km	1.5 km/s	1.0 g/ccm
gradient layer	0.9 km	1.5-1.9 km/s	1.0-1.8 g/ccm
half space		4.4 km/s	2.5 g/ccm

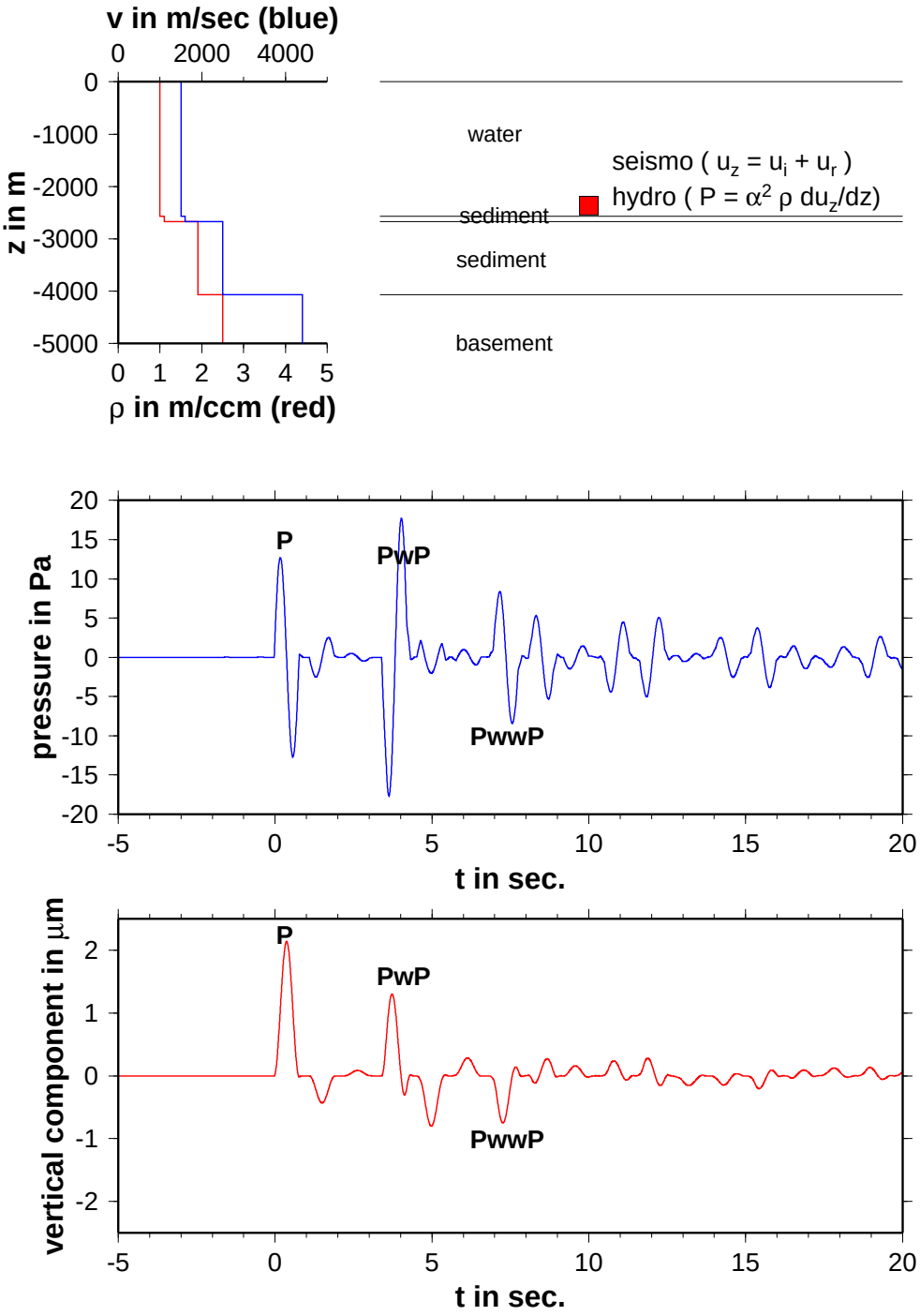

Figure 3.8: The three layer over half space model. **Top**: the model of the subsurface. Water depth corresponds to OBS OB10. **Middle**: the synthetic seismogram for pressure. **Bottom**: the synthetic seismogram for vertical ground motion.

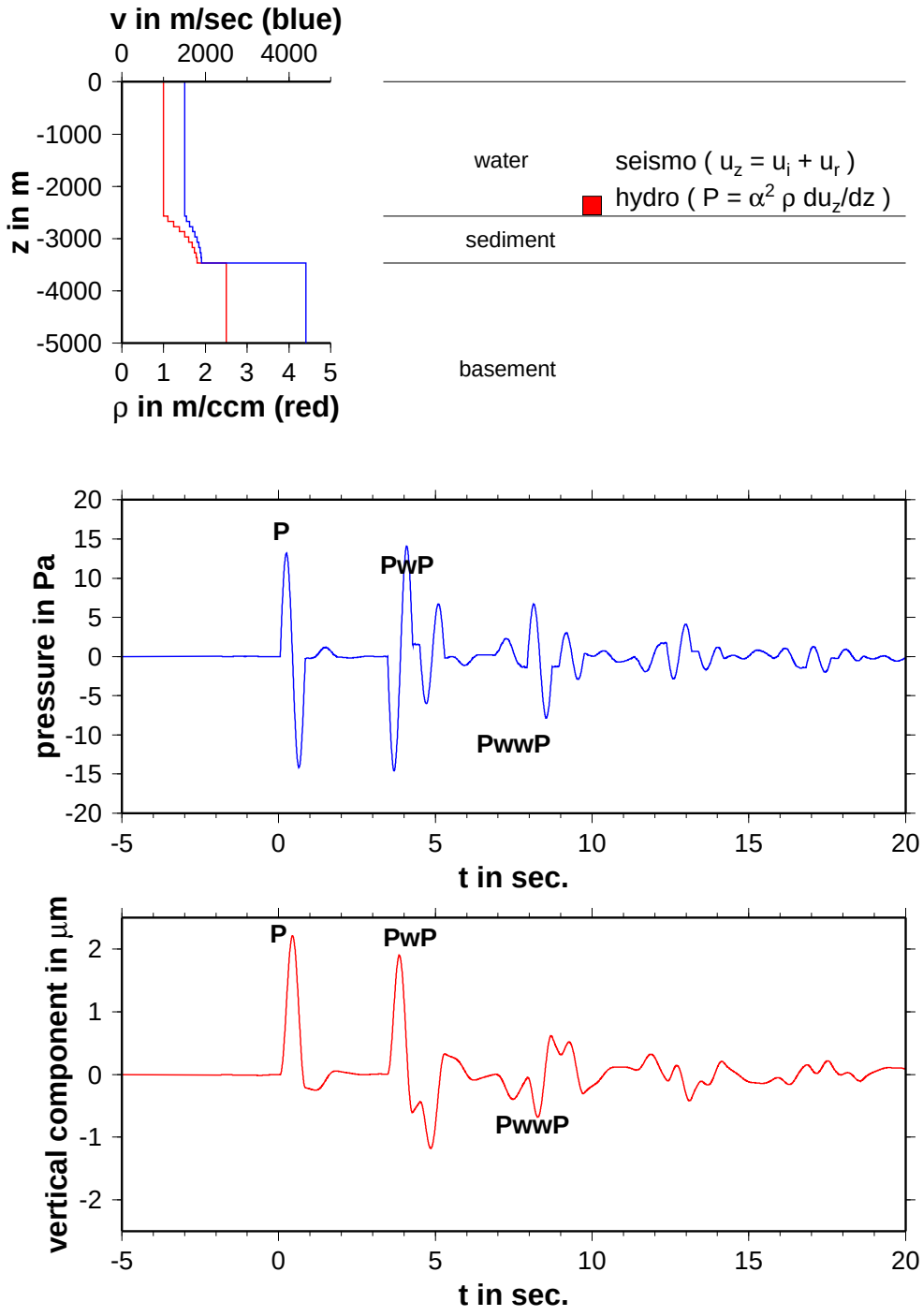

Figure 3.9: Gradient layer over half space model **Top**: model of the subsurface. Water depth corresponds to OBS OB10. **Middle**: synthetic seismogram for pressure. **Bottom**: synthetic seismogram for vertical ground motion.

3.3 Application to real data

The P-wave coda depends on the subbottom structure below the OBS-station as synthetic data have shown. Therefore, it is obvious to invert the subbottom structure from the coda-pattern which has been measured at the OBS. 13 deep earthquakes below 50 km occurred between Dec. 2000 and May 2001 in the Tyrrhenian Sea and are well localized in the region of the network. (see Tab. D.1). Each event was preprocessed by the following steps (see Fig. 3.10):

1. The restitution of the vertical seismometer component to ground motion and of the hydrophone component to pressure. A high pass filter with a corner of 0.5 Hz is applied to attenuate low frequencies produced by restitution.

2. The P-onset is picked and the P-waveform is cut out of the seismometer trace. The P-waveform is used as a time function of the incoming wave.

3. A bandpass filter (e.g. 1.7 - 5.0 Hz) is applied to the hydrophone, the seismometer and the P-waveform to improve the signal-to-noise ratio (SNR).

4. Traces with a clear P-waveform were chosen for the evaluation.

A three layered model over a half space is assumed. A grid search over the parameter of the second and third layer is done.

The first layer is a water layer. P-velocity is $\alpha_w = 1500\,\mathrm{m/s}$, density $\rho_w = 1000\,\mathrm{kg/m^3}$ and thickness d_w is taken from the bathymetry. The sensors (seismometer and hydrophone) are placed at the bottom of this layer.

The second layer is an unconsolidated top sediment layer as observed in active seismic surveys (Godin and Chapman (1999)). The porosity of the sediment is high at the top of the layer and the pores are filled with water. Lithostatic pressure increases with depth. The pores close and porosity decreases with depth.

A power law dependent on depth z is assumed for the velocity α: $\alpha(z) = 1500 + (\alpha_b - 1500) \cdot (z/d_1)^b$ (see also Laughton (1954)). The parameters which are determined in the grid search are the exponent b, the bottom velocity α_b and the thickness d_1. The average velocity α_1 is calculated from these parameters.

The third layer is a constant velocity sediment layer with the parameters velocity α_2 and thickness d_2.

A half space with a constant velocity of 5000 m/s is below the third layer. The density of each layer is determined by the Nafe-Drake curve (Fig. 3.11).

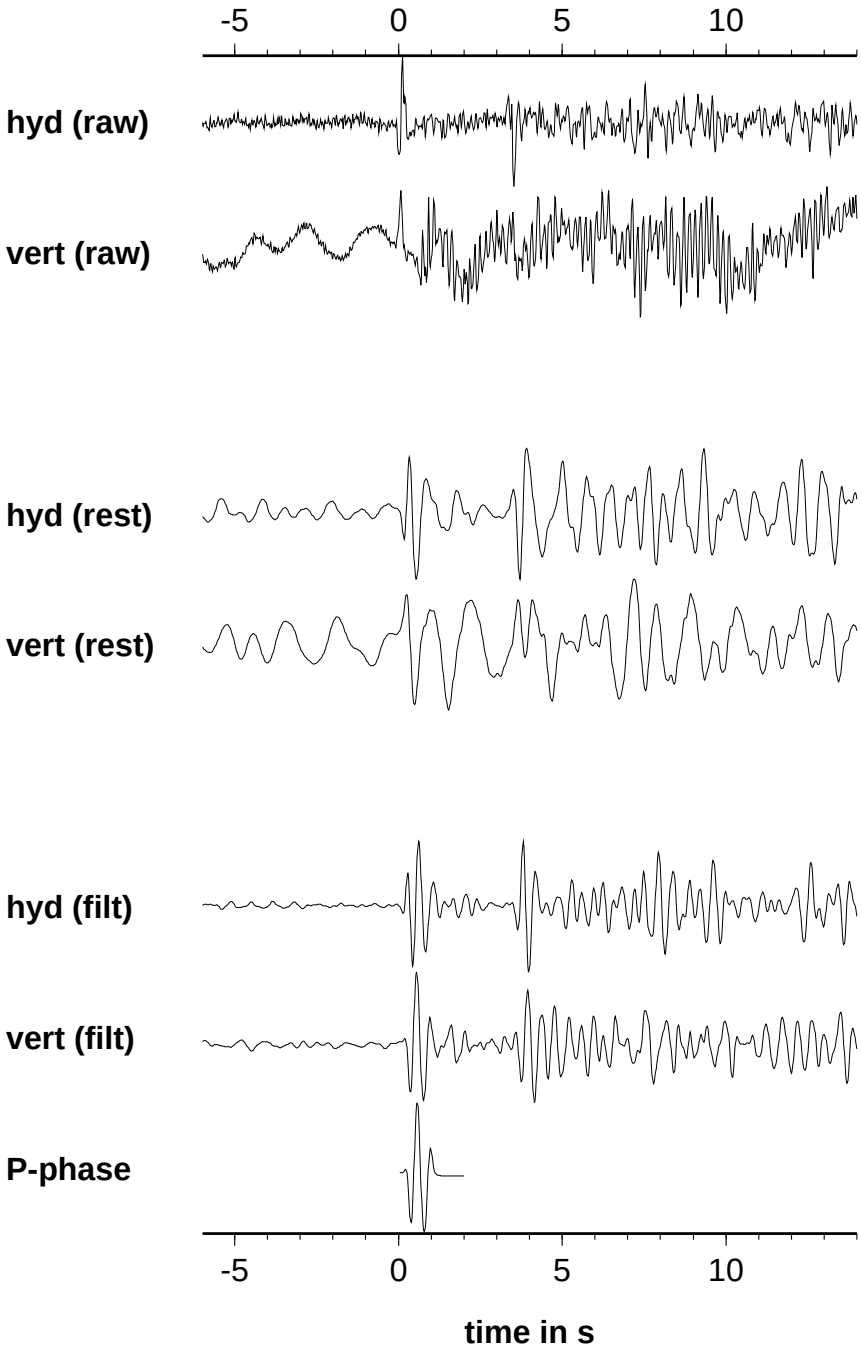

Figure 3.10: The processing steps are demonstrated by the event from 30.04.2001, 11:24:32.38. **Top**: the hydrophone and seismometer trace. **Middle**: the restituted hydrophone and seismometer trace. **Bottom**: the filtered hydrophone, the seismometer traces and the P-waveform.

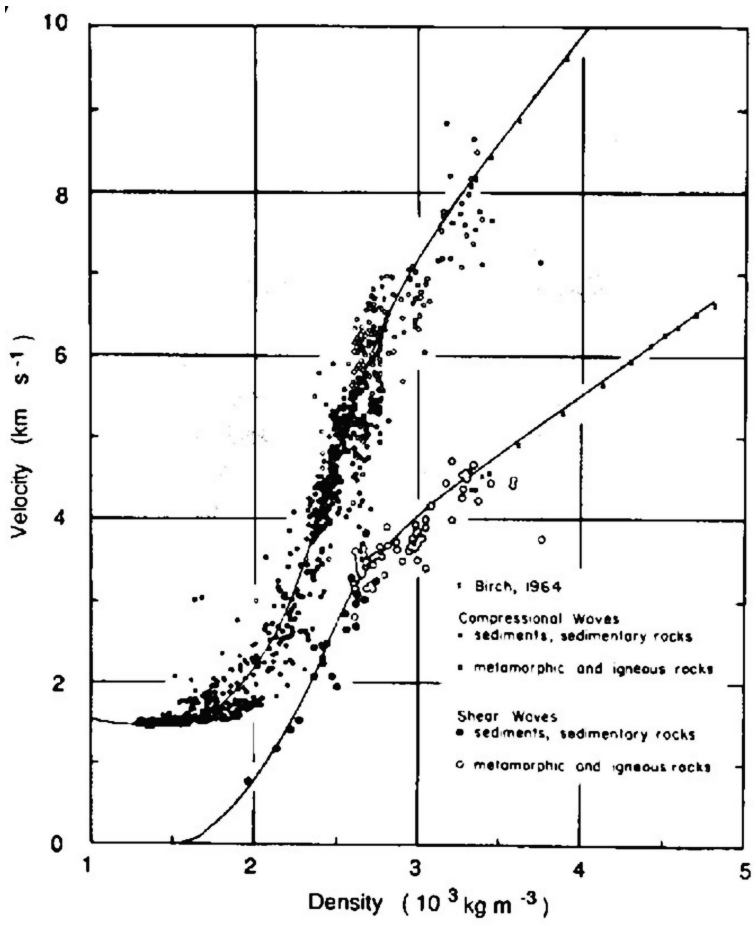

Figure 3.11: The Nafe-Drake-Curve. The P-velocity and density of marine sediments are measured and plotted against each other. (after Nafe and Drake (1963))

For each set of parameter the transfer function $\left(M_{11} + M_{12}\frac{M_{12}+M_{22}}{M_{11}+M_{21}}\right)$ of the underground is calculated (equation 3.22). The waveform of the P-wave is used as the waveform of the incoming wave $\int_{-\infty}^{\infty} A_n^+(\omega) exp\,[i\omega t]$. Convolving the P-waveform with the transfer function produces synthetic seismograms for each event.

In a first step of the inversion all parameters are varied to find a solution which fits best both the seismometer and hydrophone traces of several earthquakes. In a second step four of the five parameters are fixed to the best fitting model of the grid search and only one parameter is varied in order to sample the model space. Because data from several earthquakes are inverted simultaneously the approach is less sensitive to noise or the sources.

The parameter range for the grid search is listed in table 3.4. The misfit function is calculated for the first 6 s including the PwP-phase adding up the squared deviation and weighted by the energy of the trace:

$$misfit = \sum_{l=1}^{M} \frac{\sum_{i=1}^{n} ({}_l u_i - {}_l\hat{u}_i)^2}{\sum_{i=1}^{n} {}_l u_i^2} \tag{3.24}$$

M is the number of the seismometer and hydrophone traces, ${}_l u_i$ the observed data of the lth trace, ${}_l\hat{u}_i$ the synthetic seismogram and N the number of samples.

Table 3.4: Parameter for OB10 (top) and OB11(bottom)

layer	parameter	range	increment
2nd	thickness d_1	130 m - 400 m	30 m
	bottom velocity α_b	1600 m/s - 3000 m/s	200 m/s
	exponent b	0.4/0.6/0.8/1.0/1.25/1.66/2.2/2.4	
3rd	thickness d_2	1000 m - 2200 m	200 m
	velocity α_2	2000 m/s - 4400 m/s	400 m/s

layer	parameter	range	increment
2nd	thickness d_1	60 m - 240 m	30 m
	bottom velocity α_b	1600 m/s - 3000 m/s	200 m/s
	exponent b	1./1.2/1.4/1.7/2.0/2.5/3.0/4.0/6.0/8.0	
3rd	thickness d_2	800 m - 2000 m	200 m
	velocity α_2	2000 m/s - 4600 m/s	200 m/s

A bootstrap method is applied for the estimation of errors. A random selection is chosen from the traces with good SNR. Traces were allowed to occur more than once in the selection. Other traces are not selected. 25 selections are done. The minimum of the misfit function is estimated for each parameter separately and each selection. The

produced distribution represents the dependency of the result from the chosen traces and is a measure for the reliance of the estimated parameter value. The median and the 25%- and 75%-quartile are estimated for the distributions. The median is chosen instead of the mean value because the median is less sensitive to outliers.

3.3.1 Station OB10

Fig. 3.12, 3.13, 3.14 and 3.15 show the result of the simultaneous inversion of the waveform of 13 deep events at Station OB10. In Fig. 3.12 the model space of the grid search, the best model and the models in the ±25%-confidence interval are plotted. The models in the ±25%-confidence interval vary only little, especially for the top sediment layer. The best model has a thickness of 190 m and a average velocity of about 1630 m/s for the top sediment layer. The exponent has a value of 2.3 . The second subbottom layer is 2000 m thick and has a velocity of 3200 m/s.

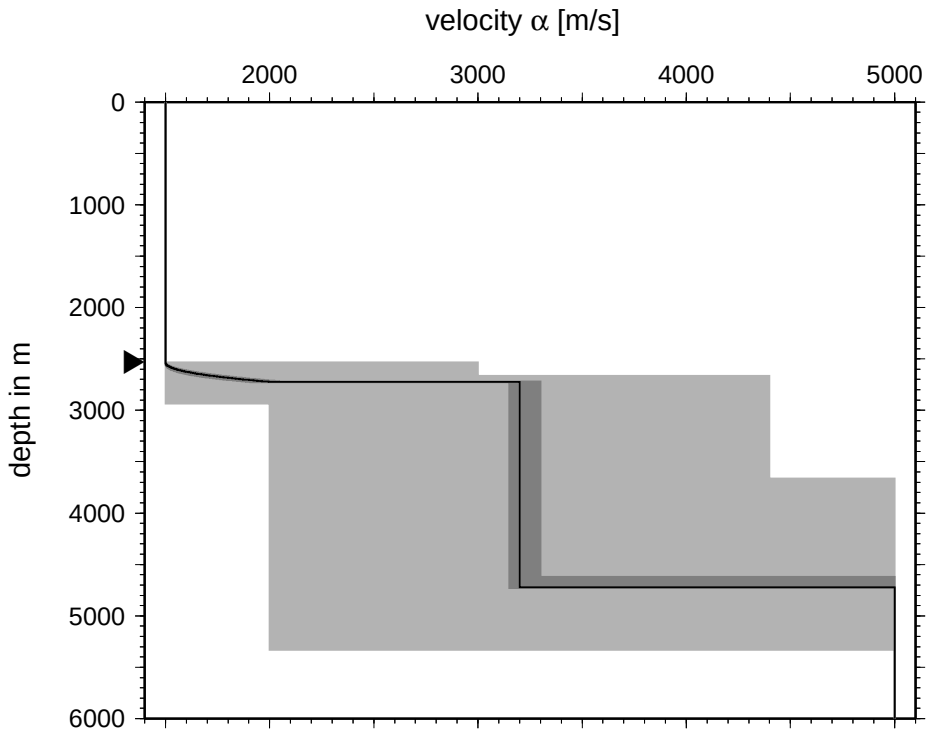

Figure 3.12: The model which fits best the data (black line) for OB10. The dark gray area corresponds to the error bars determined by the bootstrap method. The light trey area represents the model space of the grid search. The black triangle indicates the ocean bottom.

For a closer look to the parameter variation the misfit function is plotted against each parameter (Fig. 3.13). Errors for each parameter estimated by a bootstrap approach

are plotted as a box-and-whisker-symbol below the misfit functions. For each parameter the ±25%-confidence interval is narrow, symbolized by the box of the box-and-whisker-symbol. For the parameter of the top sediment layer even the minimum and the maximum of the bootstrap distribution are narrow. Especially the thickness of the top sediment layer is well constrained. The extrema of the bootstrap distribution for the second subbottom layer are far away from the median because in some cases of the bootstrap the best value of the parameter is found in the neighboring minima of the misfit function.

This is also shown in Fig. 3.14. The bootstrap distribution is plotted for each parameter. For the parameter of the top sediment layer the distribution is narrow and does not have any outliers, whereas the distribution for the parameter of the second subbottom layer have outliers. Especially the thickness seems to be nearly uniformly distributed between 3 values at 1300 m, 2000 m and 2700 m.

Fig. 3.15 compares recorded traces in black and simulated traces in red. The P-waveforms used are plotted in green. The simulated traces fit quite well the waveform of the PwP. This goes in hand with the well estimated parameter of the top sediment layer because the top layer is so thin that it is not recognized as an own onset but as a deformation of the waveform as demonstrated above. Especially the events on Julian day 342.2000 at 9:00 and on 120.2001 at 10:00 are well fitted.

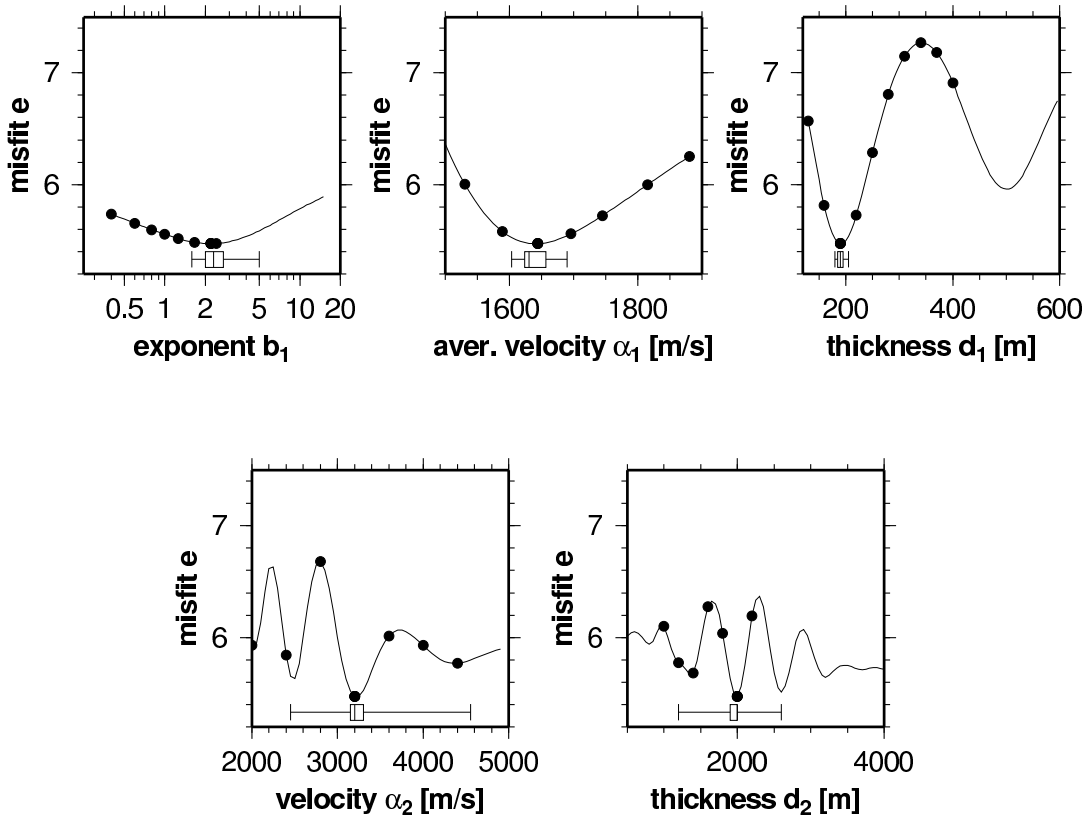

Figure 3.13: The parameters of the model for OB10. The first three plots show the parameters of the second gradient sediment layer: exponent b_1, average velocity α_1 and thickness d_1. The two lower plots show the parameters of the third layer: velocity α_2 and thickness d_2. Black dots show the nodes of the grid search. The solid line shows the course of the misfit relative to one parameter while the other parameters are fixed. The error bars are calculated with a bootstrap method. They are drawn as a box-and-whisker symbol below the curve. The symbol indicates the minimum, the 25%-quartile, the median, the 75%-quartile and the maximum of the distribution of the bootstrap error estimation for each parameter.

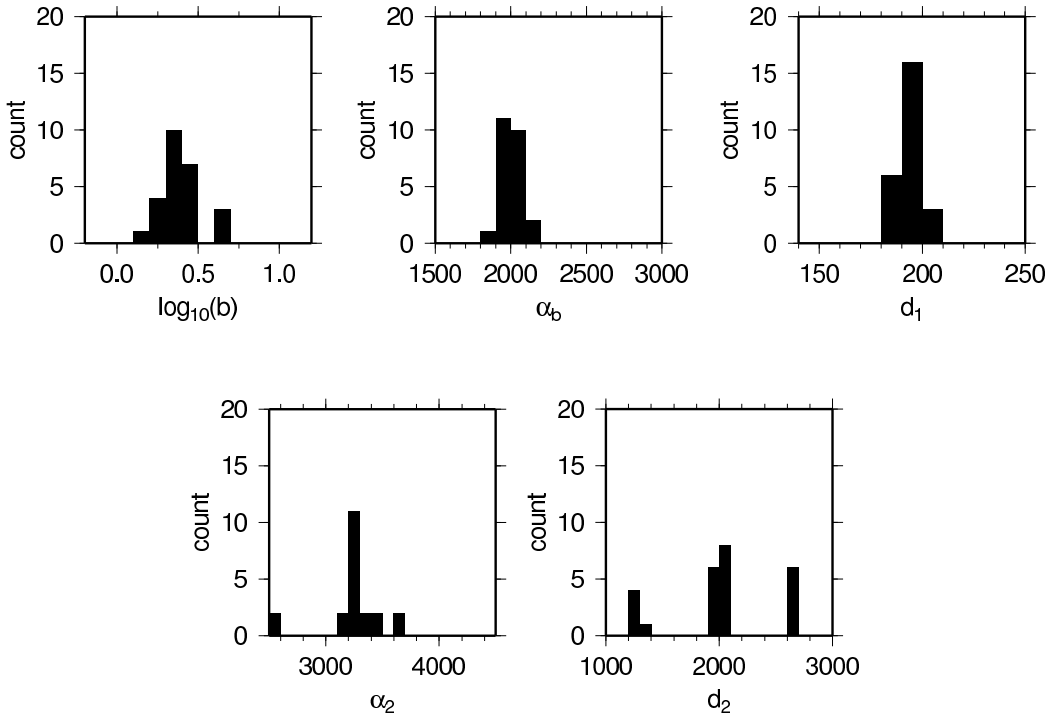

Figure 3.14: The distribution of the bootstrap error estimation for OB10. Velocities a_b and a_2 have the unit m/s, thickness d_1 and d_2 are in m and b is dimensionless.

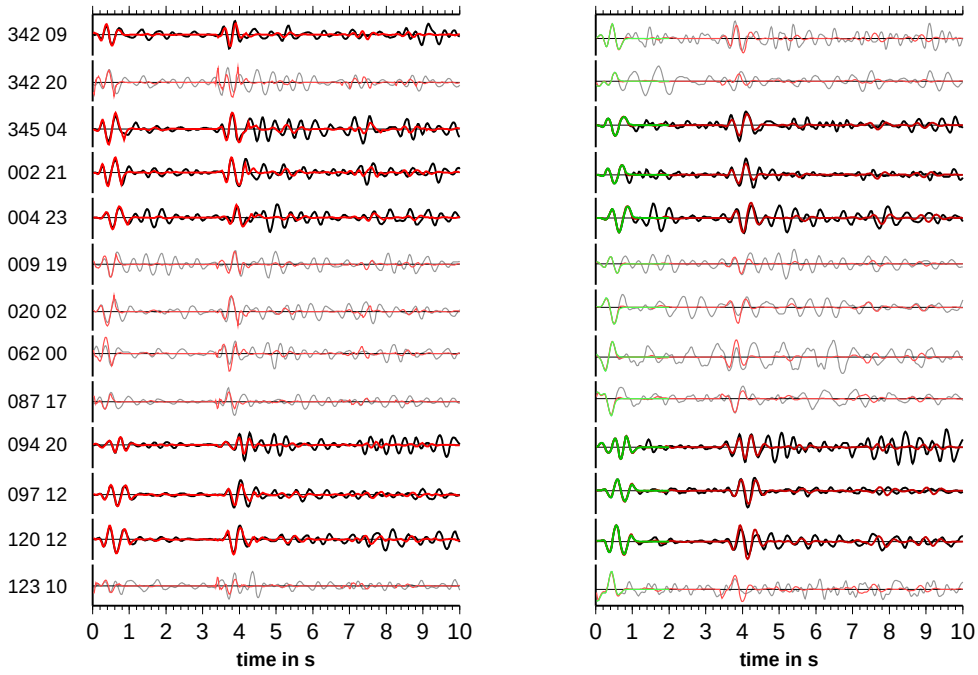

Figure 3.15: The traces of the deep earthquakes recorded by OB10 during the campaign (black/gray lines), the hydrophone traces on the left, the seismometer traces on the right. Julian day and hour of the events are plotted on the left margin. Green traces show the waveform of the P-onset used in the inversion. Only dark colored traces are used for the inversion. Red traces are synthetic seismograms of the best fitting model. All events are normalized to their maximum.

3.3.2 Station OB11

Fig. 3.16, 3.17, 3.18 and 3.19 show the result for OB11. Only 11 deep events could be used because no data was recorded on OB11 for the last 30 days. In Fig. 3.16 the model space for the grid search, the best model and the ±25% confidence interval for the model are plotted again. The top sediment layer is well defined. The thickness of the second subbottom layer is, however, poorly resolved. The top layer is about 95m thick and has an average velocity of about 1690m/s. The exponent of the velocity-depth-function is 3. The second layer has a velocity of 2400m/s and a thickness of 1400 m.

The misfit-function is plotted against each parameter in Fig. 3.17. As in Fig. 3.16 it is obvious that the top sediment layer is well and the second subbottom layer poorly estimated. The median of the bootstrap distribution for the thickness of the second layer is not near to the estimated thickness of 1400 m, but at 3100 m. This can also be deduced from Fig. 3.18. Here, the bootstrap distribution is plotted. In general, all distributions are broader as for station OB10. Even the distribution of the thickness of the top layer shows two outliers at 340 m resulting in a large maximum bar in Fig. 3.17 but a small ±25%-confidence interval. For the second subbottom layer the velocity has a narrow, but the thickness has a wide distribution. The high values of the thickness are not reliable, because the layer would have a TWT of around 2.5 s to 3.0 s. In this time window no subbottom reflection occurs, whereas the PwP-phase does at 2.7 s. Therefore these models try to fit the PwP-phase instead of a sediment reflection.

Fig. 3.19 shows the comparison between the recorded data and the simulated traces for the best model. There is a high noise level on the seismometer but a low noise level on the hydrophone traces. The synthetic traces fit the PwP-phase well but also the PwwP-phase at 5.4 s for some events (345.2000, 002.2001, 009.2001).

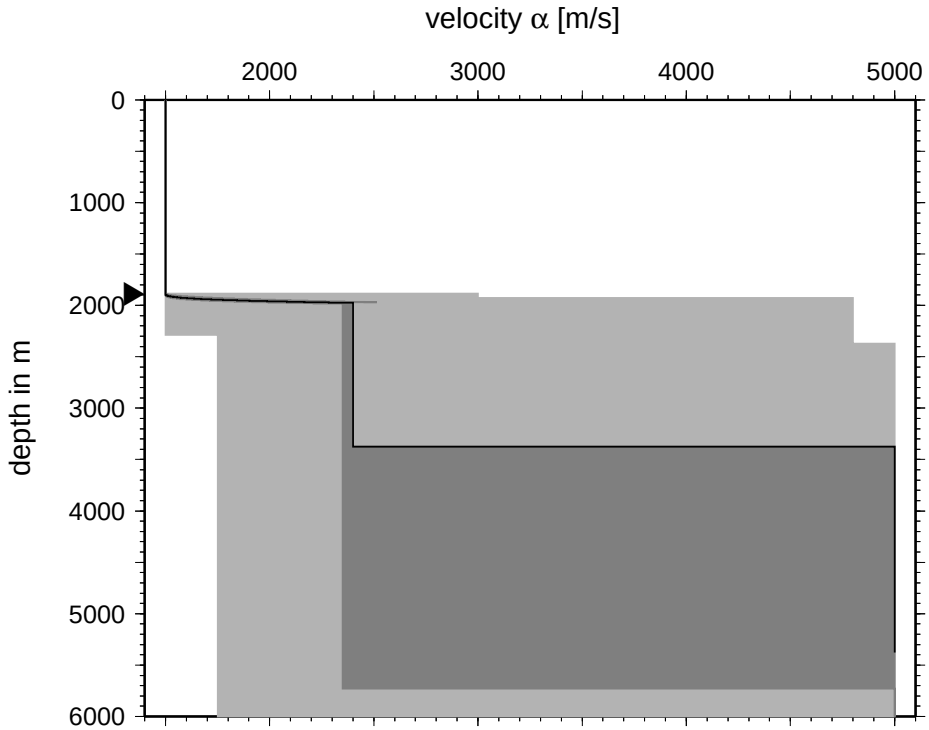

Figure 3.16: The model which fits best the data (black line) for OB11. The dark gray area corresponds to the 25% and 75% quartile determined by the bootstrap method. The light gray area represents the model space of the grid search. The black triangle indicates the ocean bottom.

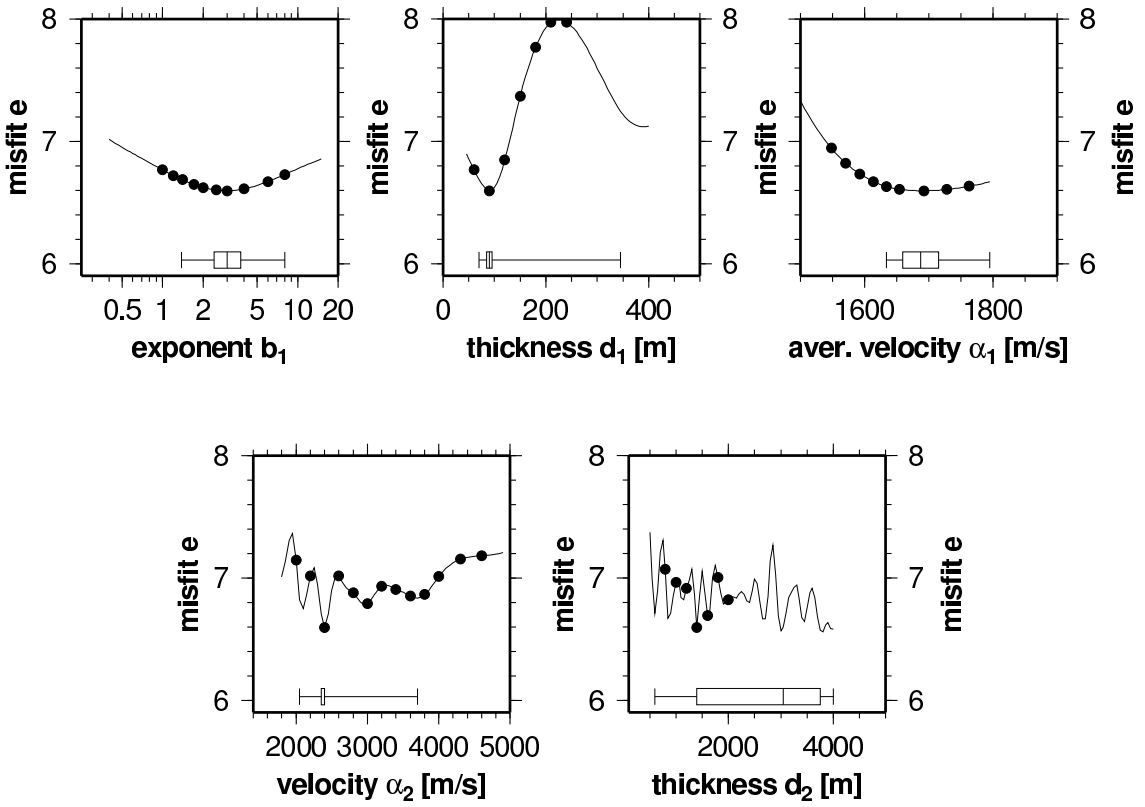

Figure 3.17: The parameters of the model for OB11. The first three plots show parameters of the second gradient sediment layer: exponent b_1, average velocity α_1 and thickness d_1. Two lower plots show parameters of the third layer: velocity α_2 and thickness d_2. The black dots show the nodes of the grid search. The solid line shows the course of the misfit function relative to one parameter while the other parameters are fixed. The error bars are calculated with a bootstrap method. They are drawn as a box-and-whisker symbol below the curve. The symbol indicates the minimum, the 25%-quartile, the median, the 75%-quartile and the maximum of the bootstrap distribution of each parameter.

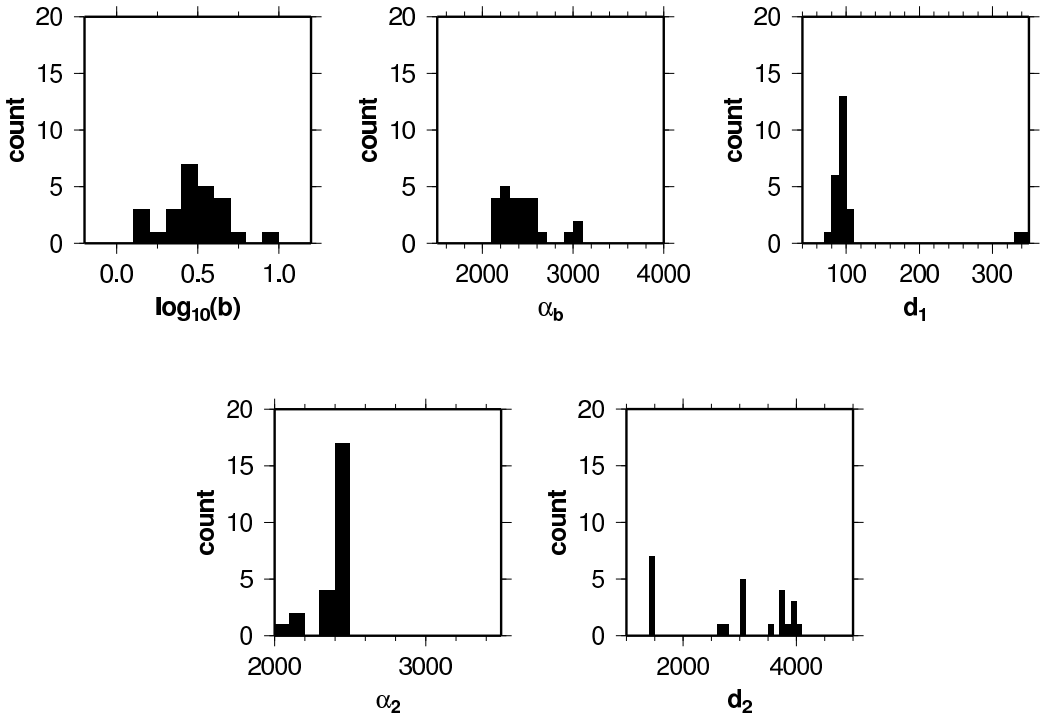

Figure 3.18: The distribution of the bootstrap error estimation for OB11. Velocities a_b and a_2 have the unit m/s, thickness d_1 and d_2 are in m and b is dimensionless

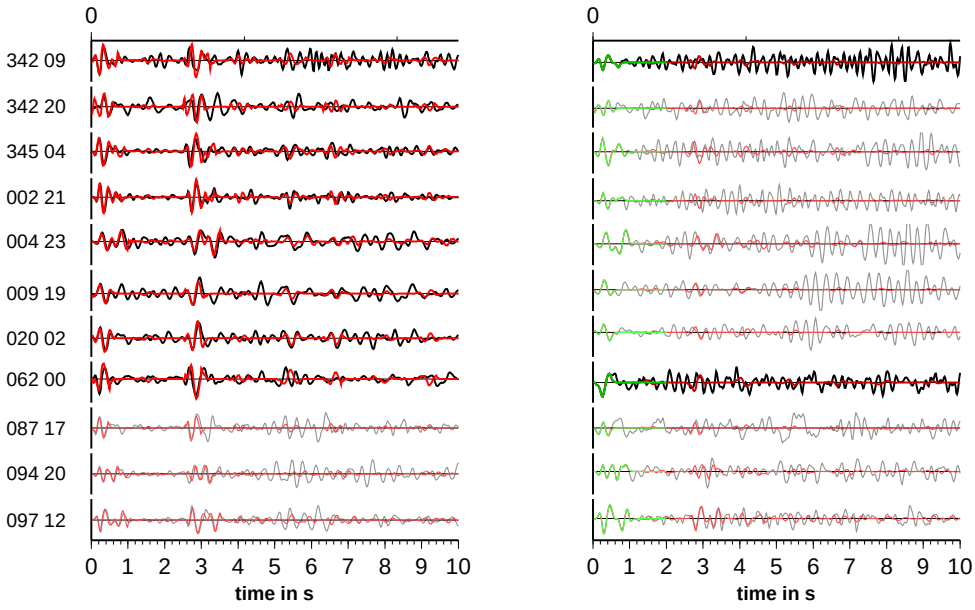

Figure 3.19: The traces of the deep earthquakes recorded by OB11 during the campaign (black/gray lines), the hydrophone traces on the left, the seismometer traces on the right. Julian day and hour of the events are plotted on the left margin. Green traces show the waveform of the P-onset used in the inversion. Only dark colored traces are used for the inversion. Red traces are synthetic seismograms of the best fitting model. All events are normalized to their maximum.

3.4 Discussion

It is important to know the structure under an ocean bottom station. Only with the knowledge of the subbottom underground is it possible to compare the data of the OBS with the data from station at land.

The subbottom structure and the water layer produce a side effect to the incoming wave, i.e. the incoming wave is convolved with the site effect:

$$P_{obs}(t) = S(t) * P_{incom}t \tag{3.25}$$

with $P_{OBS}(t)$ the waveform observed from the OBS, $P_{incom}(t)$ the waveform of the incoming wave and $S(t)$ the impulse response of the site.
Therefore it should be possible to deconvolve the site by applying an inverse filter and to transform the OBS-data into land station-like data. This can happen in the time-domain with an Wiener-optimum-filter or in the frequency domain by the division of the spectrum of the site response $\bar{S}(\omega)$.

The site effect consists of the multiple reflections PwP in the water layer and the subbottom structure. For deriving the subbottom structure the fact that the multiple reflections PwP show different pattern on seismometer and hydrophone is put to use. The amplitude of the multiple reflections depends on the impedance contrast at the ocean floor as I have shown in chapter 3.2.3. But not only the multiple reflections in the water layer but also the multiple reflections in the sediment show different patterns after the PwP-phase on both the hydrophone and the seismometer depending on impedance contrast between the layers in the subbottom (chapter 3.2.4 and chapter 3.2.5).

Using both the hydrophone and the seismometer traces is an advantage for deriving the subsurface structure as it constrains the subbottom structure more than inverting only one of each. 13 deep earthquakes with clear onsets occurred during the deployment in the Ionian slab below the OBS station network. Similar to Gurrola et al. (1995) hydrophone and seismometer traces of the deep earthquakes are used to invert simultaneously the subsurface structure. The simultaneous inversion has the advantage that the influence of noise to the inversion is reduced compared to a separate inversion of each event.

Because of the geometry between station and earthquakes a vertical incidence is assumed. Only the P-velocity and density of the layers can be resolved in this case, similarly to the inversion scheme for the reflectivity seismograms developed by Aki and Richards (1980) for recordings from exploration seismology. However, the time of the wave which arrives at the lowest interface is unknown in passive seismology. Therefore, a direct inversion of the traces is not possible like Aki and Richards (1980) suggest. The waveform also depends non-linearly on the subbottom structure. Hence, the solution for the inverse

problem can be found by a step-wise approximation of the solution using a linearized version of the inversion problem or by a systematic grid search.

Using a systematic grid search the number of layers are limited because the parameter space increases rapidly by the number of layer. A linearized approach to the inversion problem would allow the use of more layers. But it is uncertain whether the inversion is stable and converge and whether the right solution is found. This are common problems of non-linear inversions.

For this reason, we applied a systematic grid search to solve the inversion problem. The systematic grid search is done over the parameter space of a 3 layer over half space model. The three layers stand for one ocean layer and two subbottom layer. Less than two subbottom layer do not explain all features of the traces.

First all parameters are varied on a coarse grid to make the grid search efficient. For each parameter set synthetic seismograms are calculated and compared with the observed data. A misfit function is computed and a minimum of the misfit function is found on the coarse grid. In a second step only one parameter is varied and the others are fixed to sample the model space around the minimum. A bootstrap method is applied for the estimation of errors.

The result shows that at both stations the top sediment layer is well but the second only poorly constrained. The average velocity of the top layer is 1.630 km/s and 1.69 km/s. Thickness is 95 m and 190 m. We retrieve an exponent of the power law of the P-velocity larger than 1. Normally top sediment layers are assumed to be unsolidified and have their P-velocities only little higher than water due to the fact that these sediments are water-saturated. The P-velocity follows a power law depending on depth with an exponent smaller than 1 as derived theoretically as well as from observations (e.g. Laughton, 1954; Godin and Chapman, 1999).

The station OB10 and OB11 are situated to north of the Aeolian islands at the continental slope in the margin of the Tyrrhenian basin. Both station are located at the lower continental slope (Fig. 1.5). Most of the sediment is deposited in the peri-Tyrrhenian basins like the Celafù and the Giola Basin. The Aeolian islands behave as a barrier to the sediment transport. Therefore, only a thin sediment layer exists on the lower slope (Gennesseaux et al., 1998). The top layer can therefore be interpreted as the top sediment layer.
A question is why the exponent of the power law is larger than 1. A possible answer could be that this layer does not only consist of one but two thin layers and that the lower one has a larger velocity. If both layers are seen as one the velocity is assumed to have a power law with an exponent larger than 1 (Fig 3.20). Another possible answer is that there is no sharp interface between the top and the second subbottom layer and

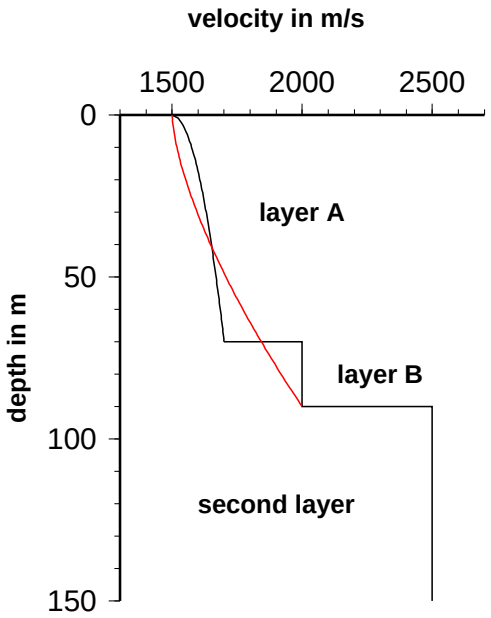

Figure 3.20: Two layers as seen as one layer. black: real velocity. red: apparent velocity.

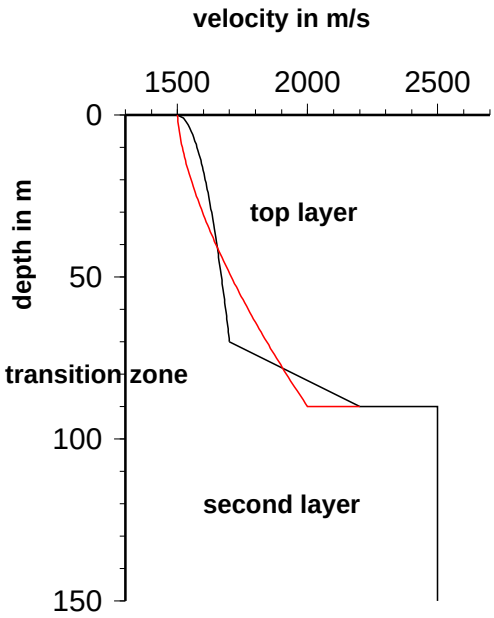

Figure 3.21: Transition-zone-model. black: real velocity. red: apparent velocity.

the velocity increases steadily to the second layer (Fig 3.21).

It is hard to say what exactly the second subbottom layer is because it is poorly constrained. It could be related to a volcanic complex of the Aeolian islands.

The inversion is done with recorded data from deep earthquake which has occurred in the subduction zone. Therefore, it was justified to assume vertical incidence. In this case it is not possible to invert the data for S-velocities.

the question whether it is possible to use shallow earthquakes in the inversion, too, remains unanswered. It is likely, however, that in this case it is not possible to assume a vertical incidence. Though the wave propagation is steepen in the upper most layer the time difference between P and PwP should be similar to the case of a vertical incidence, but there should be a significant deviation in the underground. Then S-waves are converted from P-waves and occur in the data. For a non-vertical incidence it would also be possible to retrieve S-velocities.

In general the statement can be made that it is possible to invert a subsurface model from a single station recording. The simultaneous inversion is important to minimize the influence of noise and to derive a more reliable model. There is more potential in the inversion method since only a simple model is derived and indications for a more complex model exist. A higher sampling rate is needed to evaluate the ray parameter

from the time difference between PwP and P.

Chapter 4

Wavefield decomposition

In chapter 3 the subsurface structure is derived to obtain the possibility of removing the water layer multiples. Schneider and Backus (1964) were among the first who recognized that simultaneous measurements of ground velocity and pressure on the ocean-bottom opens the possibility to attenuate water layer multiples (see also Yan (2002)). This approach takes advantage of the fact that hydrophones and vertical geophones generate signals of the same polarity for upgoing waves, but of opposite polarity for downgoing waves. To be more specific, the observed wavefield can be decomposed into up- and downgoing contributions, either by acoustic decompositions as in the very first approaches (dual sensor method, e.g. Barr and Sanders, 1989) or by full elastic decomposition as introduced in recent years (e.g. Amundsen and Reitan, 1995).

While the wavefield in the ocean layer is dominated by water layer multiples, the upgoing wavefield in the subbottom is not and is thus better suited for structural analysis and interpretation.

A necessary prerequisite for the wavefield decomposition is the knowledge of the sensor transfer functions, the seafloor impedance contrast and the ray parameter of the body-wave under study. When the characteristic features of the expected decomposed wavefields are known, techniques can be developed to resolve one or all of the interdependent parameters. Thus, the wavefield decomposition has the potential to estimate the coupling of sensors, the impedance of the uppermost layers of the seafloor and the ray-parameter of the incoming phases.

In active seismic experiments plane wave decompositions have to be introduced (e.g. in τ-p or ω-k domain Greenhalgh et al., 1990; Wapenaar et al., 1990; Amundsen and Reitan, 1995; Osen et al., 1999), which need to have of having dense and regular sensor-spacing along one or several parallel profiles. The off-shore petroleum industry has continuously developed multicomponent seafloor recording techniques (for instance ocean bottom ca-

bles, see e.g. Caldwell, 1999), aiming mainly at improving the structural imaging in sedimentary basins and the studying of shear properties of the sea-bed. The wavefield decomposition can be applied to these data and has the potential for improving the images.

In passive seismology decomposition can be applied to single station data since the plane wave assumption is fulfilled when sources are far away from the receivers. While body-waves of intermediate deep and moderately strong earthquakes recorded at local stations contain signals at frequencies above 1 Hz teleseismic body-waves are often analyzed below 0.25 Hz. Water layer multiples (see also chapter 3) in a 3000 m deep ocean have a characteristic two-way travel time of about 4 s. Thus, local deep earthquakes may generate water layer multiples clearly separated from the incoming wave, while reverberations in teleseismic signals introduce a smooth wavefield distortion which is hard to identify.

In this chapter the effect of water multiple reflection is demonstrated at deep local earthquakes and by means of teleseismic applications. Wavefield decomposition is applied to study data from local deep earthquakes and to investigate its potential with regards to the improvement of travel time residuals and receiver functions from teleseismic events.

4.1 Theory

It is assumed that an upgoing, plane P-wave arrives at the ocean floor at time t_0 with an incidence angle φ_2 and a horizontal slowness $p = \sin\varphi_2/\alpha_2$. α_2 is the P-wave velocity in the ocean bottom layer. A subscript 1 or 2 indicates whether the parameter or variable is attributed to layer 1 just above and layer 2 just below the interface, respectively.

The wave energy will partition at the interface due to reflections and transmissions. Vertical tractions T_{zz} and the vertical velocity v_z are assumed to be continuous across the ocean bottom interface whereas shear traction is assumed to be zero.

The wave generates the ground particle velocity $\vec{v}$ which is measured with a three-component ocean bottom seismometer and pressure P is measured with a hydrophone in the water at the ocean-bottom. The vector $\vec{v}$ is displayed in a coordinate system containing a vertical (v_z), a radial (v_r) and a transversal component (v_t).

Because of the different type of sensor (directional and isotropic sensor) the recorded wavefield at time $t > t_0$ can be decomposed into up- (U) and downgoing plane waves (D) which have all the same slowness p (Fig. 4.1).

Typically, eight wavefield components are considered (e.g. Amundsen and Reitan, 1995), namely U_1^P, D_1^P, U_2^P, D_2^P, $U_2^{v_z}$, $D_2^{v_z}$, $U_2^{v_r}$ and $D_2^{v_r}$. Here and in the following, a superscript

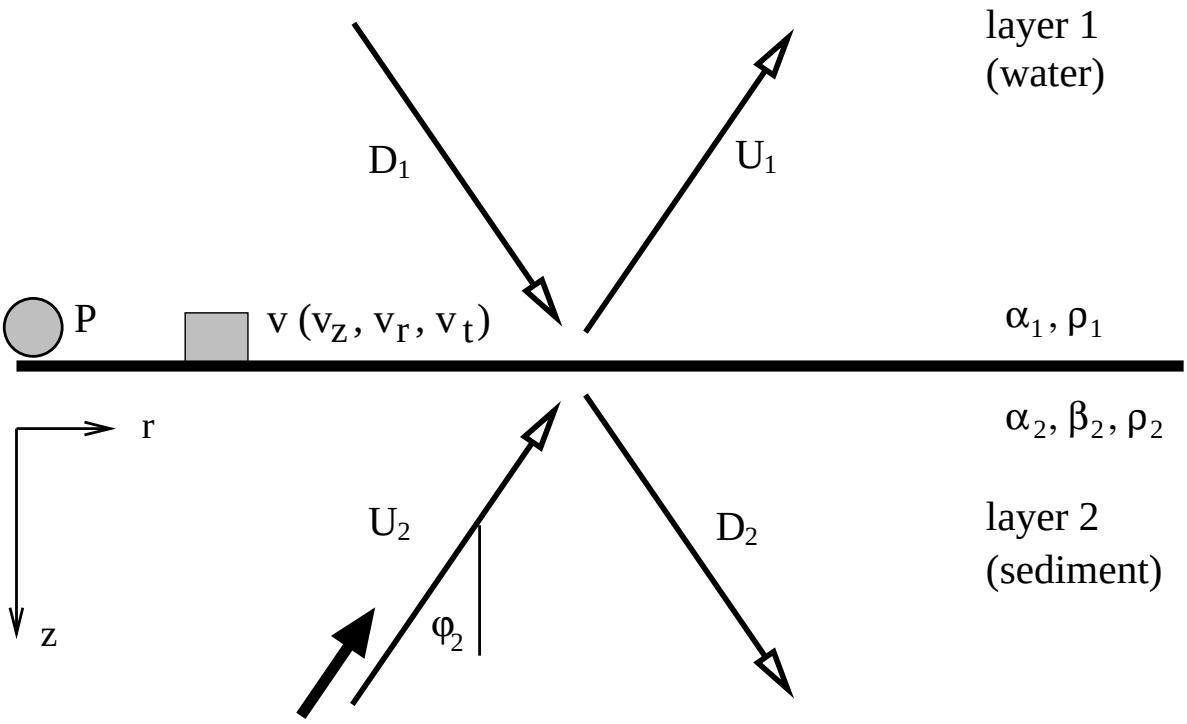

Figure 4.1: Plane waves, which hit the ocean floor, can be decomposed into up- and downgoing plane waves just above (U_1, D_1) and below (U_2, D_2) the seafloor. The ocean layer is characterized by a P-wave velocity $\alpha_1 = 1500$ m/s and a density of $\rho_1 = 1000$ kg/m^3. The shear-wave velocity β_1 is zero. α_2, β_2 and ρ_2 of the ocean floor sediments may vary significantly from site to site and have to be estimated for each station. The thick arrow indicates the incoming P-wave, the gray circle the hydrophone which measures the pressure P and the square the seismometer which measures ground velocity $\vec{v} = (v_z, v_r, v_t)$.

(P, v_z, or v_r) indicates that the wavefield is scaled to have dimensions of pressure or particle velocity, respectively.

The relation between pressure and particle velocity $\vec{v}$ of a P-wave is deduced in chapter 3.2.1. The scaling is defined by the impedance $I_i = \rho_i \alpha_i$ of the medium of layer i (see equation 3.13). It is obvious that S-waves do not produce a pressure variation because of the transversal polarization of the S-wave.
Because of the longitudinal polarization of P-waves the ground velocity $\vec{v}$ is parallel or antiparallel to the wave number vector $\vec{k}$, i.e. $\vec{v}$ can be written as:

$$\vec{v} = \pm |\vec{v}| \frac{\vec{k}}{|\vec{k}|} \tag{4.1}$$

.

The seafloor is a boundary between a solid and a fluid medium. The boundary conditions are a continuous vertical displacement $\vec{v_z}$ and a normal traction T_{zz} and a vanishing shear tractions $T_{xz} = T_{yz} = 0$. Therefore, the elastic pressure produced by a P-wave can be related to the vertical ground velocity (see Fig. 4.2):

$$P(z,t) = \rho\alpha\frac{\vec{k}}{k}\vec{v}(\vec{x},t) = \tag{4.2}$$

$$= \begin{cases} \rho\alpha\ |\vec{v}(\vec{x},t)| & \vec{v} \text{ parallel to } \vec{k} \\ -\rho\alpha\ |\vec{v}(\vec{x},t)| & \vec{v} \text{ anti-parallel to } \vec{k} \end{cases}$$

$$= \begin{cases} \rho\frac{\alpha}{\cos\varphi}\ v_z(\vec{x},t) & k_z > 0 \text{ (Upgoing)} \\ -\rho\frac{\alpha}{\cos\varphi}\ v_z(\vec{x},t) & k_z < 0 \text{ (Downgoing)} \end{cases} \tag{4.3}$$

The fraction $\cos\varphi_i/\alpha_i = \sqrt{1/\alpha_i^2 - p^2} = q_{\alpha_i}$ is the vertical slowness q_{α_i} of the wave in layer i.

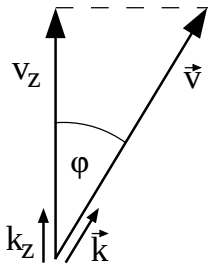

Figure 4.2: The ground velocity vector $\vec{v}$ stands for a P-wave parallel (as shown) or anti-parallel to the wave number vector $\vec{k}$. The relation between the value of $\vec{v}$ and the vertical ground velocity v_z is :

$$|\vec{z}| \cdot \cos\varphi = v_z$$

φ is the incidence angle.

Acoustic decomposition or dual sensor method

In an acoustic media like water the S-waves vanish and, thus, only P-waves are present. Like the reflectivity method up- and downgoing wavefields are both measured by the seismometer and the hydrophone. Therefore, the pressure and vertical particle velocity are a superposition of the up- and downgoing wavefield. Using equation 4.3 leads to the following equation:

$$\begin{pmatrix} P \\ v_z \end{pmatrix} = \begin{pmatrix} 1 & 1 \\ \frac{q_{\alpha_1}}{\rho_1} & -\frac{q_{\alpha_1}}{\rho_1} \end{pmatrix} \begin{pmatrix} U_1^P \\ D_1^P \end{pmatrix} \quad . \tag{4.4}$$

v_z is measured on or just below the ocean floor. It can be used in equation 4.4 to describe wavefields in layer 1 (water layer) due to the continuity of v_z across the interface. Since both sensors, the seismometer and the hydrophone, measure the up- and downgoing wavefields with different a polarity, the matrix in equation 4.4 can be inverted (see also

Schneider and Backus, 1964)

$$\begin{pmatrix} U_1^P \\ D_1^P \end{pmatrix} = \frac{1}{2}\begin{pmatrix} 1 & \frac{\rho_1}{q_{\alpha_1}} \\ 1 & -\frac{\rho_1}{q_{\alpha_1}} \end{pmatrix}\begin{pmatrix} P \\ v_z \end{pmatrix} \tag{4.5}$$

A general prerequisite for a decomposition into up- and downgoing waves is that the sensors involved measure the two wavefields with an alternating polarity so that the inverse matrix in equation 4.5 exists.

Elastic decomposition

In layer 2 (sub bottom layer) S-waves do not vanish and thus a full elastic decomposition has to be applied to separate up- and downgoing wavefields. This procedure was introduced by Amundsen and Reitan (1995); Osen et al. (1999):

$$\begin{pmatrix} U_2^k \\ D_2^k \end{pmatrix} = \frac{1}{2}\begin{pmatrix} F_p^k & +F_z^k & F_r^k \\ F_p^k & -F_z^k & F_r^k \end{pmatrix}\begin{pmatrix} P \\ v_z \\ v_r \end{pmatrix} \tag{4.6}$$

Index k defines the scaling unit and is either P, v_z or v_r.

The coefficients are:

$$\begin{aligned}
F_p^P &= 1 \\
F_z^P &= \frac{\rho_2}{q_{\alpha_2}}\left[(1-2p^2\beta_2^2)^2 + 4p^2\beta_2^2 q_{\alpha_2} q_{\beta_2}\right] = \frac{\rho_1}{q_{\alpha_1}}\frac{1+r}{1-r} \\
&\quad \text{with} \quad r = \frac{(1-2p^2\beta_2^2)^2\rho_2 q_{\alpha_1} + 4p^2\beta_2^4 q_{\beta_2} q_{\alpha_1} q_{\alpha_2} - \rho_1 q_{\alpha_2}}{(1-2p^2\beta_2^2)^2\rho_2 q_{\alpha_1} + 4p^2\beta_2^4 q_{\beta_2} q_{\alpha_1} q_{\alpha_2} + \rho_1 q_{\alpha_2}} \\
F_r^P &= 0 \\
F_p^{v_z} &= \frac{-1}{\rho_2 q_{\beta_2}}(p^2 + q_{\alpha_2} q_{\beta_2}) \\
F_z^{v_z} &= 1 \\
F_r^{v_z} &= \frac{p}{q_{\beta_2}}\left[1 - 2\beta_2^2(p^2 + q_{\alpha_2} q_{\beta_2})\right] \\
F_p^{v_r} &= 0 \\
F_z^{v_r} &= \frac{-q_{\beta_2}}{q_{\alpha_2}} F_r^{v_z} \\
F_r^{v_r} &= 1\,,
\end{aligned}$$

where r is the reflection coefficient for the water-solid interface for a downward traveling wave (see e.g. Barr and Sanders, 1989). For a vertical incidence F_z^P is reduced to a similar form as in equation 4.5, and v_r is zero. The upgoing wavefield in the sediment would resemble the pressure wave in the water for the extreme case of a vanishing impedance

in the sediments only. It is interesting that up- and downgoing waves on the radial component can be retrieved from v_z and v_r. The reason for this is that both components show the polarity reversal when the different wavefield components are measured.

The coefficients $F_{(P,z,r)}^{(P,v_z,v_r)}$ depend only little on the angle of incidence below 30 degrees (Fig. 4.3). Similar to the discussion of the incidence angle of the PwP-wave in the water layer (chapter 3.1) only a small angle of incidence is excepted in the top sediment layer. The uppermost marine sediment layer has a P-velocity close to the P-velocity of water because the sediment is unsolidified and has a large porosity. Thus, the critical angle for a sediment layer with a P-velocity of 1700 m/s is about 17 degrees. This applies to rays traveling through the upper crust with a P-velocity of 5800 m/s. For rays traveling through deeper parts of the earth the critical angle of incidence is even smaller. Therefore the angle of incidence is an uncritical variable for seismological applications.

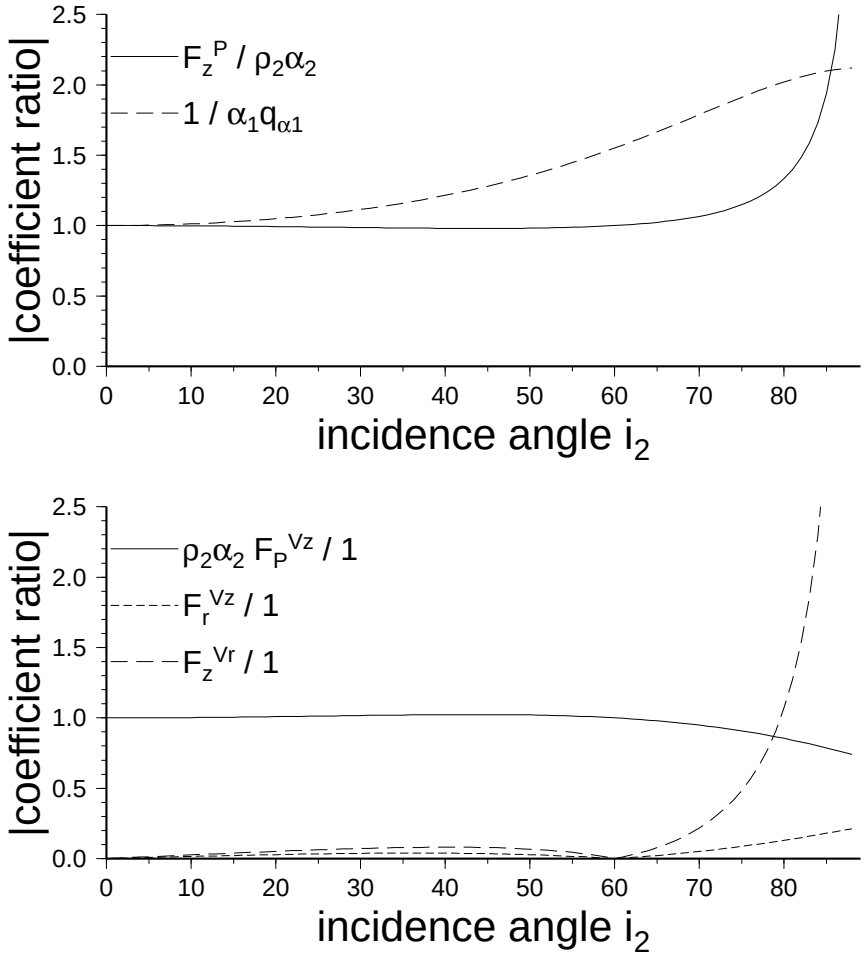

Figure 4.3: Coefficients $F_{P,z,r}^{P,v_z,v_r}$ of the wavefield decomposition are plotted against the angle of incidence.

Fig. 4.4 shows synthetic waveforms for a P-wave arriving at an ocean bottom station

located at the interface between an elastic half-space and a three kilometer thick oceanic layer. The source (explosion type) was fixed at 350 km depth below sea level, and the station was in the epicenter ($i_2 = 0°$). Full seismograms and spherical waves from point sources were simulated (program qs2.f77 from Wang, 1999). The wavefronts are, however, nearly planar when arriving at the station. In the following, the decomposition will be applied to earthquake data with a similar source-station geometry.

Both, P and v_z in Fig. 4.4 show large-amplitude water layer multiples after the first arrival in 4 s intervals. On the hydrophone the first multiple has even larger amplitudes than the first arrival. Multiples on the hydrophone and seismometer channel have opposite polarities, while the first arrival has a positive polarity on both traces (see chapter 3.2.3). The decomposed waves U_1^P, U_2^P, D_1^P and D_2^P in Fig. 4.4 show a simpler pattern. The upgoing wave in layer 2 (U_2^P) has no signal from multiples and only the incoming wave can be seen. This is expected since no energy is reflected back from the underlying half-space. The downgoing wave in layer 1 (D_1^P) has no direct wave but only multiples which travel downward after a reflection at the sea surface. The up- and downgoing waves in the ocean have the same amplitude and polarity pattern of phases, although they are delayed by the two-way travel time of the acoustic waves in the ocean layer. This strict relation between both wavefields will also be conserved if the incoming wavefield is more complex or when the waves will be back-scattered from the crust.

The advantages of the wavefield decomposition are obvious and will be discussed further at a later points.

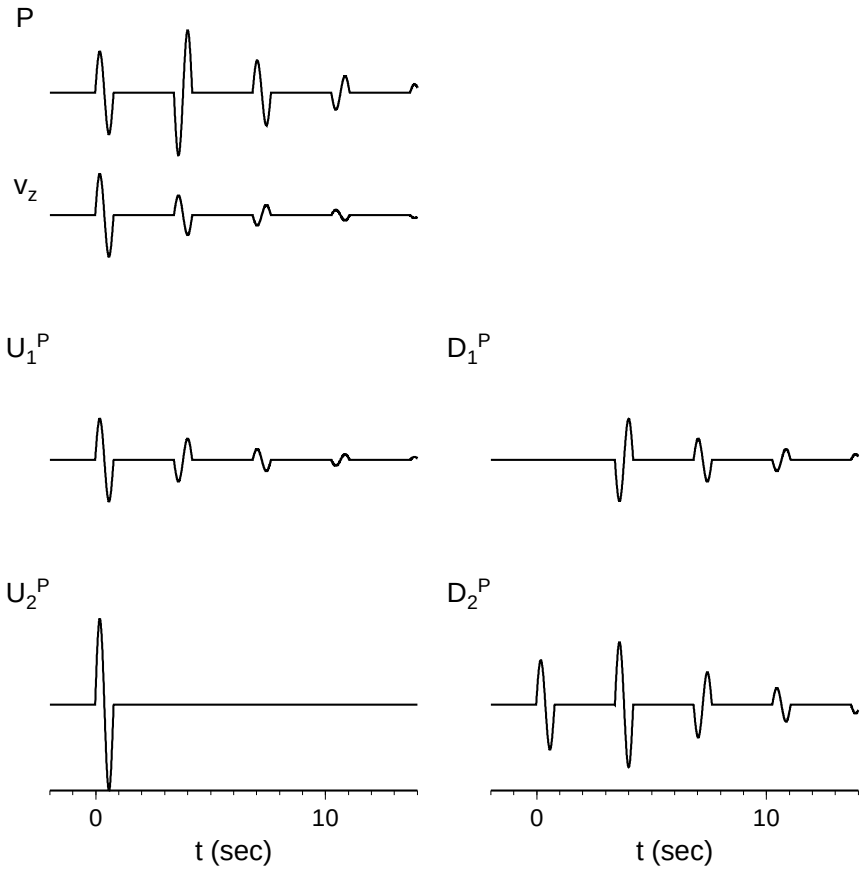

Figure 4.4: The simulated pressure (P) and the vertical particle velocity (v_z) for the simple model of an ocean layer over a half-space (α_1 = 1500 m/s, ρ_1 = 1000 m/s, α_2 = 1900 m/s, β_2 = 1440 m/s, ρ_2 = 1900 kg/m^3). The ocean layer has a thickness of 3 km. A volumetric point source (explosion) has been fixed at 350 km depth below sea level. The source time function is a 0.8 s long Brüstle-Müller-wavelet (Brüstle, 1985). The station is located above the source ($i_2 = 0°$). The vertical particle velocity is normalized with the impedance of water $\rho_1\alpha_1 = 1.5{\cdot}10^6$ kg/(m^{2}s).

4.2 Sensor sensitivity and seafloor properties

A question is, however, whether the decomposition can be applied to real earthquake data and ocean bottom recordings since accurately calibrated recordings are necessary as well as estimates of elastic parameters of the ocean floor. This section gives proposals on how to overcome these difficulties and how to use the decomposition to estimate the relative sensor sensitivity and seafloor properties from single station recordings. First, the estimation of the relative sensor sensitivity and, secondly, different approaches for the estimation of the seafloor properties will be indicated. This has been introduced as two- or three-step decomposition (see e.g. Schalkwijk et al., 1998).

4.2.1 Hydrophone calibration factor

The acoustic decomposition in equation 4.5 depends on the incidence angle of the ray and the P-wave velocity in the water, both are well known. To estimate an unknown sensitivity of the pressure sensor (or seismometer channel) equation 4.5 is applied and the trace energy of the downgoing pressure wave D_1^P in the water is minimized before the first water-layer multiple, i.e.

$$F_1 \quad = \quad \frac{1}{N}\sum_{i=1}^{N}(D_{1i}^P)^2 \quad \text{is minimal}\,, \tag{4.7}$$

where i is the sample index of the time series. The minimization problem has been solved by means of a simple grid search.

The procedure has been successfully tested with synthetic data from different complex earth models. Fig. 4.5 gives a real-data example for a deep earthquake in the Tyrrhenian Sea (4. January 2001, z=350 km, M=4) recorded by a wide-band ocean bottom station (OB10) deployed in a depth of 2569 m right above the event ($\varphi \approx 0°$, see for technical and experimental information Dahm et al., 2002, 2004). The pressure (P) and the vertical ground velocity (v_z) show a clear onset of the P-wave at about 0s and the first water layer multiple PwP at about 3.5 s. Multiple reflected energy from sedimentary layers is present between the P and PwP phase. The sensor system transfer function has been deconvolved before the estimation of a calibration factor of 0.4 for the pressure signal. As a result, the signal energy on the downward propagating wave D_1^P is approximately zero before the arrival of the first multiple reflection at about 3.5 s although a small time window of only about 1s has been used to minimize the trace. From this and other examples we conclude that the calibration with a factor which is independent of the frequency is already sufficient for deep earthquake data. A more complex procedure and frequency dependent sensitivities (e.g. Muijs et al., 2004) may be advantageous when given sensor transfer functions are unknown or wrong.

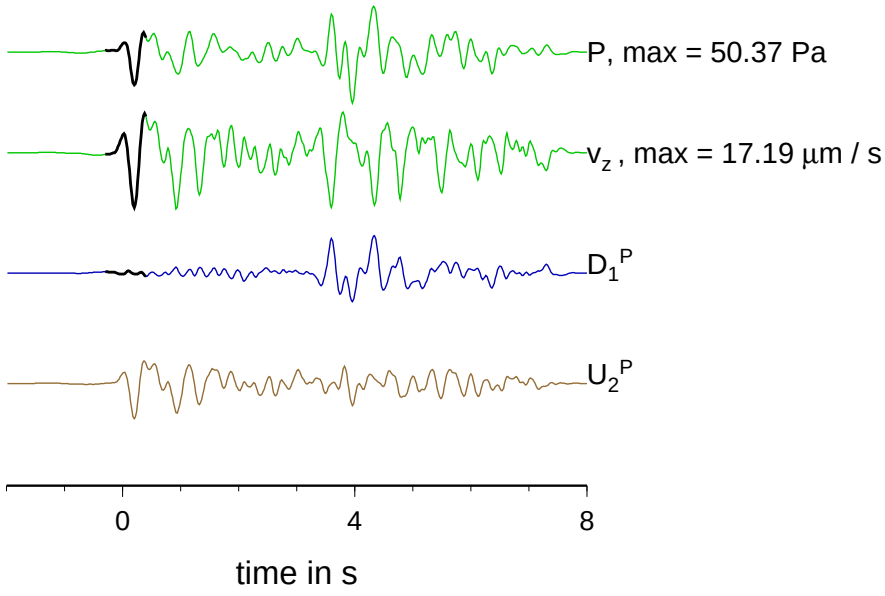

Figure 4.5: Data from the 4 January 2001 deep earthquake are plotted. (Lat = 38.907°, Lon = 14.881°, z= 279 km, $\varphi_2 = 0°$). The upper two traces show the pressure (P) and the ground velocity (v_z). Below the decomposed downgoing wave in the water is plotted (D_1^P). The time window used to estimate the hydrophone calibration factor is indicated as bold line, i.e. the sum of the squared amplitudes on the bold-line section of trace D_1^P have been minimized. The bottom trace is the decomposed upgoing wave in the sediment layer (U_2^P). The shown traces of D_1^P and U_2^P are used to estimate the impedance contrast through the cross correlation technique CC2 (s. Fig 4.12).

4.2.2 Impedance contrast

The estimation of the seafloor properties is done with equation 4.6 after the calibration factor is known and the data of the hydrophone is corrected for. Using synthetic data we tested different approaches which are:

1. the minimization of the signal energy at the arrival time of the first multiple in the upgoing wavefield below the surface (MinEng).

2. the zero-lag cross correlation between upgoing wavefield below the surface and downgoing wavefield above the surface (CC1).

3. the squared version of 2. (CC2).

The difficulty for all approaches are existing multiple sediment reflections and the overlap of the multiple water reflection with them.

Impedance contrast by minimizing the energy

Multiple water reflections vanish on the upgoing wavefield below the surface with the right seafloor properties. It is obvious to minimize the energy of the multiple water reflections. In real data only the first water reflection is visible. Higher reflections have only small amplitudes and are hidden by noise and other phases. Therefore only a short time window around the first water reflection is chosen. The time window ranges from sample N1 to sample N2 and the energy of the waveform in the time window is minimized:

$$F_2 \quad = \quad \sum_{i=N1}^{N2} U_{2i}^k \, U_{2i}^k \qquad \text{is minimal}\,. \tag{4.8}$$

Most problems occur with regard to the choice of the right time window because of the wave energy arriving from different directions. The upgoing wavefield in the subbottom is calculated by (see equation 4.6):
$U_2^P = P + F_z^P \cdot v_z$
with $F_z^P > 0$. For a wave arriving from above pressure and vertical ground velocity show opposite onsets. Therefore the wave vanishes on U_2^P. The wavefield decomposition attenuates the wave energy arriving from above like multiple water reflections. Any energy coming from a different direction than the multiple water reflection is not totally attenuated and remains in the upgoing wavefield in the subbottom U_2^P. The Energy arriving from below like the direct P-wave and the sediment reflection shows equal onsets for pressure and vertical ground velocity. Therefore, these phases are amplified.

To estimate the seafloor properties the wave energy is minimized. Therefore the time window should only include the first water reflection and no sediment reflections and noise. The effect of different time windows is demonstrated in Fig. 4.6 for noise-free synthetic data calculated with the reflectivity method (see chapter (3.2.2). A two layer model upon a half space was used (see tab. 4.1). As it can be seen the estimation of the seafloor properties is very sensitive to the chosen time window. Two different time windows are used: a short one of 0.4 s (left) and a long one of 0.8 s (right). Only the energy arriving from above occurs in the short time window but the energy arriving from below occurs additionally in the long time window. For both cases the misfit function is plotted against the relative impedance (bottom) and the two traces of the downgoing wavefield in the water layer and upgoing wavefield in the subbottom is shown (top). In the first case (short time window) the right impedance is estimated. The first water reflection is attenuated (red line). In the case of the long time window a wrong impedance is estimated. The use of this impedance for the wavefield decomposition leads

to remaining energy inside the time windows.
A deep frequent P-wave or a long lasting P-coda would have a similar effect because energy arrives from below the station. Noise is also disturbing since noise energy arrives not only from above but from different directions.
For real data it is even harder to find the right time window since waveforms are more complicated.

Table 4.1: Three layer model over half space.

	thickness	P-velocity	density
water layer	3.0 km	1.5 km/s	1.0 g/ccm
1th layer	0.4 km	1.75 km/s	1.7 g/ccm
half space		4.4 km/s	2.5 g/ccm

Impedance contrast by zero-lag cross correlation

The wavefield decomposition is applied with the right subbottom impedance if
a.) only the P-wave occurs on the upgoing wavefield in the subbottom U_2^P and water multiple reflections are attenuated and
b.) only the water reflections occur on the downgoing wavefield in the water layer D_1^P and the P-wave is attenuated (see Fig. 4.4).
Therefore, a zero-lag cross correlation between U_2^P and D_1^P vanishes for the right impedance contrast:

$$F_2 \;=\; \frac{\sum_{i=1}^{N} D_{1i}^k \, U_{2i}^k}{\sqrt{(\sum_{i=1}^{N} D_{1i}^k \, D_{1i}^k)}\,\sqrt{(\sum_{i=1}^{N} U_{2i}^k \, U_{2i}^k)}} \quad \text{is minimal}\,. \tag{4.9}$$

A similar formulation is a zero-lag cross correlation between the squared traces of U_2^P and D_1^P:

$$F_2 \;=\; \frac{\sum_{i=1}^{N} \left[D_{1i}^k \, U_{2i}^k\right]^2}{(\sum_{i=1}^{N} D_{1i}^k \, D_{1i}^k)\,(\sum_{i=1}^{N} U_{2i}^k \, U_{2i}^k)} \quad \text{is minimal}\,. \tag{4.10}$$

The advantage in comparison to the estimation by minimization of the energy is that the cross correlation is independent of a time window if it is long enough. For a simple model with a water layer over a half space both show the same result but the minimum of the single cross correlation is much harper than the minimum of the squared cross correlation (Fig 4.4). If a sediment layer is present the situation is more complicated (Fig 4.7). Sediment reflection occur on both traces, U_2^P and D_1^P. Therefore, the zero of the misfit function is shifted for the single cross correlation (Figure 4.8). The value of

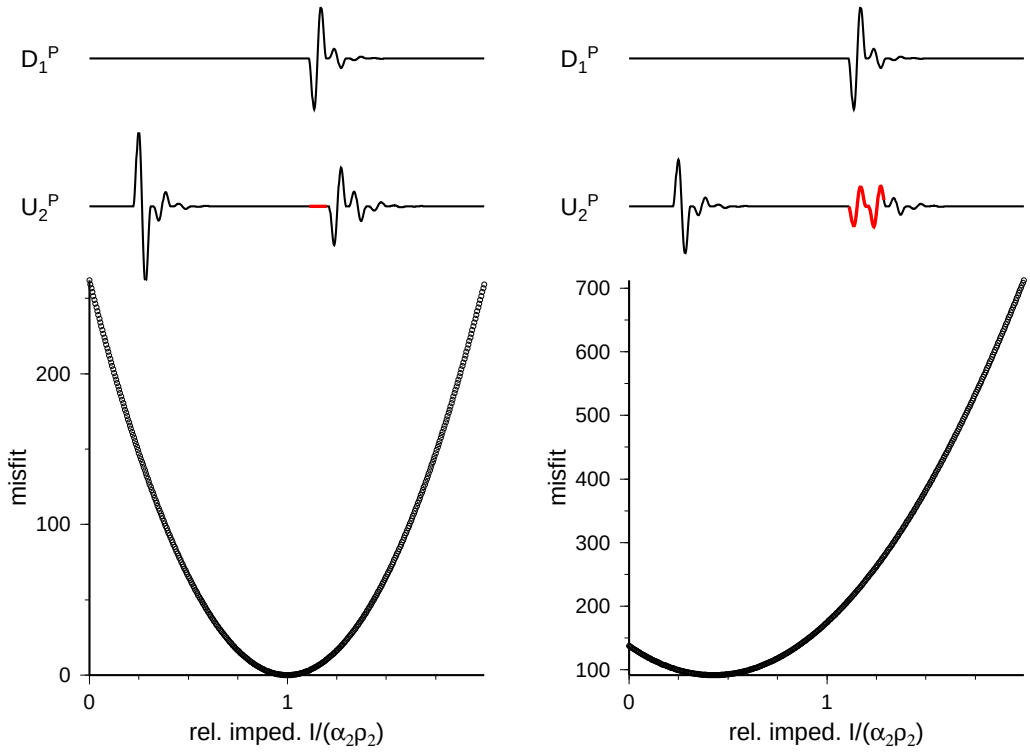

Figure 4.6: The estimation of seafloor properties through the minimization of the wave energy applied to synthetic data. The duration of the P-wave is 0.4 s. A sediment reflection occurs with a two-way-time of 0.46 s after first water reflection. **Top:** The downgoing wavefield in the water layer and the upgoing wavefield in the subbottom derived by applying the wavefield decomposition to synthetic data using the estimated impedance contrast. The red line indicates the chosen time window. The start time of the time window is the onset of the first water reflection. Left: a short time window (0.4 s) includes only the first water reflection. No energy of sediment reflections occurs in the time window. Right: a long time window (0.8 s) includes energy of first water reflection and sediment reflections. **Bottom:** The misfit function is plotted against relative impedance. Left: The minimum of the misfit function is, for the short time window, at 1, i.e. the right impedance is estimated for the seafloor. Right: The minimum of the misfit function is, for the long time window, at about 0.6, i.e. the impedance of the seafloor is wrongly estimated with an relative error of 40%

the minimum of the misfit function does not vanish and the minimum is also shifted for the squared cross correlation (Figure 4.8). In general the shift is general smaller for the squared cross correlation than for the single cross correlation (Figure 4.9). Therefore, the squared cross correlation is used to estimate the seafloor properties of the deep events.

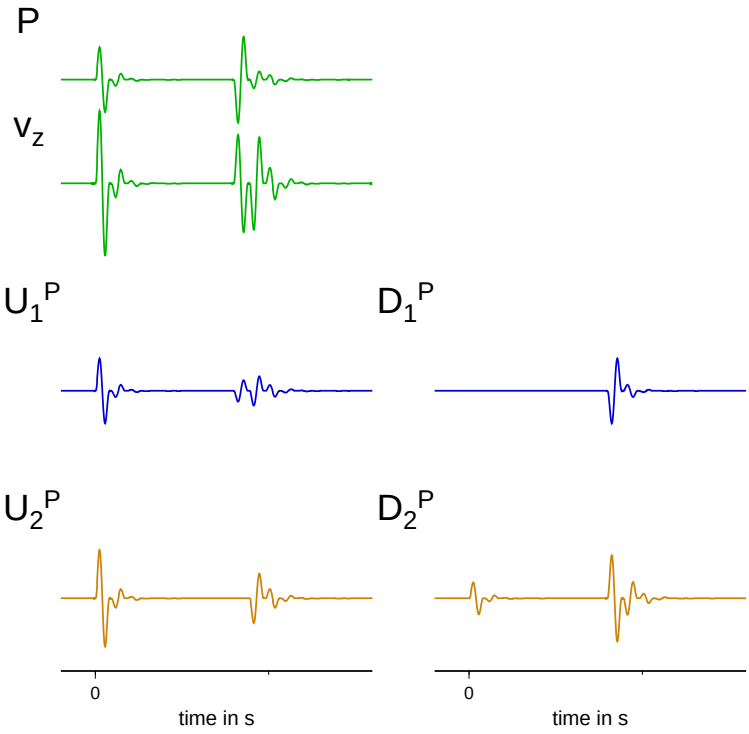

Figure 4.7: Synthetic seismogram for a model with one sediment layer. The wavefield decomposition is applied using the right impedance contrast.

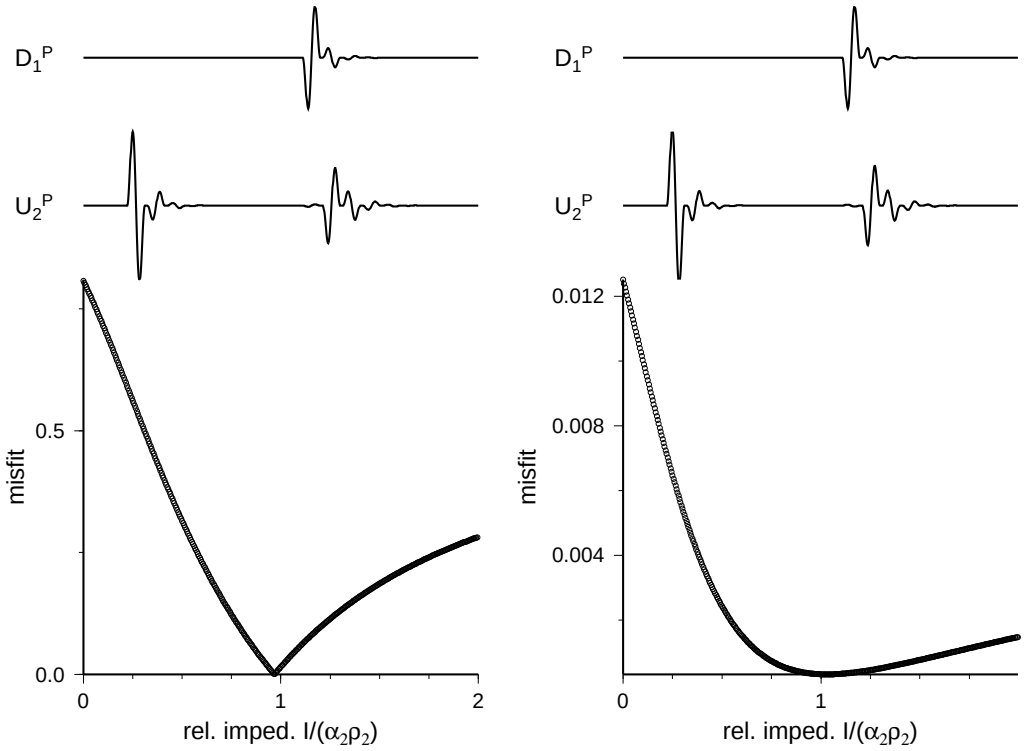

Figure 4.8: **Left**: the single cross correlation. **Right**: the squared cross correlation. **Top**: the traces of the downgoing wavefield in the water layer D_1^P and the upgoing wavefield in the subbottom U_2^P **Bottom**: misfit function against the relative impedance.

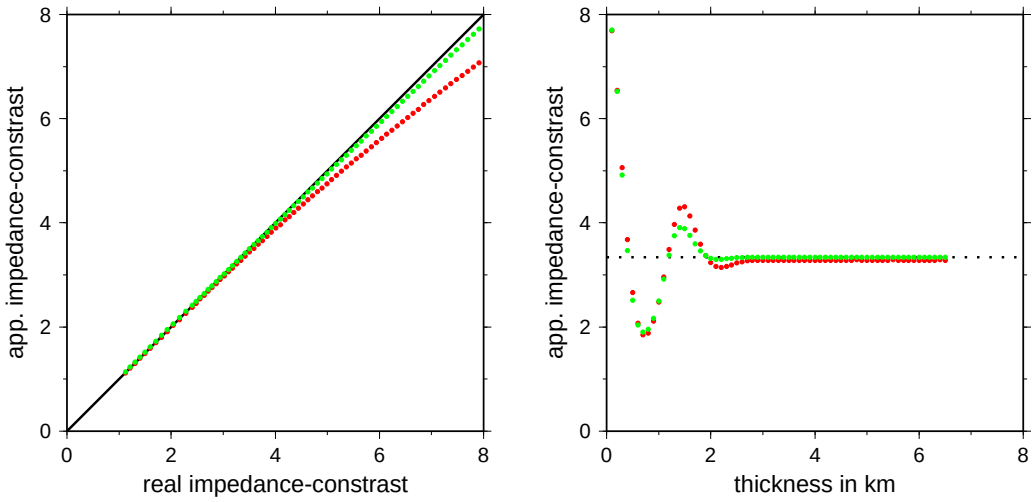

Figure 4.9: Synthetic data: the half space has double impedance than subbottom layer.
Left: apparent impedance plotted against real impedance of second layer.
Right: apparent impedance plotted against thickness of subbottom layer.

Influence of noise

The influence of noise to the estimation of impedance contrast is an important question. The underground model from Fig 4.4 is used to calculate synthetic seismograms. Synthetic noise is generated by a uniformly distributed pseudo-random number algorithm. The pseudo-number trace is convolved with the time function $\sin(2\pi t/7s) * exp(-(4 * t/21s)^2)$ to produce colored noise and is multiplied by the noise amplitude. Noise is added to the synthetic seismogram as ground displacement.

It is assumed that the noise is generated by several spatial distributed sources like civilisatoric noise, waves, fauna etc.. The superposition of the single sources is different for the two sensors due to the directivity of the sensors (isotropic versus directional). Therefore less coherence between the noise on the hydrophone and the seismometer is excepted, but the amplitude-spectra should be similar. Thus two pseudo-number traces - one for each (hydrophone and seismometer trace) - with the same amplitude are generated. The signal-to-noise-ratio (SNR) is about 7 (maximum amplitude ratio for noise and the P-onset).

The result for the estimation of the seafloor properties are shown in Fig. 4.10 and 4.11.The synthetic traces for pressure and the vertical ground velocity is shown in Fig. 4.10. The separated upgoing and downgoing wavefields are also plotted. The right impedance contrast was used.
Fig. 4.11 shows the misfit functions for the two cross correlation approaches for the estimation of the seafloor properties. All misfit functions show a shift of the minimum. The shift is small for the squared cross correlation approach CC2. The minimum is at $0.995\rho_2\alpha_2$, i.e. at 99.5 % of the impedance of the subbottom. The shift is larger for the single cross correlation. The minimum is at $0.74\rho_2\alpha_2$. Depending on the noise the shift varies, but the trend that the single cross correlation is more sensitive to noise than the squared cross correlation remains.

To remove the multiple water reflections on the upgoing wavefield it does not seem important to know the correct seafloor properties since the wavefield decomposition with the wrong impedance contrast attenuates the water multiples.

4 January 2001 deep event

The estimation of seafloor properties is done with equation 4.6 after the calibration factor is known and the hydrophone data is corrected for. The minimization of the square of the zero-lag cross-correlation between the upgoing wave in the sediment and the downgoing wave in the water layer was used. The length of the selected time window is uncritical and has only be chosen roughly to include direct waves and water multiples (see Fig 4.5). Either $k = P$, v_z or v_r can be taken for estimation of the impedance contrast. Theoretically, when rays with $\varphi \neq 0$ are used, the simultaneous use of all three

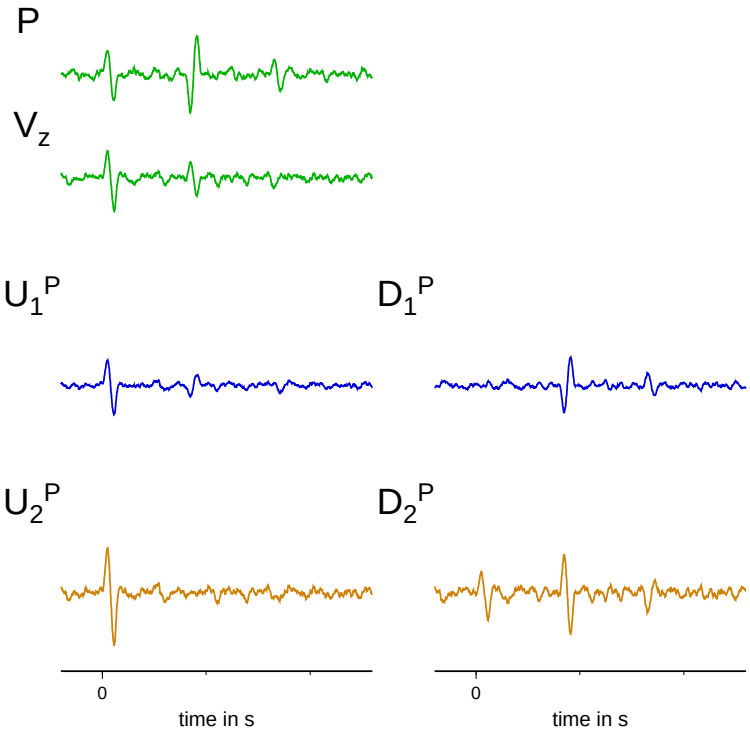

Figure 4.10: The synthetic seismogram with noise. The wavefield decomposition is applied using the right impedance contrast.

wavefield components enables the estimation of α_2, β_2 and ρ_2. However, due to relatively large noise on horizontal components, we have been able to give estimates for $\rho_2\alpha_2$ only. Again the minimization problem has been solved by a grid search approach.

The decomposed upgoing wave U_2^P in the sediment layer (Fig. 4.5) shows a small or zero PwP-phase at 3.5 s as predicted by theory. However, a secondary phase arriving slightly later, at about 3.8 s, is now visible and was hidden in the original traces. This phase must originate from the mud-sediment interface below the station.

Fig. 4.12 shows the misfit for the hydrophone calibration factor f and for the impedance contrast F_p^P/F_p^P with respect to water. In this case the impedance contrast is $\rho_2\,\alpha_2\,/\,\rho_1\,\alpha_1 = 1.2$.

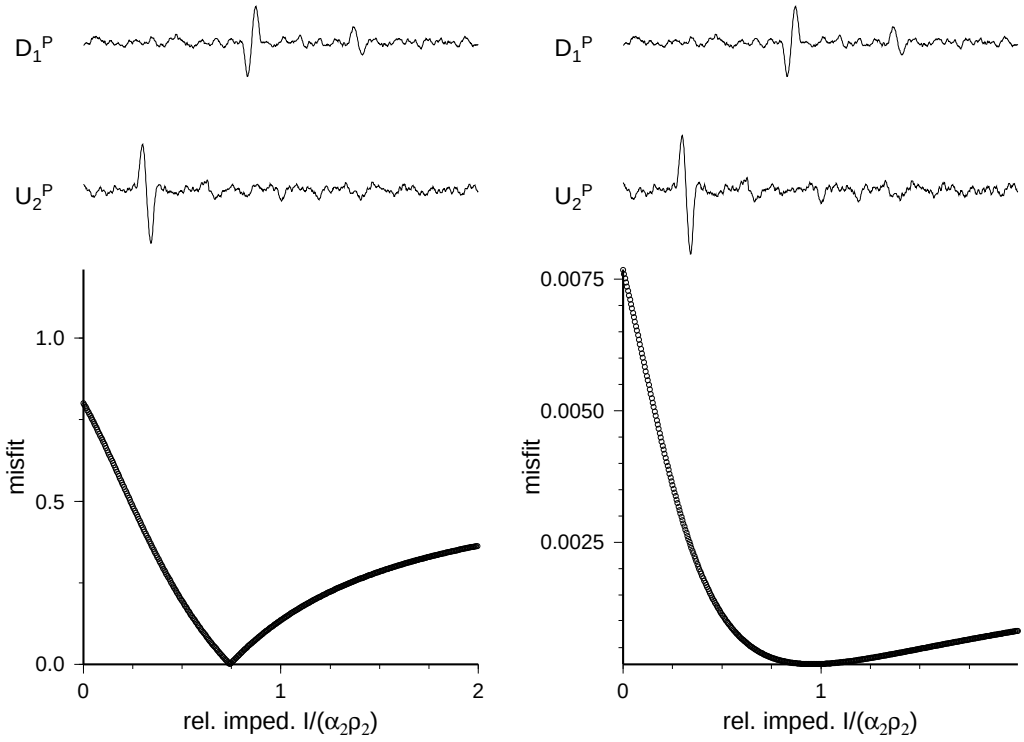

Figure 4.11: **Left**: the single cross correlation. **Right**: the squared cross correlation. **Top**: the traces of the downgoing wavefield in the water layer D_1^P and the upgoing wavefield in the subbottom U_2^P. The estimated impedance contrast is used for the wavefield decomposition. **Bottom**: misfit function against the relative impedance.

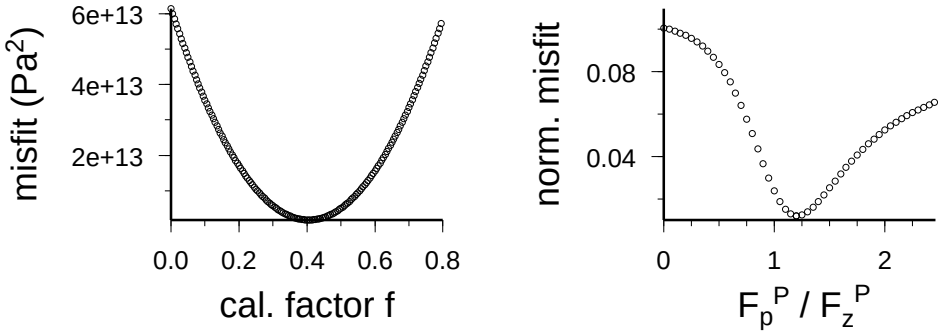

Figure 4.12: Misfit function is plotted against the calibration factor and the impedance contrast as estimated by a grid search to find optimal values for the decomposition in Fig. 4.5. A hydrophone calibration factor of $f = 0.4$ was estimated and a seafloor impedance contrast of $F_p^P/F_z^P = \rho_2\alpha_2/\rho_1\alpha_1 = 1.2$.

4.3 Deep local earthquakes

The wavefield decomposition is applied to the 13 deep earthquakes which have occurred in the Tyrrhenian Sea (see chapter 1.3) to estimate the seafloor properties and to attenuate the water layer multiples.

First, the data is restituted to pressure (hydrophone) respectively to ground velocity (seismometer) and high pass filtered with a corner of 1.7 s to attenuate mircoseimic noise is applied to the data. On the vertical component a crosstalk signal occurs from the horizontal components. In a second step the crosstalk signal is removed. The wavefield decomposition is calculated for these data. A vertical incidence is assumed as the dependency of the angle of incidence is weak (see Fig. 4.3).

Attenuation of crosstalk signal
The horizontal traces are rotated into a coordinate system which consists of the radial and transversal component. Crawford and Webb (2000) developed an approach to attenuate energy on the vertical component caused by a crosstalk from the horizontal traces. Frequency dependent correlation coefficients between the vertical and the horizontal component are estimated using noise traces. A filter designed with the correlation coefficients is applied to the horizontal components This resulting crosstalk trace is subtracted from the the vertical component.

An approach similar to Crawford and Webb (2000) is used to attenuate the crosstalk signal observed in the Tyrrhenian sea. Instead of using a time window with only noise energy a time window between the P- and PwP-phase is chosen containing the crosstalk signal but no P- or PwP-energy. The time window starts about 0.3 s after the maximum of the P-phase and last 2.74 s for OB10 and 2.00 s for OB11 (see Fig. 4.13). The quotient of the Spectrum of the time window on the vertical $\bar{Z}_t w(\omega)$ and the radial trace $\bar{R}_t w(\omega)$ is calculated and multiplied with the spectrum of the whole radial traces $\bar{R}(\omega)$. The result is the spectrum of the crosstalk signal $\bar{G}(\omega)$:

$$\bar{G}(\omega) = \frac{\bar{Z}_t w(\omega)}{\bar{R}_t w(\omega)} \bar{R}(\omega) \tag{4.11}$$

The vertical component is corrected by subtraction of the crosstalk signal:

$$v_{z,corr.} = v_z - G \tag{4.12}$$

Some high frequent energy remains on the traces due to spectral singularities. Therefore, a low pass filter is applied. The corner frequency used was 5 Hz for OB10 and 3.5 Hz for

OB11. Fig. 4.13 shows the attenuation of the crosstalk signal. The PwP-onset is hidden by the crosstalk signal on the uncorrected, vertical trace v_z (second traces from bottom). After the correction a PwP-phase is visible on the corrected vertical trace $v_{z,corr.}$(second traces from top).

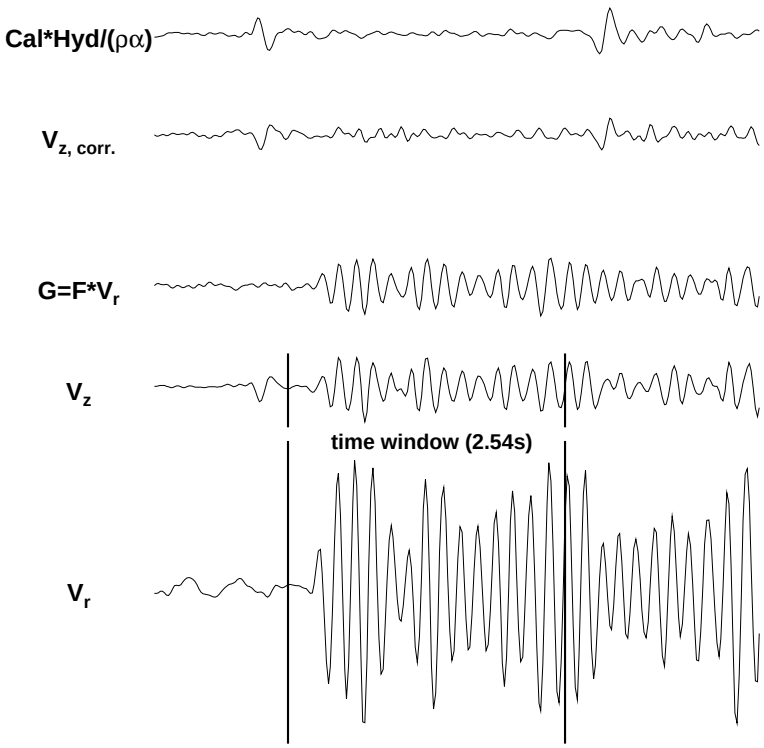

Figure 4.13: At the bottom the vertical and the radial component of an earthquake is plotted. The two vertical lines indicate the time window used for the attenuation of the crosstalk signal. The middle traces show the crosstalk signal G. At the top the hydrophone and the corrected vertical trace are plotted. All traces have the same zoom. The hydrophone is additionally normed with the impedance of water $\rho\alpha$ and the Calibration factor Cal.

A wavefield decomposition has been applied to estimate seafloor properties and to attenuate water layer multiples, e.g. as a preparation for structural or source analysis.

Figs. 4.14 and 4.15 show the decomposition result at two nearby stations OB10 and OB11 about 20 km apart. A similar pattern is observed for both stations. The incoming wavefields (P) show strong water layer multiples some seconds after the first arrivals. After the wavefield decomposition, the downgoing and upgoing wavefields are well separated. The downgoing wavefield D_1^P has a very small or zero energy at the time of the first upgoing P-wave but has strong energy at the arrival times of water layer multiples.

The water layer multiples arrive at about 3.5 s and 2.5 s for stations OB10 and OB11. This corresponds to a water depth of 2569 m and 1893 m respectively. The rays of all used earthquakes have been nearly vertical.

A comparison between the original P-waveform (P) and the decomposed, upgoing wavefield (U_2^P) verifies that the original P-phase waveform is not distorted or changed by the decomposition technique (see summed traces in figs. 4.14 and 4.15). In contrast, the water layer multiple is vanishing or attenuated in the sum of the upgoing trace. In the sum trace $\sum_U$ in Fig. 4.14 and 4.15 a small-amplitude phase arrives about 0.25 s respectively 0.08 s after the arrival time of the PwP-phase, which is here interpreted as a structural phase from a soft mud layer.

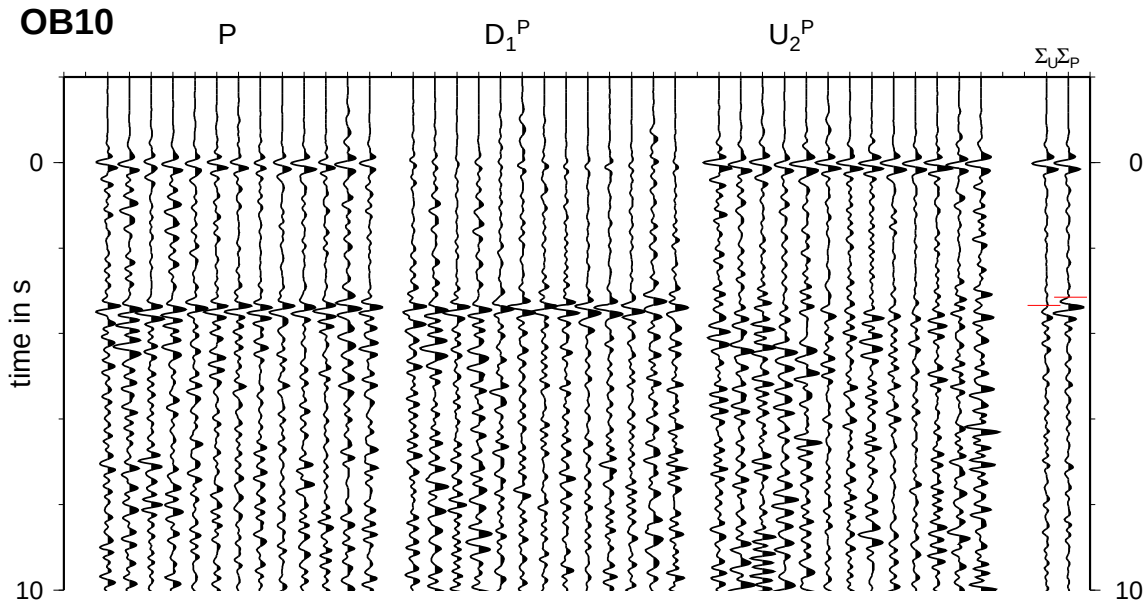

Figure 4.14: Seismograms from local earthquakes between 100 km and 400 km depth have been decomposed for station OB10 at 2569 m depth. A common calibration factor of 0.36 was used. The crosstalk signal has been removed from the vertical trace before decomposition, and horizontal traces have been discarded because of increased noise levels. Here, the incoming waves (P, left), the downgoing waves in the water layer (D_1^P) and the upgoing waves in the sediment layer (U_2^P) are plotted. A six-pole Butterworth bandpass filter with corners at 1.5 Hz and 5.0 Hz has been used (two passes) and traces have been normalized to their maximum. Sum traces of P and U_2^P are plotted on the right side. The onset of the PwP-Phase an of the sediment reflection are marked in red.

For each event the impedance contrast is estimated. The median of impedance contrast

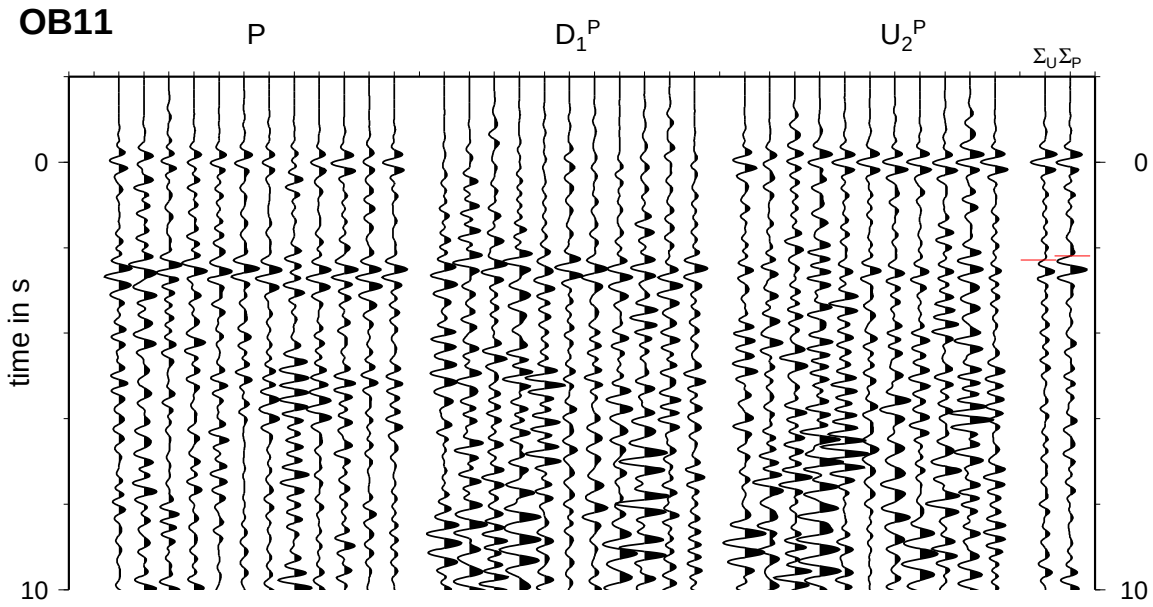

Figure 4.15: The same plot as in Fig. 4.14 but for station OB11 at 1893 m depth, which was deployed in about 25 km from OB10. A six-pole Butterworth bandpass filter with corners at 1.5 Hz and 3.5 Hz has been used (two passes). A common calibration factor of 0.25 was estimated.

for the site of OB10 is $\rho_2\alpha_2/\rho_1\alpha_1 = 1.3$ with a one-σ confidence interval between 0.96 and 1.75. For the site of OB11 it is 1.5 with a one-σ confidence interval between 0.67 and 3.25 (Fig. 4.16). The scatter is larger at OB11. The relatively small values indicate that the uppermost seafloor layers in the Tyrrhenian Sea are very muddy and unconsolidated. For some events impedance contrasts below one are found, which may theoretically be explained by the presence of gas. However, the scatter of values is more likely induced by noise in the data and the narrow band spectrum of the traces.

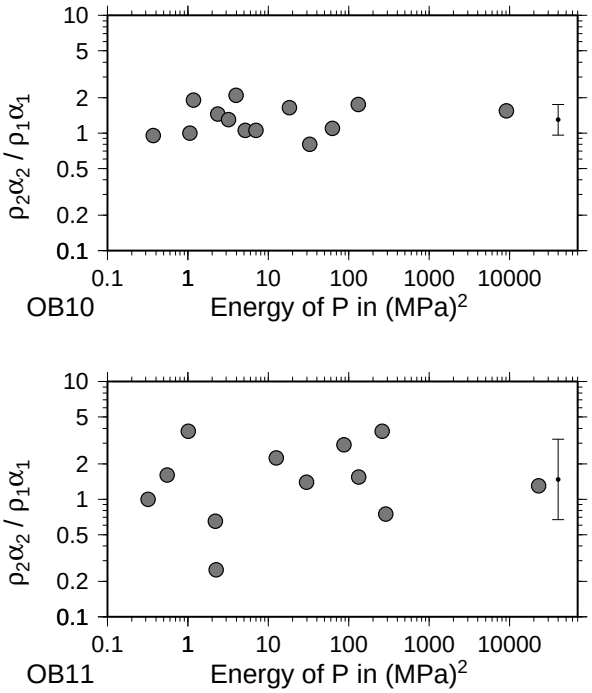

Figure 4.16: Impedance contrast $\rho_2\alpha_2/\rho_1\alpha_1$ as estimated from different earthquakes plotted as a function of the energy of the incoming P-wave. The bar and error range indicates the median and one-sigma confidence intervals. The left plot is for station OB10, the right for OB11.

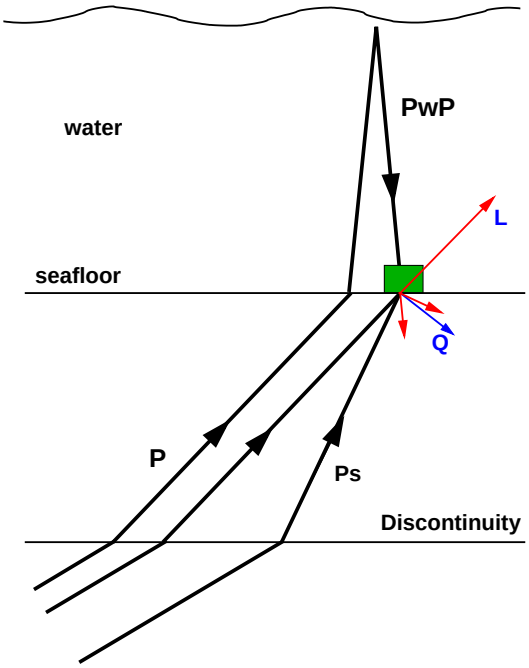

Figure 4.17: A teleseismic P-wave hits a discontinuity, from where a P-wave and a converted Ps-wave will ascend polarized in L- and Q-direction (blue arrows) respectively. Ray paths are indicated by black lines, polarizations by red arrows at the ocean bottom station. The multiple water-layer reflections PwP have a different polarization angle than the P-wave and will therefore produces in Q-direction a signal. This disturbs the interpretation of the receiver-functions.

4.4 Receiver-functions

The receiver-function method has been successfully applied for several years. Receiver-functions are calculated to investigate the structure of the crust and upper mantle and to determine the morphology of the 400 km and 660 km mantle discontinuities (e.g. Li et al., 2003; Vergne et al., 2003; Shen et al., 2003). The occurrence of P-to-S converted waves in the coda of the P-wave was first studied by Vinnik (1977) and Burdick and Langston (1977). Amplitudes of only 5% to 10% of the P-wave are expected for the converted waves. In the cylindrical coordinate system of the Z-R-T axis of the station the P-wave and the converted waves Ps occur both on the vertical component Z and the radial component R. Z stands for the vertical, R for the radial and T for the transversal component. Therefore, the converted waves Ps can be hidden in the coda of the P-wave. To separate the P-wave and the converted waves Ps and to enhance their amplitudes the three component data (Z-R-T) are rotated into a ray depended coordinate system (L-Q-T, Fig. 4.17). The P-wave now occurs on the longitudinal component L and the converted Ps-waves on the Q-component. To enhance the coherence of the converted phases the P-phase waveform is deconvolved from the Q trace. The resulting trace is called the receiver function (e.g. Clayton and Wiggins, 1976; Burdick and Langston, 1977; Ammon et al., 1990; Ammon, 1992; Abers et al., 1995; Gurrola et al., 1995). P-waves should be strongly attenuated on the receiver function while the small-amplitude P-to-S converted phases should be visible.

One major difference between land- and ocean bottom recordings is the occurrence of multiple reflections in the oceanic water layer. These multiples arrive at the station as

downgoing waves having a different polarization angle compared to the incidence angle of the incoming, upgoing P-wave (Fig. 4.17). Therefore, water layer multiples have non-vanishing amplitudes on the receiver function (Q-component). The non-vanishing water-layer multiples will attenuate slowly whenever the impedance contrast between water and subsurface sediments is strong.

In order to investigate the ocean-layer effect on receiver-functions, synthetic seismograms are calculated using a Thompsen-Haskell-propagator (program "qseis" from Wang, 1999) for a 3 km thick water layer over a two-layer crust embedded in a global velocity model (AK135 (Kennett and Engdahl, 1995), Fig. 4.18; a sediment layer with $v_P = 2500$ m/s, $v_S = 1440$ m/s and $\rho = 2000$ kg/m^3 and a basement layer with $v_P = 6800$ m/s, $v_S = 3900$ m/s and $\rho = 2900$ kg/m^3). The sampling rate is 2.5 Hz and the source-time function is a normalized half sinusoid with a duration of 2.5 s. The sources have been placed in epicentral distances between 30 and 90 degrees at a depth of 500 km in order to suppress strong surface-waves (Fig. 4.18, Fig 4.19). In this case the depth-phase pP has a delay time > 90 s and does not disturb the converted phases from mantle discontinuities in 400 km and 660 km depth at a delay time of about 40 s and 60 s (see Fig 4.19).

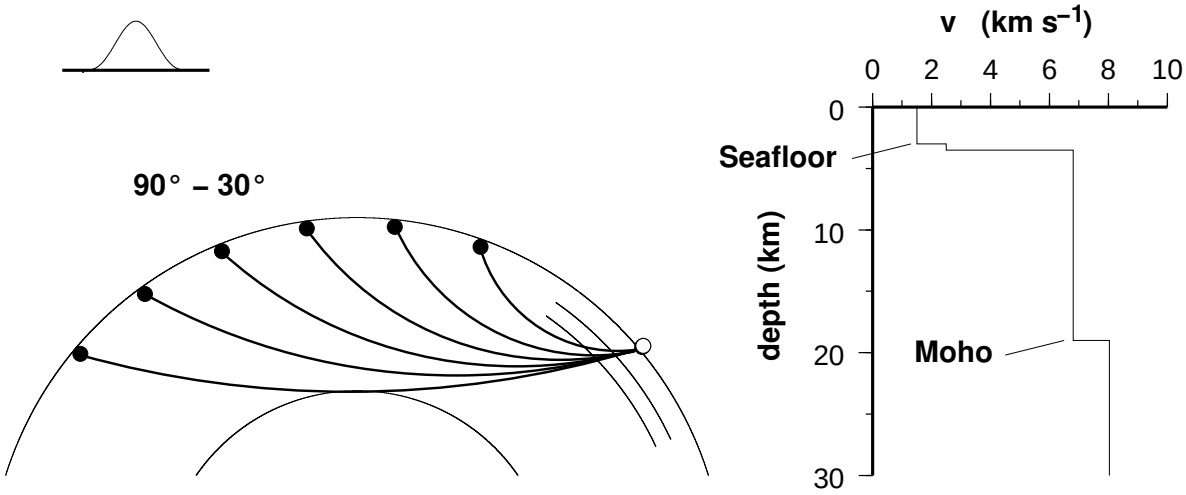

Figure 4.18: Geometry (bottom left) and source-time function (top left) for the synthetic data test. Sources (black circles) have been placed between 30° to 90° epicentral distance from receiver (white circle). Mantle discontinuities are plotted below the receiver.
The P-wave crust model is plotted on the right; AK135 velocities (Kennett and Engdahl, 1995) have been used below 30 km.

Traces are rotated into the ray dependent coordinate system L-Q-T. The axes of the L-Q-T coordinate system represents the direction of the P-wave (L), the SV-Wave(Q) and the SH-wave(T). In the absence of anisotropy the energy of the waves which are

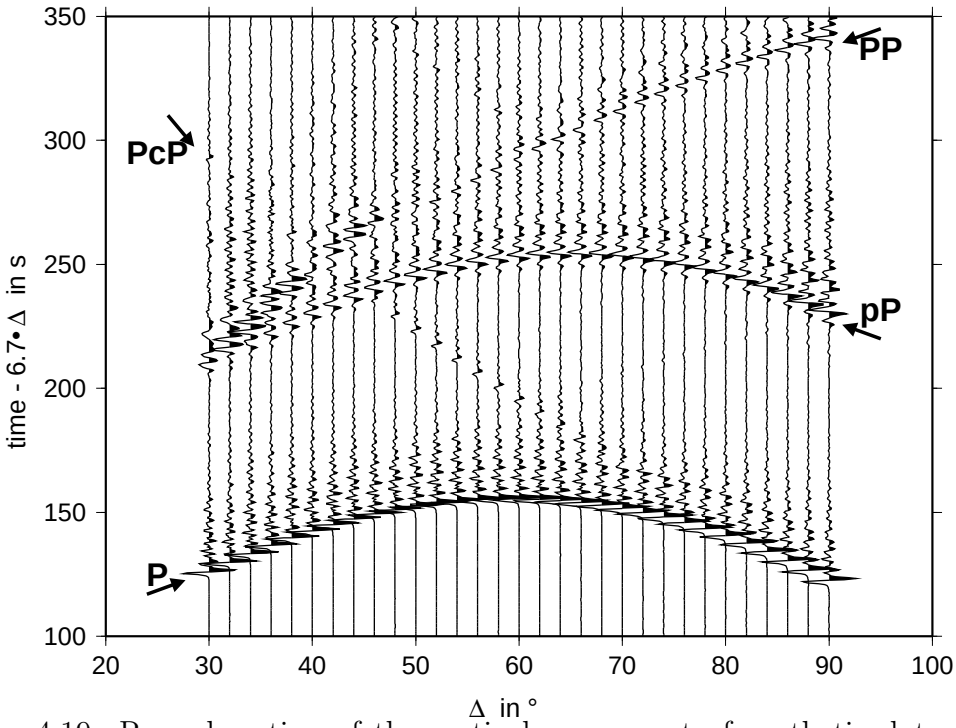

Figure 4.19: Record section of the vertical component of synthetic data for an epicentral distance Δ between 30° and 90°. Time is in s and epicentral distance Δ in °.

converted from the P-waves occurs only on the Q-component. No SH-wave occurs in the coda of the P-wave. To improve the recognizability of the converted waves the waveform of the P-waves must be removed from the data. Here, a Wiener-Optimum-filter is applied to deconvolve the waveform of the P-phase from the Q-component while a time window of 80s after the P-onset is used as the waveform of the P-wave. Afterwards, I correct the receiver functions for normal-move-out (NMO) to simulate a vertical incidence (see Fig. 4.20).

A strong regular signal disturbs the receiver function. Thus, converted waves from the 400km and 660km discontinuities expected at 41.1s and 62.4s are not visible on individual receiver-functions, but may appear on the sum of the trace (Fig. 4.20 right). However, a potential morphology of mantle discontinuities would be difficult to study. Fig. 4.21 shows the corresponding "delta" functions resulting from applying the same Wiener-Optimum-filter to the L-component. The deconvolution of the waveform of the P-wave works well. Therefore, the disturbing signal cannot be an artifact of the processing process but is generated by the model. The disturbing signal has a main period of the double two-way-time of the water layer $2 \cdot T_0 = 4 \cdot h_{water}/\alpha_{water} = 4 \cdot$ 3000 m / 1500 m/s = 8 s. Please note that in figure 4.20 the traces are NMO-corrected. Thus the main period seems to differ depending on the epicentral distance but this is due to the NMO-correction. Water multiple reflections have a main period of the double two-way-time.

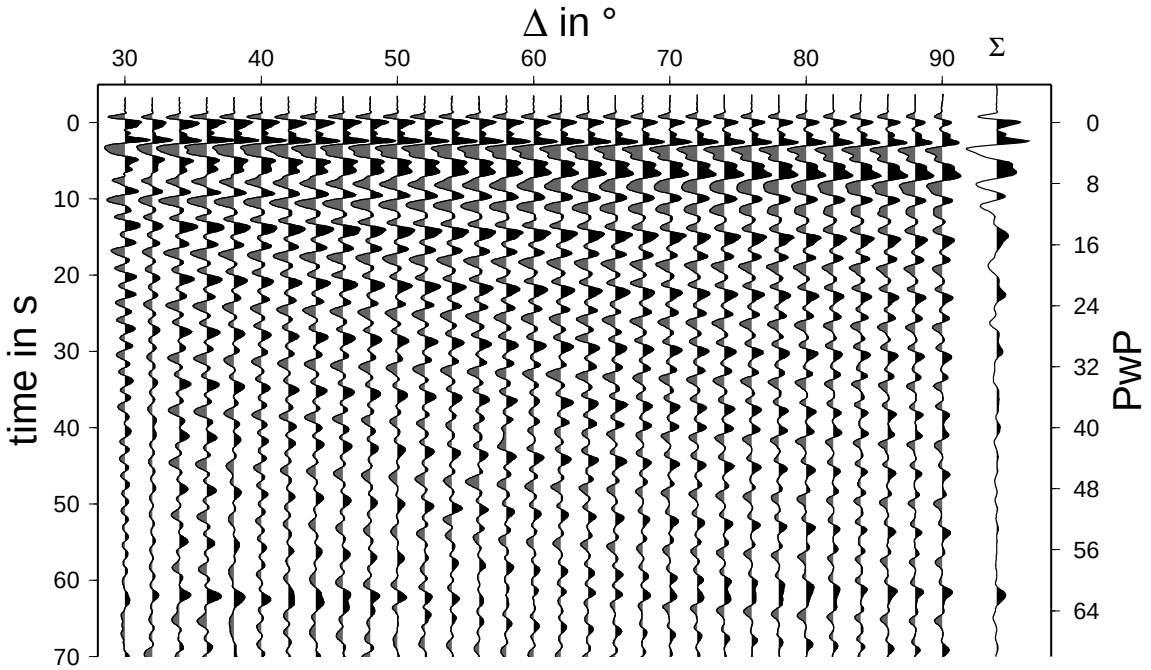

Figure 4.20: Synthetic data receiver-functions section for an epicentral distance Δ between 30° and 90°. A normal-move-out correction is applied to the traces. The summed trace Σ is plotted on the right. Ticks on the right axis indicate the recurrence time of the PwP signal. Conversion at the deep mantle discontinuities should occur at about 40 s and 62 s.

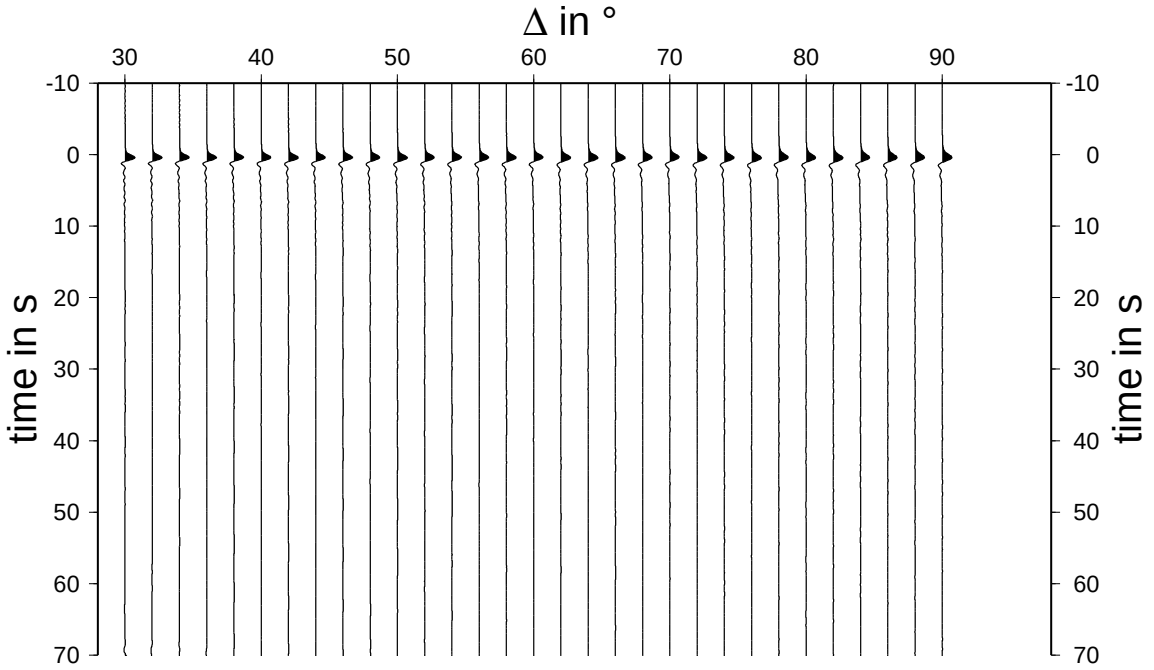

Figure 4.21: δ-function resulting from applying a Wiener-Optimum-filter to the L-component and removing the P-waveform.

Therefore, it is obvious to suggest that the water multiples disturb the receiver functions.

To prove this, the wavefield decomposition is applied to the individual synthetic recordings. The use of the decomposed upgoing wavefield to calculate receiver-function sections results in an impressing improvement (Fig. 4.22). The disturbing signal is attenuated. Converted phases from mantle discontinuities can now be identified on individual receiver-functions so that lateral variations may be studied. Additionally, the reflection at the core-mantle-boundary PcP is visible in the receiver function section.

An important question is how large the effect of multiple water reflections is relative to the frequency of the incoming P-wave. So synthetic seismograms are calculated using Brüstle-Müller-wavelets with different periods as source time functions. The receiver functions are calculated on the base from of these synthetic seismograms. As it can be seen in Fig. 4.23 the effect of the multiple water reflections decreases with period length.

The upgoing wavefield in (Fig. 4.22) has been calculated by using the correct impedance contrast at the sediment-water interface. Another important question is how sensitive the decomposed receiver functions are when a wrong impedance contrast is assumed. In Fig. 4.24 the impedance contrast to calculate receiver functions from upgoing waves has been varied. Despite a relatively large range of seafloor properties water layer multiples are efficiently attenuated.

Table 4.2: Source parameter of two teleseismic events studied.

Date	Time	Lat (°)	Lon (°)	Depth (km)	ML	Region
13.01.2001	17:33:32.38	13.05	-88.66	60	7.8	El Salvador
26.01.2001	03:16:40.50	23.42	70.23	16	8.0	India

It can be concluded that wavefield decomposition has a good potential to improve receiver function studies for submarine experiments, at least at higher frequencies. This hypothesis is tested with data collected during the Tyrrhenian Sea deployment. I found out that water layer multiples are indeed attenuated. Fig. 4.25 presents a comparison of receiver functions at two broadband land stations (VTS and WDD) and OB11, with and without wavefield decomposition. WDD is located in Malta at a distance of about 310 km and VTS in west Bulgaria at a distance of about 850 km to station OB11. Closer land-stations from the Italian peninsula or Sardinia have been discarded due to a bad signal-to-noise ratio, timing problems and apparent waveform complexities from nearby subducting slabs. Station OB10 has also been discarded because a close inspection of the hydrophone data indicated that the hydrophone sensor at OB10 was not sensitive at the low frequencies of the teleseismic data. Thus, waveform decomposition at OB10 did not lead to the expected improvements.

The receiver function of the original data shows large-amplitude multiple phases at the theoretical recurrence times as estimated from a water depth of 1893 m (Fig. 4.25). These multiples can neither be seen on receiver functions from the land stations nor when wavefield decomposition has been applied prior to the calculation of the receiver function (see OB11 UP in Fig. 4.25). The corrected and land station receiver functions show coherent arrivals interpreted as structural phases, e.g. at 3 s and at 39 s corresponding possibly to the Moho- and 400 km mantle discontinuity.

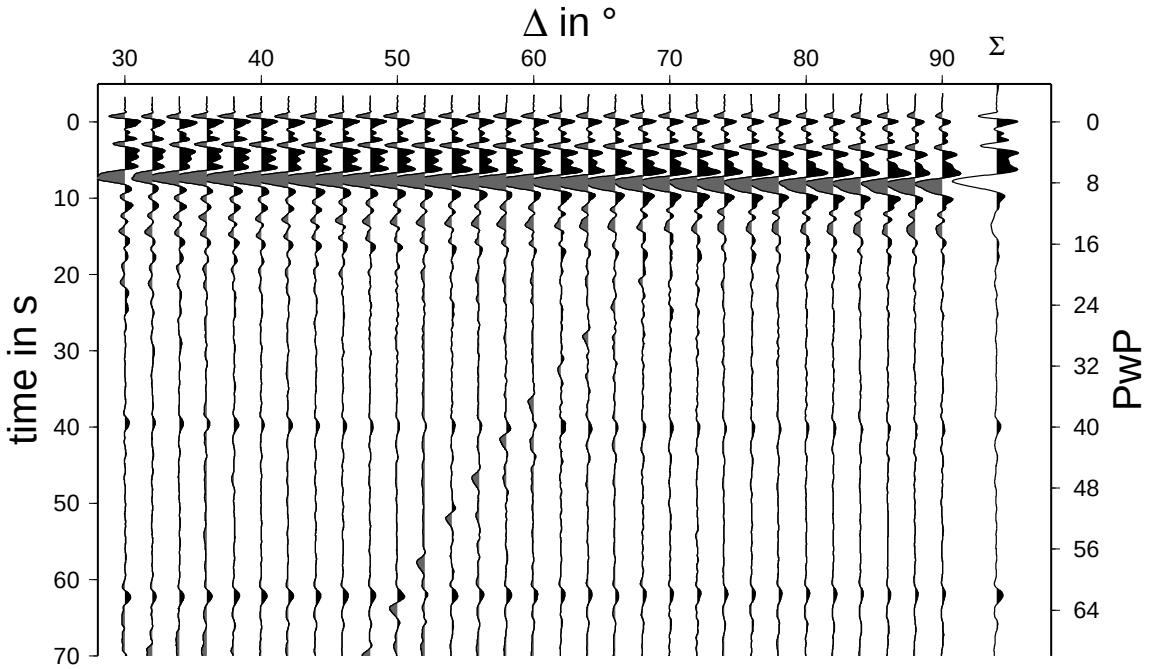

Figure 4.22:
Synthetic data receiver-functions section from Fig. 4.20 after wavefield decomposition. Conversions at the deep mantle discontinuities are visible at about 40 s and 62 s.

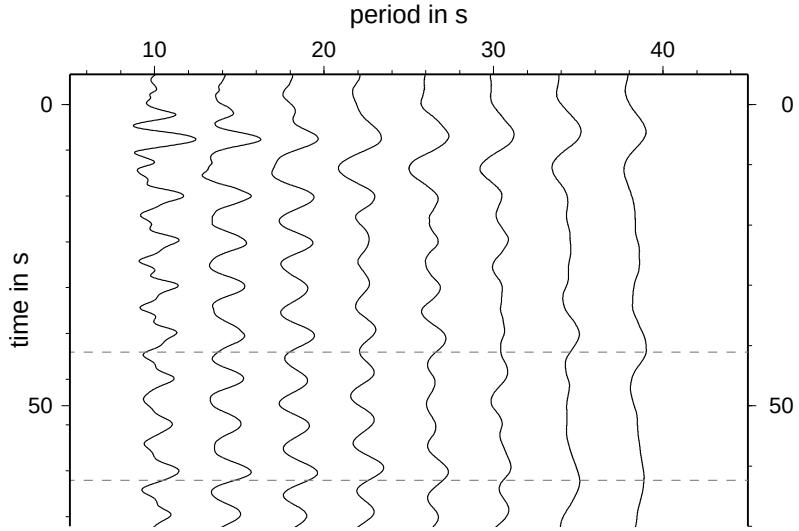

Figure 4.23: Receiver functions for synthetic data in an epicentral distance of 80°. The period of the source time function (Brüstle-Müller-wavelet) is varied between 10 s and 40 s (horizontal axis). The vertical axis is the time axis of the receiver functions. Small tick marks on the right axis indicate multiple water reflections. Dated lines indicate expected conversions at 400 km- and 660 km-discontinuities.

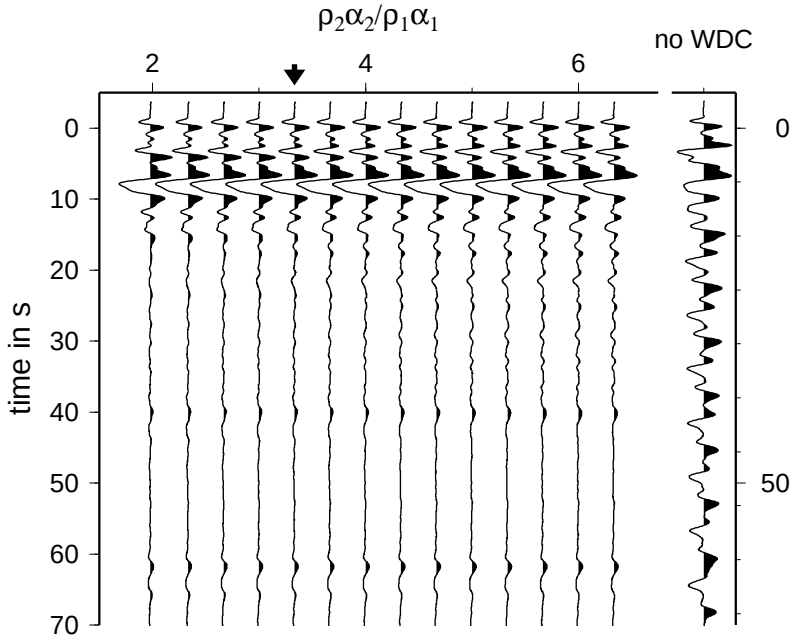

Figure 4.24: Single-trace receiver functions for a station in 80° distance as calculated for varying seafloor properties. The correct impedance contrast is indicated by a small arrow. The receiver function from the uncorrected, incoming wave is plotted at the right for comparison (no wavefield decomposition (WDC)). Small tick marks on the right time axis indicate multiple water reflections. Please note that the recurrence time of the multiple water reflections is NMO-corrected.

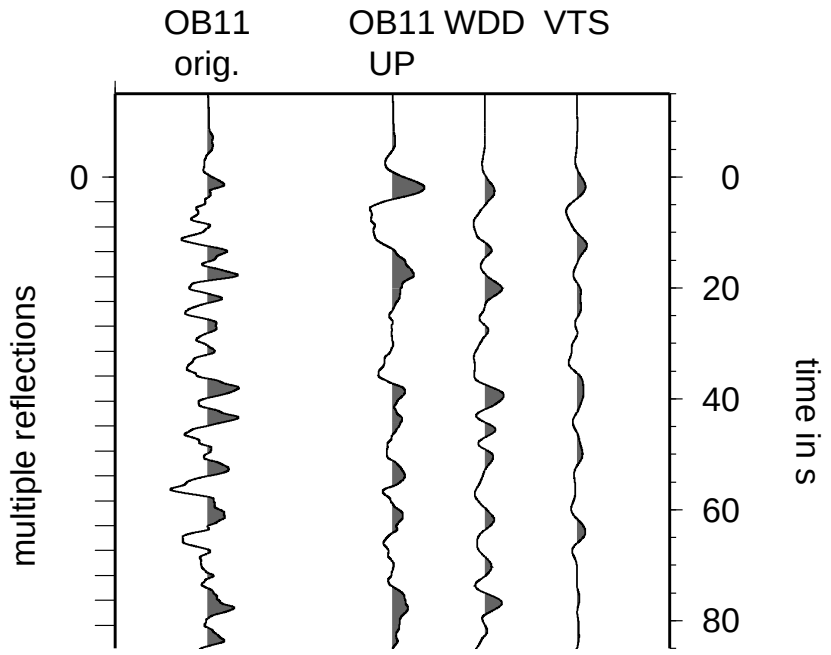

Figure 4.25: The receiver function is shown for station OB11. The India M=8.2 earthquake of Jan. 26, 2001 was analyzed (Table 4.2). The trace on the left shows the receiver function without the wavefield decomposition. The next trace is the receiver function after applying the wavefield decomposition. The receiver function of two broadband land stations VTS (Bulgaria) and WDD (Malta) for the same event is plotted on the rigth for comparison. The tick marks on the left time axis give the theoretical recurrence times of positive pulses from water layer multiples (5.0 s / 1.124 = 4.5 s).

4.5 Teleseismic travel time residuals

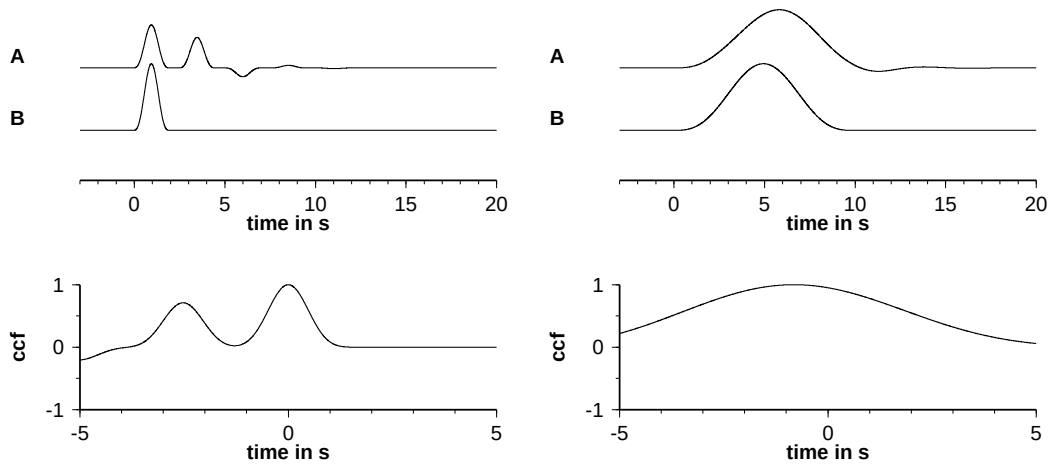

Figure 4.26: Determination of the relative time residuals between the synthetic seismometer trace of a ocean bottom station (A) and of a land station (B). Both traces are in groud motion. The normalized cross correlation function (ccf) is shown at the bottom. Two wavelet with a different period are used. **Right**: a source wavelet of a length of 2 s. **Left**: a source wavelet of a length of 10 s.

Teleseismic tomography studies are interesting for passive seismological experiments. A main prerequisite is to measure precise travel-time residuals between neighboring stations, e.g. between ocean bottom stations in different deployment depths or between ocean bottom and land stations. Correlation techniques are known to give precise estimates as long as the waveforms are similar at different stations (e.g. Allen et al., 2002; Ritter et al., 2001). However, the multiple reflections in the water layer distort the waveform and introduce systematic bias depending on the water depth and wave period (see also Webb, 1998). When uncorrected, apparent travel-time residuals may cause biased tomography velocity-models of the earth.

Synthetic seismograms for displacement and pressure are calculated for the simple model given in Fig. 4.29. The thickness of the water layer corresponds to the water depth at station OB11. An upgoing plane P-wave was initialized with a Brüstle-Müller waveform (Brüstle and Müller, 1983) with different periods from 0.5 s to 50 s. An apparent time shift was estimated by the maximum of the cross-correlation between the seismogram at the fictitious land station and the fictitious ocean bottom station. Fig. 4.26, 4.27 and 4.28 demonstrate the procedure for two different periods of source time functions: 2 s and 10 s. (A) indicates the trace of the ocean bottom sensor, (B) the trace of the land station. The cross correlation function between (A) and (B) is plotted at the bottom. In Fig. 4.26

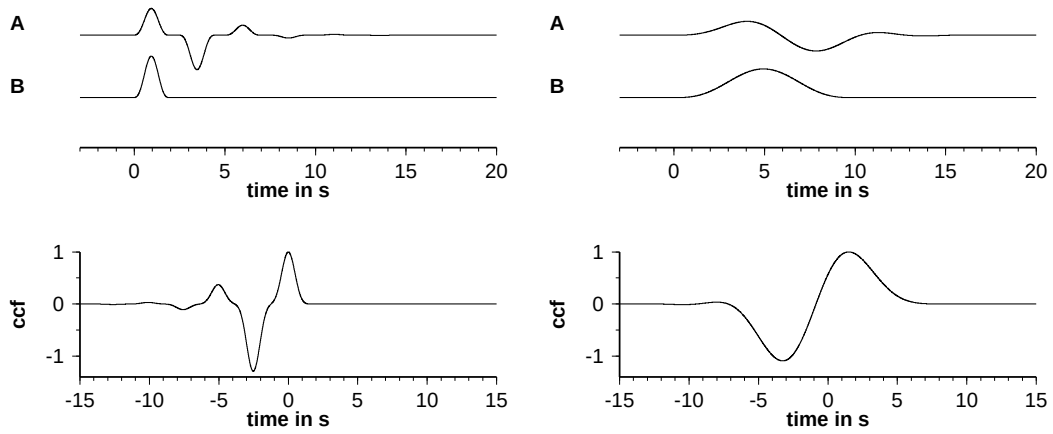

Figure 4.27: Determination of relative time residuals between the synthetic hydrophone trace of a ocean bottom station (A) and a synthetic seismometer trace of a land station (B). The traces are in pressure respectively ground velocity. The normalized cross correlation function (ccf) is shown at the bottom. Two wavelet with a different period are used. **Right**: a source wavelet of a length of 2 s. **Left**: a source wavelet of a length of 10 s.

the ocean bottom seismometer trace, in Fig. 4.27 the ocean bottom hydrophone trace and in Fig. 4.28 the upgoing wavefield from the wavefield decomposition is used. The hydrophone pressure signal was converted into an equivalent displacement by multiplying the trace with the impedance of water $I_1 = \rho_1 \alpha_1 = 1.5 \cdot 10^6$ kg/(m^{2}s) and by integrating the trace.

For the cross correlation trace A is always shifted relative to trace B. To estimate the time residual the maximum of the cross correlation function near the zero-time is picked. For the short wavelet of 2 s the P- and the PwP-phase are separated. The waveform of the P-phase is not disturbed by the PwP-phase. The maximum of the cross correlation is not shifted for each case. For the long wavelet of 10 s the situation is different. The length of the wavelet is larger than the two-way-time of the water multiples. Therefore P- and PwP-phase are not recorded as two onsets but as a conjoint phase. This conjoint wavelet differs from the original wavelet of the source. Therefore the maximum of the cross correlation is shifted. The shift can be removed by applying the wavefield decomposition (Fig. 4.28). The distortion of the wavelet is removed. The upgoing wavefield (A) shows the same waveform than the trace of the fictitious land station.

At periods shorter than the two-way travel-time of the first multiple (here 2.5 s) the apparent time shift is nearly zero (Fig. 4.29 upper panel). With increasing periods the time shift is decreasing or increasing up to 9 s at a period of 50 s. It is larger when

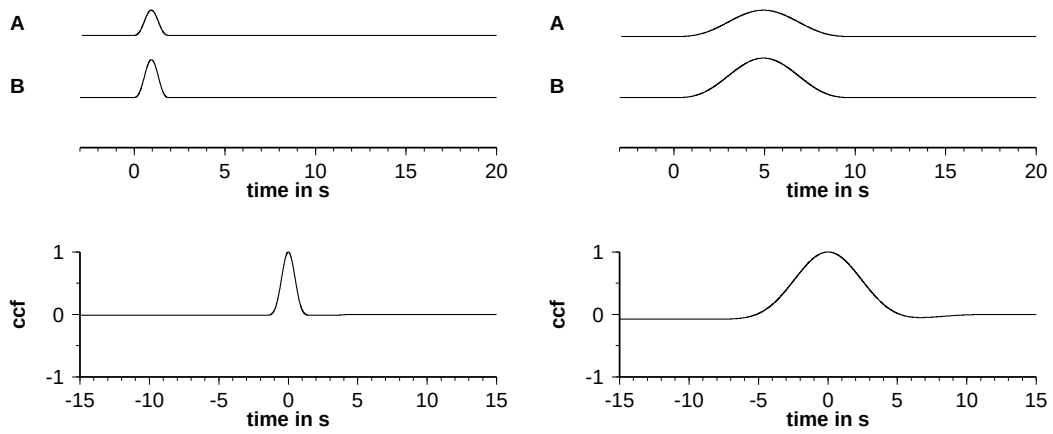

Figure 4.28: Determination of relative time residuals between the synthetic upgoing wavefield trace of a ocean bottom station (A) and of a land station (B). the traces are in pressure respectively in ground velocity. Thr normalized cross correlation function (ccf) is shown at the bottom. Two wavelet with a different period are used. **Right**: a source wavelet of a length of 2 s. **Left**: a source wavelet of a length of 10 s.

hydrophone traces are used. The maximal apparent time shift for the cross correlation between the seismometers is -0.88 s at a period of about 9.5 s and it descends to -0.70 s at higher periods.

After applying a wavefield decomposition and after using the upgoing wavefield to estimate travel time residuals the maximum of the cross correlation is zero, as expected, independent of the period and trace type (Fig. 4.29 bottom). Thus, the simplified example already indicates here that wavefield decomposition has the potential for improving the accuracy of inter-station travel time residuals from teleseismic phases.

Fig. 4.30 gives an example for two earthquakes in El Salvador and India respectively (see Table 4.2). The estimated travel time residuals between OB11 on the ocean bottom and the land station WDD in Malta differ significantly, depending on whether the hydrophone, the seismometer or the "upgoing-wave" seismograms are used. When traces from the vertical sensor are used the time residuals are, independently of the dominant period of the data, -0.8 s relative to the ones derived from the upgoing wavefield (triangles in Fig. 4.30). The theoretical bias as estimated from the ocean-layer over a half-space model is nearly independent of the period, constitutes a value of -0.7 s (Fig. 4.29) and corresponds well with the observations. When traces from the hydrophone channel are used the time shifts are larger and differ for both events. The El Salvador event has a dominant period of about 25s (P-phase). This leads to a time shift of about 5.5 s.

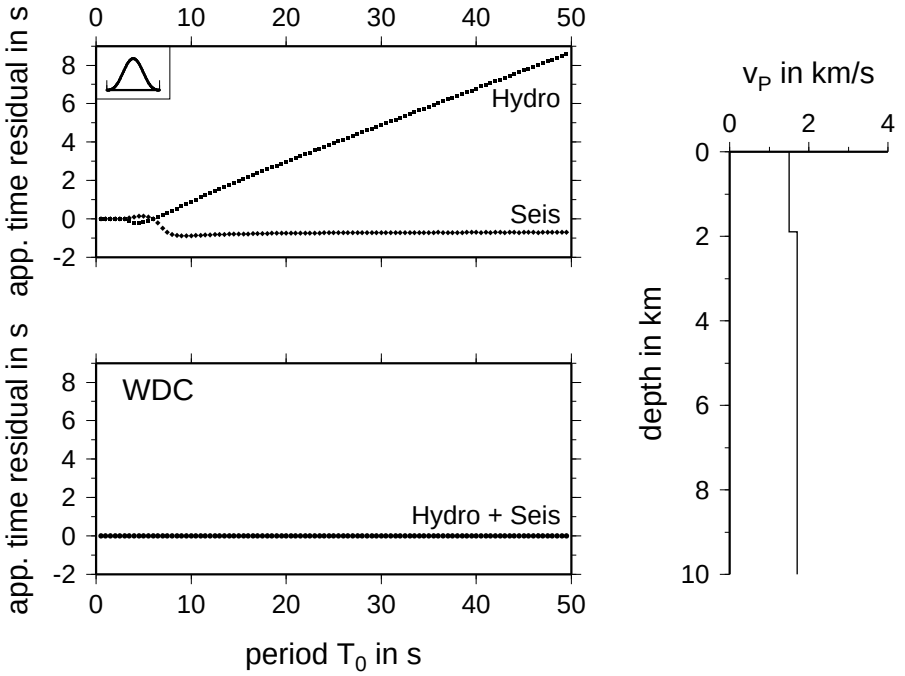

Figure 4.29: Apparent time residuals estimated from cross-correlation of synthetic waveforms for a fictitious land and a fictitious ocean bottom station. An ocean layer over half space has been used (right panel), and the travel-time effect from the different elevation of the two stations has been corrected. Plane waves arriving from below have been simulated with varying duration of the source time function (period). The top left panel shows the predicted apparent time residuals for the seismometer and hydrophone channel. The bottom left panel shows the prediction after applying a wavefield decomposition. The Brüstle-Müller-wavelet is plotted in the upper left corner.

The theoretical prediction of the bias was about 4 s at this period. The P-phase from the India earthquake arrived with a dominant period of about 20 s, which results in a time shift of 3 s, compared to the theoretical prediction of 3 s. Thus, both applications correspond well with the predicted, large bias in relative time delays. The wavefield decomposition is efficiently removing the systematic time shifts stemming from the water layer effect. These time shifts varied between -0.8 s and +5.5 s for the given examples. Thus, tomographic studies using land- and ocean bottom stations and neglecting the water layer effect may unnecessarily introduce systematic errors in their analysis.

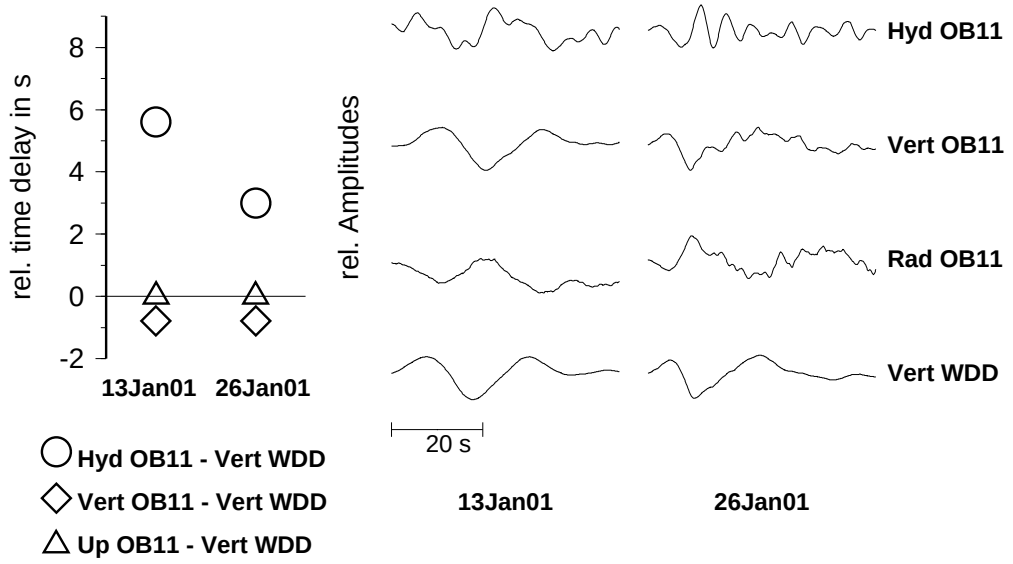

Figure 4.30:
Example of travel time residuals (left) from original (HYD, VER) and wavefield decomposed data (UP). The residuals were estimated between the ocean-bottom station OB11 and the land-station WDD in Malta by calculating a cross correlation. Different combinations of waveform data are indicated by different symbols as declared in the legend. Time residuals are relative and have been shifted to zero for the triangle symbols. P-phases from the 13 Jan. 2001, M=7.8, El Salvador and the 26 Jan. 2001, M=8.0, India, earthquakes have been analyzed. The displacement data for both earthquakes are plotted at the right. Data have been deconvolved to ground velocity for each trace and a 6-pole Butterworth bandpass filter with corners at 0.01 Hz and 4.5 Hz has been applied.

4.6 Discussion

It is demonstrated that the procedure for determining the calibration factor between the hydrophone and the seismometer and for the estimating the impedance contrast at the ocean floor is successful. The estimation of the calibration factor is done by minimizing the P-wave energy of the downgoing wavefield in the water. The impedance contrast is estimated by a minimizing of the squared zero-lag cross correlation between the downgoing wavefield in the water and the upgoing wavefield in the subsurface. Frequency independence of the calibration factors and impedance contrast can be assumed.

By using active seismic data Muijs et al. (2004) developed a technique to estimate frequency-dependent calibration functions and seafloor properties. Frequency-dependent parameters may be of advantage whenever the sensor transfer functions are unknown or grossly wrong. Another potential advantage may arise when the seafloor itself introduces a frequency-dependent transfer function. However, in this study much lower frequencies have been analyzed compared to Muijs et al. (2004). At least for our data a constant calibration factor and frequency-independent seafloor properties seem to be sufficient as we look at low frequent, narrow banded data. It must be realized that frequency-dependent transfer functions are most likely to be badly constrained and the problem might be ill-posed, at least when only few earthquake data are available.

The advantage of the squared zero-lag cross correlation is the independence on the time window chosen for calculation, in contrast to minimizing the energy of the multiple reflections. The squared zero-lag cross correlation is also less sensitive to sediment reflections compared to the non-squared zero-lag cross correlation. In addition to the potential biasing effect from sediment reflections heavy noise influences the result of the estimation of the calibration factor and of the impedance contrast. For instance a signal-noise-ratio of 7 (peak-amplitudes) changes the estimated impedance contrast about 10% .

The calibration factor is multiplied with the hydrophone, and the impedance contrast with the seismometer (see equation 4.6). Therefore, a trade-out exists between calibration factor and impedance contrast. A larger calibration factor results in a larger impedance contrast.

The wavefield decomposition depends weakly on the angle of the wavefield incidence. The coefficients in equation 4.7 are nearly constant for an angle of incidence between 0° and 60°. A small angle of incidence is expected in seismological studies due to the event-receiver-geometry. Shallow earthquakes occur in the upper crust. The P-velocity is about 5.8 km/s in the upper crust and about 1.7 km/s in the top sediment layer below the ocean bottom station. For horizontal wave propagation in the upper crust the P-wave arrives under the critical angle of incidence of 17° at the ocean bottom station.

Thus waves from deep earthquakes arrive the ocean bottom station under a smaller angle of incidence. Only deep local events are used for this thesis and therefore a vertical incidence can be assumed.

Hydrophone calibration factors of 0.36 and 0.25 are found for the stations OB10 and OB11. Impedance contrast at the ocean bottom are estimated for 13 deep local events. For OB10 the median of the impedance contrast is 1.3 and the one-sigma confidence interval ranges from 0.96 to 1.75. A small phase caused in the sediment occurs about 0.25 s after the arrival of the PwP phase. This fits with a result of another method fitting the waveforms, determining the thickness and the average P-velocity of a top subsurface gradient layer to 190 m and 1630 m/s respectively (see chapter 3). The two-way-travel time of a reflection is 0.233 s and pretty close to the estimate of 0.25 s here.

For OB11 the median of the impedance contrast is 1.5 and the confidence interval ranges from 0.67 to 3.25. A small phase occurs about 0.087 s after the arrival of the PwP phase. The thickness and the average P-velocity of a top subsurface gradient layer is independent determined to 95 m and 1691 m/s (see chapter 3). The two-way-travel time is 0.112 s. At both stations the results of both methods agree with each other. The impedance contrast is small at both stations. This mirrors the results of other studies declaring the top sediment layer unsolidified and water-saturated (Morgan (1969)) so that its seismic properties are similar to water.

The multiple reflections can disturb teleseismic applications like receiver functions and travel time residuals depending on the period of the waveform. For instance, the conversion of the mantle discontinuities are hidden by water multiples. Receiver functions from synthetic seismograms and real data show the occurrence of a periodical signal of water multiples. After applying the wavefield decomposition the periodical signal is attenuated, the receiver functions are improved and conversions of the mantle discontinuities are visible. We think that receiver functions of low frequency waveforms are less disturbed by multiple reflections than high-frequency waveforms. For a signal period of the P-phase four times larger than the main period of the multiples, i.e. eight times the two way travel time in the water, the effect of the multiple reflections decreases. Thus, the wavefield decomposition is more important for deep ocean recordings than for shallower ocean recordings.

The receiver function method was also applied to the local deep earthquake in the Tyrrhenian Sea to investigate Moho-depths. However, since our stations were close to the epicentre the wavefield incidence was nearly vertical. No energy converted at deep interfaces was visible on the receiver functions.

For the travel time residual estimation, in contrast, the effect of the multiple reflections increases with lower frequency. For the estimation with a seismometer the effect is less

than 1s over the whole frequency band. But with a hydrophone the residual increases linearly to 8 s at a Period of 50 s. This is a systematic effect and influences the results of teleseismic tomography. The depth of the ocean and the impedance contrast also influence the travel time residuals. By applying the wavefield decomposition, the effect of the multiple reflections is attenuated as we show with synthetic and real data. The correction of the travel time residuals for real data is similar to values estimated with synthetic seismograms.

The procedure for the estimation of the calibration factor and the impedance contrast fails to reproduce accurate parameter for teleseismic events. This is due to the lower frequency, i.e. the larger period of the teleseismic P-phase. If the main period of the P-phase is larger than the recurrence time of the multiples, the P- and PwP-phase are not separated but overlapping. Therefore, it is difficult to determine the time window for the minimization of P-wave energy and the squared cross correlation is not vanishing for the right impedance contrast. But as we show with the receiver function study it is not so much important for teleseismic applications to know the correct impedance contrast. There is still an improvement of the receiver functions if a wrong impedance contrast is used during the wavefield decomposition.

Chapter 5

Ringing-Phases

5.1 Observations

Horizontal mostly linear polarized, long enduring energy occurs with a dominant frequency and large amplitudes after P-onset. Therefore it is called a "Ringing phase". Fig. 5.1 shows the data of hydrophone and seismometer at station OB10 of the 07.12.2000 Ml=1.6 earthquake and the 04.01.2001, Ml=4.0 earthquake. All traces are restituted to ground motion and high pass filtered at a corner of 1.7 Hz. Also the pressure P of the hydrophone is restituted to ground motion by integration over time and dividing by the impedance of the water layer $I_1 = \rho_1\alpha_1 = 1.5 \cdot 10^6$ (see also equation 3.13). Horizontal traces are rotated into the great circle direction.

07.12.2000 Ml=1.6 earthquake was a small earthquake. Most other local events locks similar to this event. In contrast the 04.01.2001, Ml=4.0 earthquake was the stongest local event which occurred during the deployment. The ringing phase is more low frequent comparing to the 07.12.2000 Ml=1.6 earthquake. The amplitudes of the ringing phase are large compared to the amplitude of the P-wave. The Ringing phase is about 4 to 10 times larger than the P-wave as it can be seen in Fig 5.1 and 5.3. The delayed onset is obvious on the horizontal components and is for both about 0.65 s. It is also recognizable on the vertical component. There is no indication of the ringing phase on the hydrophone trace. It is remarkable that the P-wave is not recognizable on the horizontal components at all.

The particle motion of the first 2 s after the P-onset is shown in a projection into the horizontal plane in Fig. 5.2 and in a projection into the vertical-radial plane in Fig. 5.3. The linear and dominant horizontal polarization of the ringing phases is obviously. The P-phase is drawn in red in the particle motion plots of Fig. 5.3. The P-phase is vertical polarized as it is expected for a deep local earthquake.

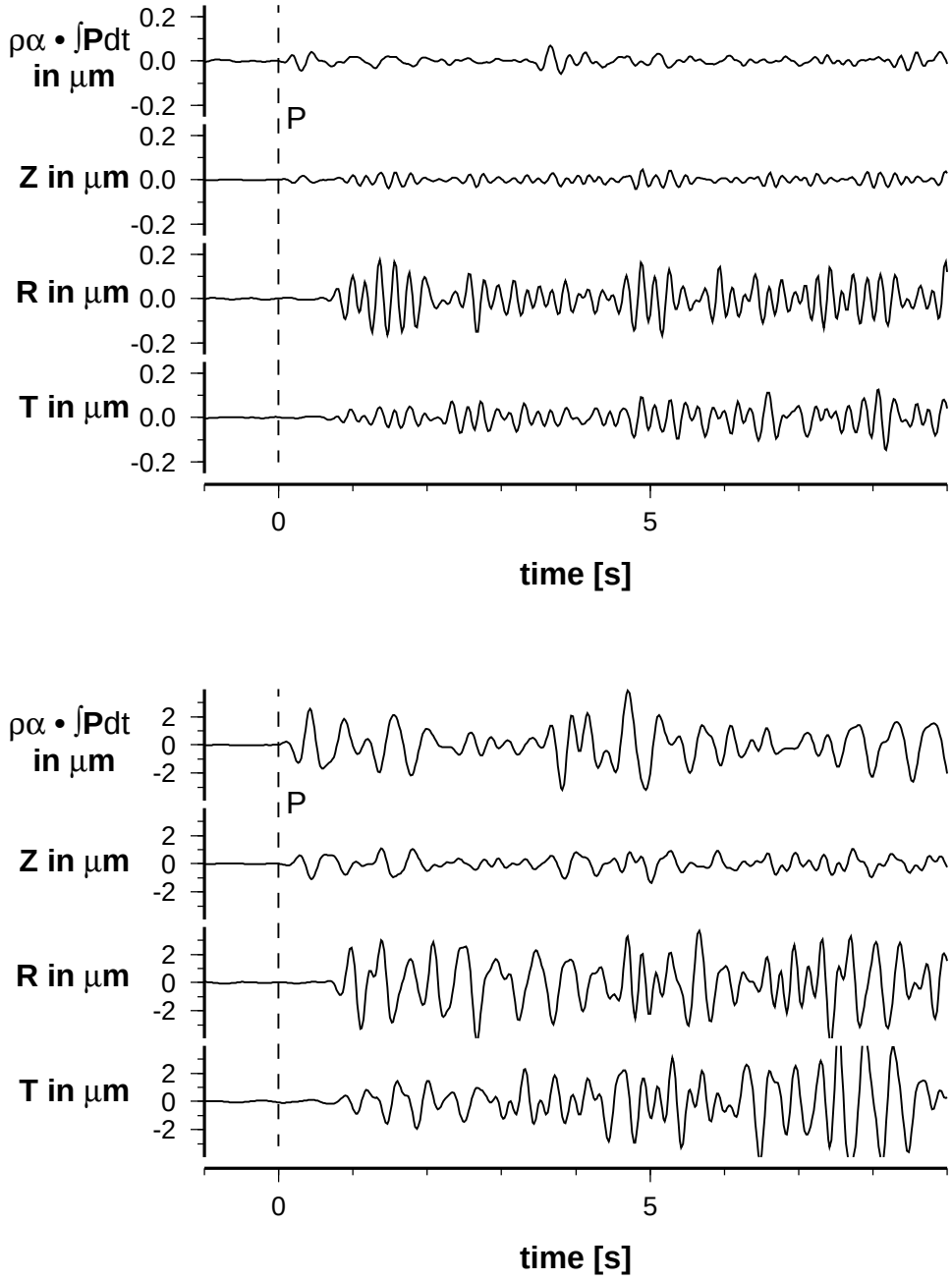

Figure 5.1: Ringing phases for station OB10. **Top**: 07.12.2000 Ml=1.6 earthquake. **Bottom**: 04.01.2001, Ml=4.0 earthquake.
Pressure data are integrated and divided with the impedance of the water layer $\alpha\rho = 1.5 \cdot 10^6$.

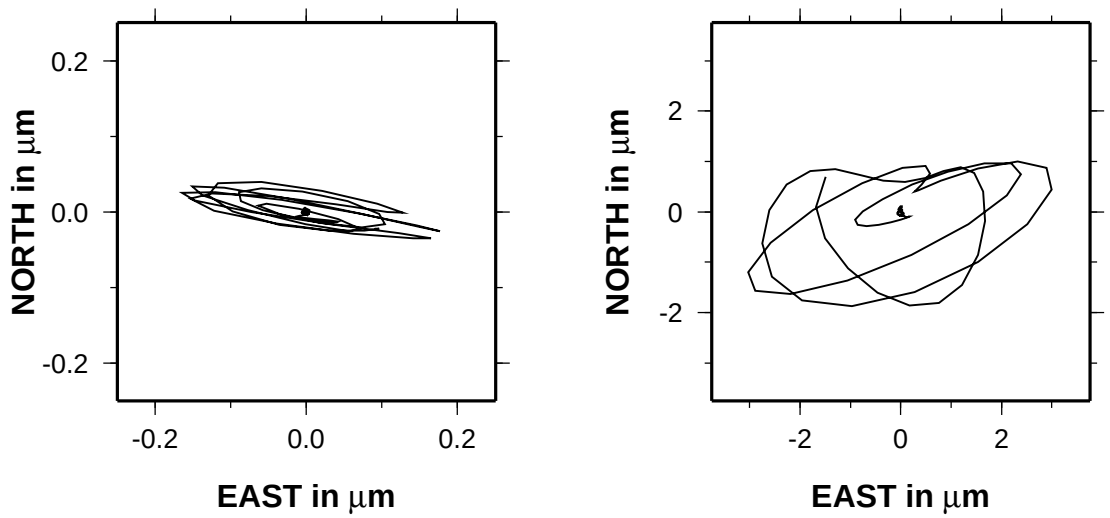

Figure 5.2: Particle motion plot of the horizontal components. Data is shown for the first 2s after the P-onset.

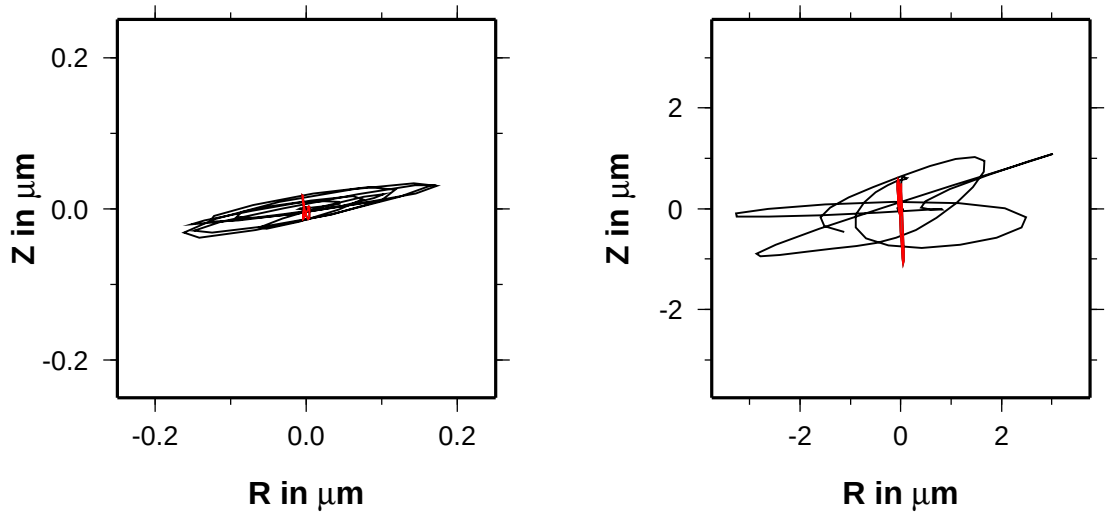

Figure 5.3: Particle motion plot in the vertical-radial plane. Data is shown for the first 2s after the P-onset. The P-phase is drawn in red.

Amplitude spectra are calculated and plotted in Fig. 5.4 for both earthquakes. The dominant frequency f_d of 5.5 Hz is clearly recognizable in the spectra for the 07.12.2000 Ml=1.6 earthquake. For the 04.01.2001, Ml=4.0 earthquake the peak at a frequency of 5.5 Hz is also present. But the largest peaks in the spectra are at a frequency of 1.5 Hz and 2.5 Hz. This corresponds to the observation of the waveforms. There are also other peaks at a frequency of about 8.5 Hz and 12 Hz. The frequency peaks are only recognizable on the seismometer, but not on the hydrophone.

A spectrogram of the vertical component (raw data) is calculated for the period of the deployment (Fig. 5.5). The frequencies peaks at the frequency of 5.5 Hz, 8.5 Hz and 12 Hz are present for the whole time. Minor peaks are also recognizable at frequencies of about 7 Hz, 9.5 Hz and 10.75 Hz.

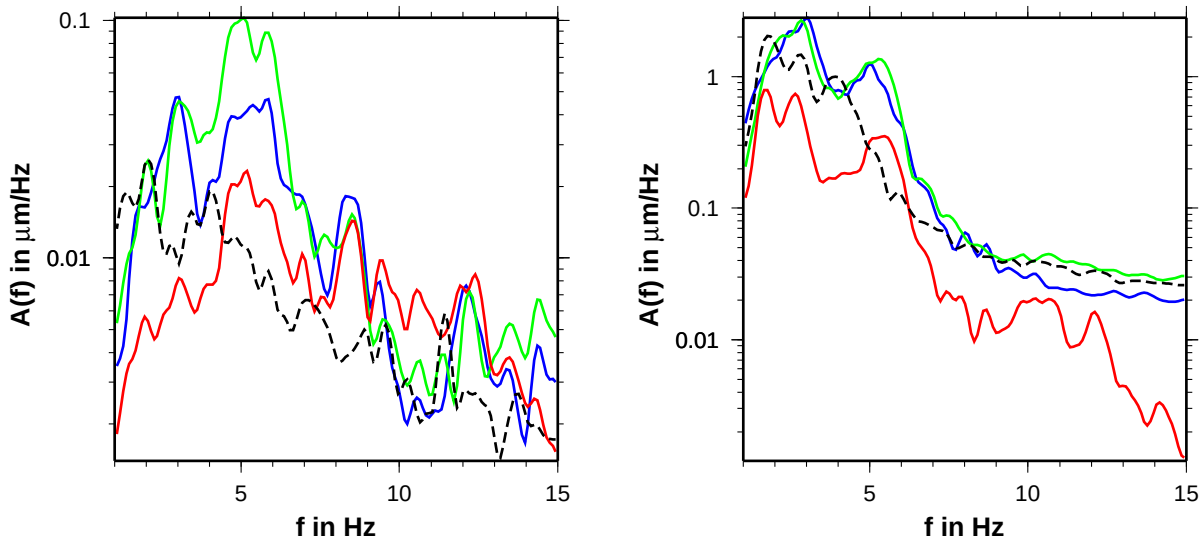

Figure 5.4: Smoothed power spectra for ground motion at station OB10 for **Left**: 07.12.2000 Ml=1.6 earthquake. **Right**: 04.01.2001, Ml=4.0 earthquake. Vertical component is plotted in solid red, horizontal in solid green and blue and hydrophone is in dashed black. Clear peak are visible at 5.5 Hz and at 8.5 Hz.

Time delay and dominant frequency is determined for each station. The results are shown in Fig. 5.6. Standard deviation of the estimated values are drawn as error bars. A correlation between time delay and frequency cannot be seen. Neither fit frequency and time delay together nor is there a systematic difference between the Hamburg type station and the station of GEOMAR.

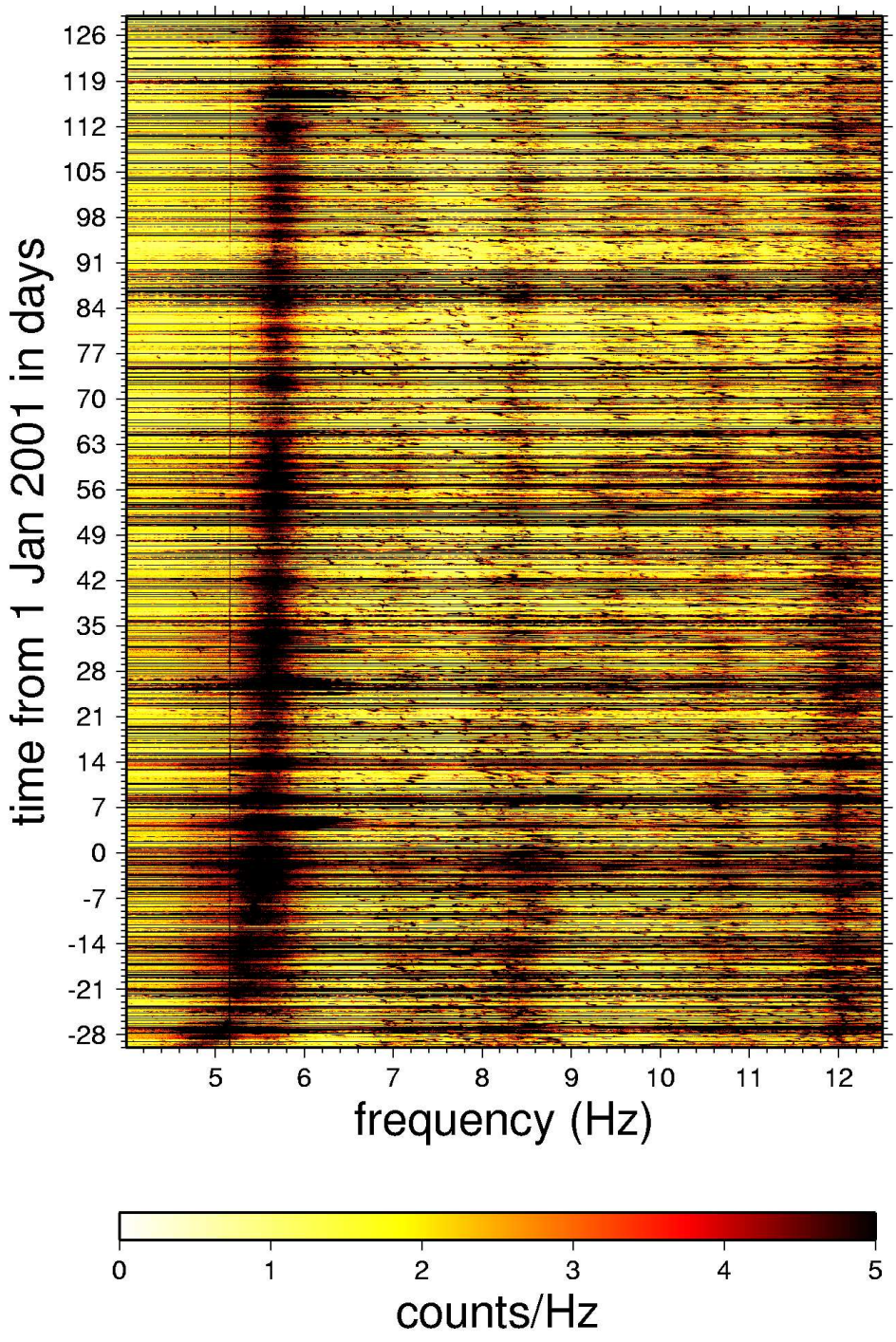

Figure 5.5: Spectrogram of the vertical component of OB10 for the period of the experiment.

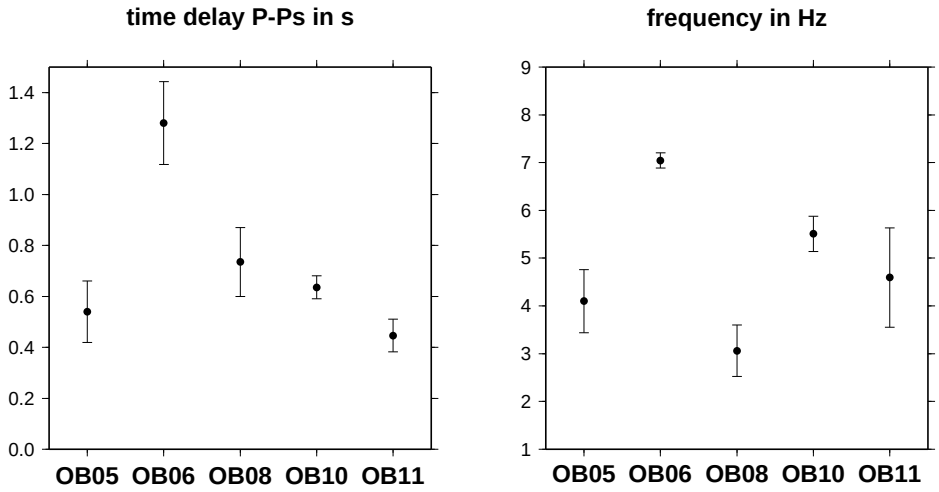

Figure 5.6: Overview of the observed time delay (left) and frequency (right) of the ringing phases. OB05 and OB06 are stations from GEOMAR, OB08, Ob10 and OB11 are from Hamburg.

5.2 Model

Lewis and McClain (1977) observed also ringing phases at ocean bottom during an active seismic experiment. They mentioned that the ringing phase is a shear wave converted from a P-wave at the lower interface of a unconsolidated (mud-)layer. Unconsolidated layers have low shear wave velocities below 100 m/s (Godin and Chapman, 1999).

The impedance contrast for shear waves is large at the lower interface between the mud layer and the basement and at the ocean bottom. Therefore, most shear wave energy is reflected back into the mud layer and shear wave energy is trapped in the unsolidified layer. Shear wave resonances are stimulated. Shear resonances are observed often. (e.g. Webb, 1998).

Since the shear velocity in the mud layer is small the S-wave is extremely steepen. Therefore the polarization is nearly horizontal. The transmission coefficient for the converted wave T_{PS} is proportional to the ratio of the P-velocity in the basement and the shear velocity in the mud layer. In the introduced model the velocity ratio is large and so large amplitudes are expected.

To assess the relative amplitudes between P and Ps transmission and reflection coefficients are calculated for a simple model. Transmission and reflection coefficient are taken from Aki and Richards (1980). Results are shown in Fig. 5.8. The S-wave which is generated by the conversion of the P-wave at the lower interface is extremely steepen and show no vertical displacement. P-wave is also steepen, but the P-wave has a significant displacement on both horizontal and vertical component. For an incidence angle larger

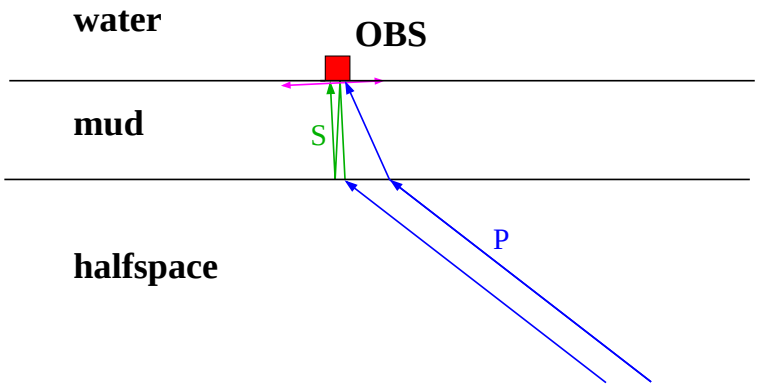

Figure 5.7: Sketch of the explanation of Lewis and McClain (1977). A incoming P-wave converts into a S-wave at the lower interface of the mud layer. The S-wave is steepen and trapped in the mud layer because of the low S-velocity.

than 40 degrees the amplitude of the Ps-wave is larger than the P-wave.

This model explains the polarization of the ringing phases, the time delay, the occurrence of bands of frequencies as harmonics and possible the large amplitudes. What is not explained is the discrepancy between the frequency and the time delay. One possibility is to assume that the resonance happens in a upper layer and the conversion from P to S in a lower interface.

5.3 Synthetic seismogram

To prove the extended model of Lewis and McClain (1977) synthetic seismograms are calculated for the 07.12.2000 Ml=1.6 earthquake for station OB10 using the program "qseis" from Wang (1999). The waveform of the P-phase is used as the source time function.

The background P-velocity model is the model found with the inversion of the PwP-phases. The sediment layer had average velocity of 1625 m/s and thickness of 190 m. The water layer is approximated by a "solid" media with a very low shear velocity of 0.01 m/s and a small Q-value for the intrinsic dumping $Q_s = 0.1$. The sediment layer is divided in three sublayer. The top should produce the resonance frequency and the two lower layer influence the amplitude pattern.

Several constrains was used for the models: a.) top layer should fit to the resonance frequency, i.e. thickness d should be $\lambda/4 = \beta/(4f_d)$, b.) average P-velocity is 1625 m/s and total thickness is 190 m and c.) time delay between Ringing phase and P is 0.65 s. P-velocity for the top layer is assumed to be 1500 m/s and of the second one 1550 m/s.

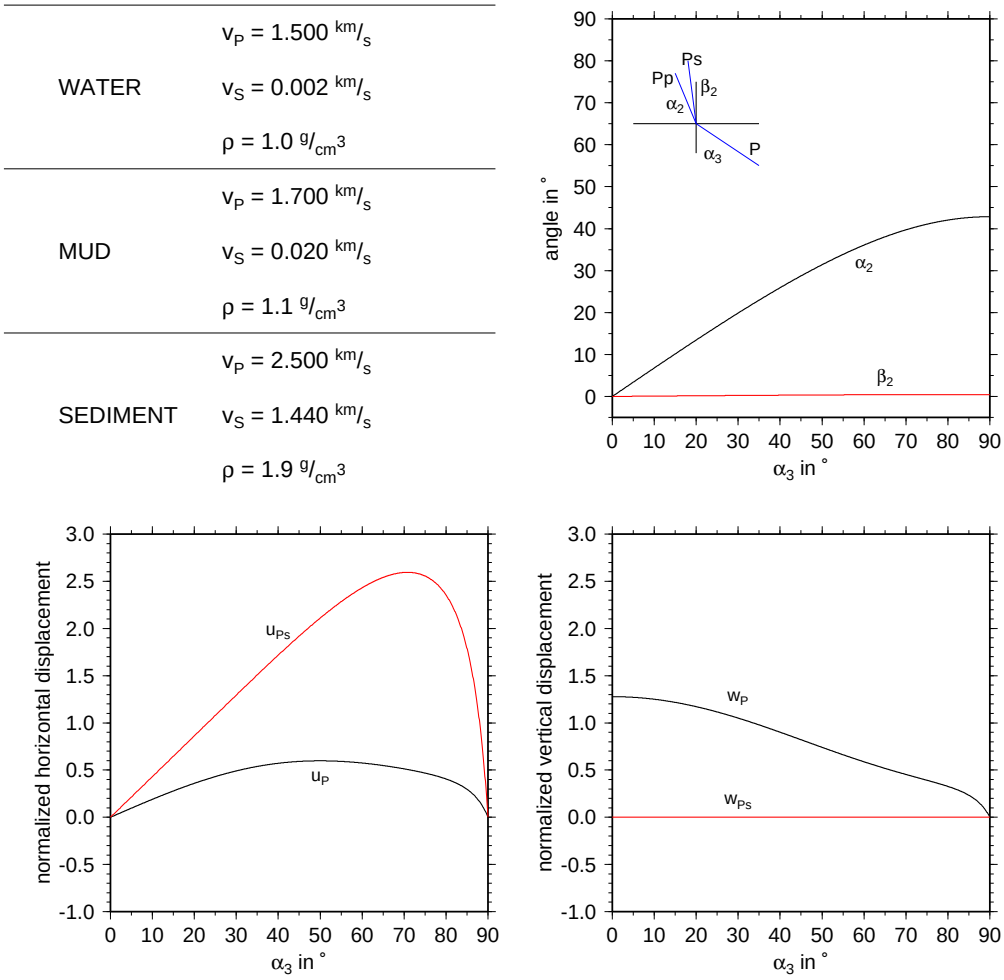

Figure 5.8: Vertical and horizontal amplitudes for a incoming P- and a converted Ps-wave calculated from transmission and reflection coefficients. **Top left**: model. **Top right**: incidence angle at the ocean bottom relative to the incidence angle of the incoming P-wave.
Bottom: horizontal (left) and vertical (right) displacement at the ocean bottom and relative to the incidence angle of the incoming P-wave. Displacement is normalized to the amplitude of the incoming P-wave. Results for the P-wave are plotted in black and for the Ps-wave in red.

Table 5.1:
Model A(top) and B(bottom) used to calculate synthetic seismogram showing ringing phases.

layer no.	thickness in m	P-velocity in m/s	S-velocity in m/s
1	2533	1500	0.1
2	2.27	1500	50
3	70	1550	170
4	119	1720	500
5		3200	1.847

layer no.	thickness in m	P-velocity in m/s	S-velocity in m/s
1	2533	1500	0.1
2	0.45	1500	10
3	70	1550	170
4	119	1720	500
5		3200	1.847

So only three parameter are free: top shear velocity, thickness and shear velocity of the middle layer. A systematic grid search is done. The top shear velocity is varied between 10 m/s and 70 m/s. The thickness of the middle layer varied from 10 m to 130 m and the shear velocity between 70 m/s and 250 m/s.

Fig. 5.9 show synthetic seismograms compared to the real data for two models. The two appendant model is listed in table 5.1. The model only differ in the velocity and the thickness of top layer.

5.4 Discussion

The 3-layer model is simple using only layers with constant velocity. Both models explain the time delay and frequency of the ringing phases. But the amplitudes of the synthetic ringing phase generated by the model A are to small. To fit the amplitudes the top shear velocity must be smaller than in model A. Amplitudes can be explained by the model B in the beginning of the ringing phase. The envelope of the synthetic ringing phase differs from the data for subsequent waveform of the ringing phase.

The thickness is about 0.45 m and the shear velocity is about 10 m/s in the top layer of the model B. Shear velocity and thickness are in the range of what is found before (Nolet

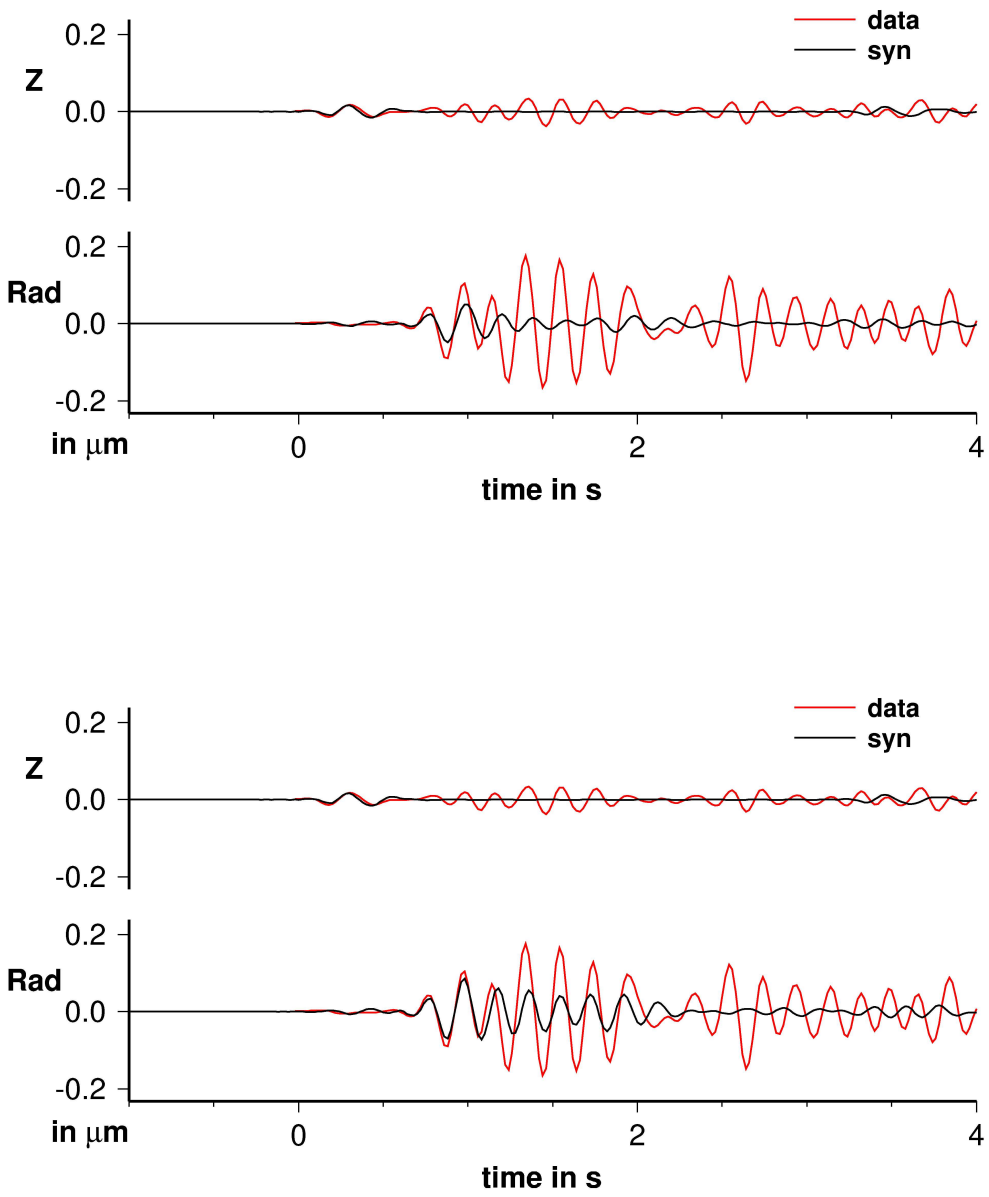

Figure 5.9:
Synthetic seismogram for vertical and radial component. **Top**: Model A. **Bottom**: Model B.

and Dorman, 1996). But usually a smooth increase of the shear velocity is observed over a range of about 30 m which can be assumed by an gradient layer. A gradient layer near the ocean bottom caused numerical instabilities of the program. Therefore it is not simulated.

The second layer has a shear velocity of 170 m/s and is about 70 m thick. It had a constant P-velocity. Conversions and multiple reflections from deeper interfaces may also contribute to the envelope of the ringing phases.

Osler and Chapman (1998) suggest an other explanation for the frequency of the ringing phases. They describe the poor coupling of the OBS station to the seafloor by a low-damped spring-dashpot model. The dominant frequency of the ringing phases is interpreted as the resonance frequency of the spring-dashpot model. The resonance frequency of the spring-dashpot model depends on the mass of the OBS station. As the Hamburg type OBS stations is about 5 to 10 times heaver than the external pack of the GEOMAR OBS. There should be a systematic differences in the observed dominant frequency what is not found. Osler and Chapman (1998) also mention a rocking of the OBS station producing a crosstalk from the horizontal components to the vertical component.

The interaction of our OBS station with the seafloor is unknown. Therefore the interaction is not considered for the simulation of ringing phases. Also the order of the crosstalk due to the rocking is unknown. Both effects are not negligible. It is important to determine the interaction by in situ experiments and to consider in the waveform analysis.

The interpretation of the ringing phases as Scholte waves can be excluded because the ringing phases are also observed on deep event recordings. In the case of deep earthquake no overcritical angles are present which are necessary for Scholte waves. Also no dispersion is observed.

Chapter 6

Summary

In this thesis waveform methods were developed and applied to two major tasks:

1. the improvement of data recorded by ocean bottom stations and
2. the estimation of sea floor properties and its structure.

The wavefield decomposition is a technique which can attenuate the multiple reflections in the water layer above an ocean bottom station. The calibration factor of the hydrophone and the impedance contrast at the sea floor has to be known for a successful application of the wavefield decomposition to the recorded data. Both, the calibration factor and the impedance contrast, can be estimated during the application as an in-situ result. Several criteria for the estimation of the impedance contrast were tested. It was found that the minimization of the squared zero-lag cross-correlation produces the best results for the estimation of the impedance contrast (chapter 4).

The application of the wavefield decomposition to the data of ocean bottom station is important as a preprocessing step to applying other seismological techniques to the data like receiver functions or travel time tomography. Without the application of the wavefield decomposition the results obtained by these techniques are strongly disturbed by the signal of the multiple reflections in the water layer. This is also due to the large impedance contrast at the ocean floor and the long duration of the multiple reflections. The wavefield decomposition attenuates the effect of multiple reflections in the water layer. It also improves the resolution and accuracy of receiver function studies and relative arrival time estimates. This was demonstrated with synthetic data as well as with real data. Unfortunately the number of records from teleseismic events was limited in the project. A crude demonstration of the attenuation of the multiple reflection and the elimination of them when applying the receiver function and travel times tomography was possible and demonstrated the big potential of the applied wavefield decomposition.

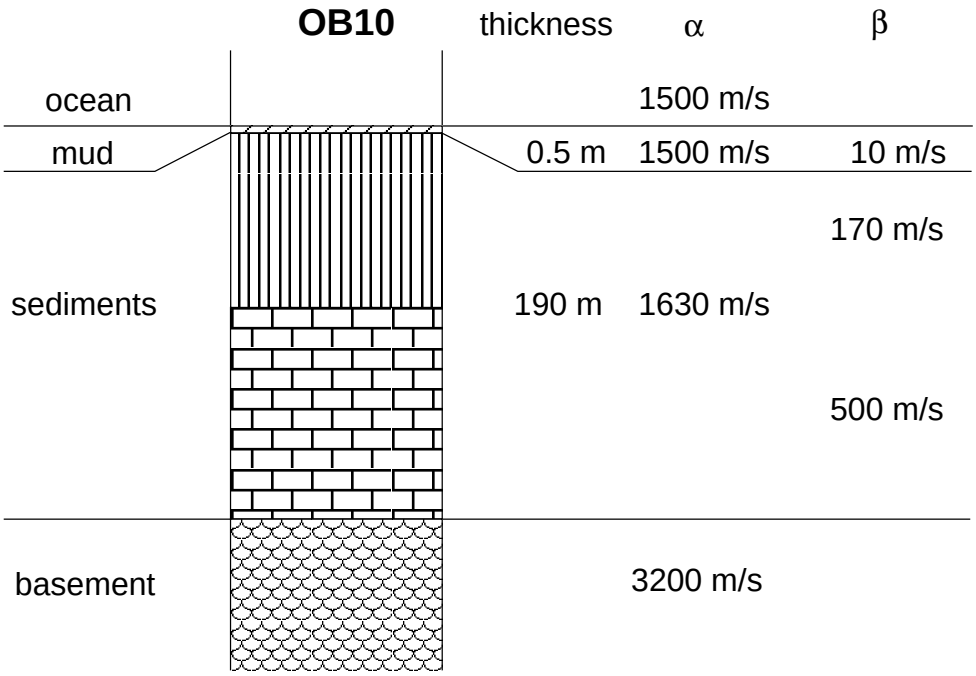

Figure 6.1: The underground model combines the results of the different means which were applied to the recordings of ocena bottom station OB10.

The impedance contrast at the sea floor is estimated from recording of local earthquakes during the application of the wavefield decomposition. After the attenuation of the multiple reflections in the water layer a sediment reflection is recognizable after the PwP-Phase. The two way travel time of the related sediment layer can be estimated. The waveform after the P- and the PwP-phase of local earthquakes differs due to the subbottom structure. Therefore, it is possible to obtain the P-velocity and the thickness of the uppermost layers of the subbottom by modeling the waveforms. Ringing phases which are clearly recognizable on recordings of local earthquakes are supposed to be shear wave resonances of a converted P- to S-wave in the upper most sediment layer. Characteristic for the ringing phases is their delay and their frequency. By modeling the waveform of the ringing phase it was possible to invert the S-wave velocity of the upper most sediment layer.

As a result of the application of the presented methods an integrated local model of the subbottom structure is obtained. Following properties were found for the ocean bottom station OB10 :

- a impedance contrast of 1.3,
- a two way travel time of 0.25 s,
- a thickness for the top sediment layer of 190 m,

- a average P-velocity of 1630 m/s and
- a S-velocity of 10 m/s on top and 170 m/s and 500 m/s in the lower part.

The model of the subbottom which combines all results is shown in Fig. 6.1. The thin uppermost layer has a P- and S-velocity similar to water. It must be water-saturated and can be assumed to be mud. This result is similar to other studies (e.g. Nolet and Dorman, 1996). Another sediment layer lies below the top mud layer. This layer is 190 m thick. It may consist of two layers since the P-velocity has an unusual power law and the modeling of the ringing phases needs a two layered model for the S-velocity. The structure of the underground below is weakly constrained by the investigation of the experimental data. The estimated P-velocity is 3200 m/s.

The resolution of the model is not as high as usually obtained in high frequency active seismic experiments. But the knowledge of the properties of the uppermost layer gives the possibility to consider side effects for passive seismic recordings. Even the spatial distribution of the thickness, the P- and the S-velocity is of interest.

Another result is the estimation of the sensor orientation by the use of the ringing phases. The orientation of a free fall ocean bottom station cannot be controlled. A common approach is to determine the orientation after the experiment by comparing real and apparent backazimuth of earthquake phases. Since ringing phases are supposed to be a converted P- to S-wave their polarization points in the direction of the great circle between the earthquake and the station. So the angle to the apparent north-component of polarization is the apparent backazimuth. The analysis with the ringing phases of local earthquakes shows similar results to an analysis which used teleseismic events. The advantages of the use of ringing phases of local earthquakes are the higher frequency of the waveform, the strong amplitudes of the ringing phases and the large number of local earthquakes. A difficulty of the method is that you have to consider effects which are caused by the 3-dimensional media in the investigation area.

The presented und discussed methods give the possibility to use ocean bottom stations and land station in a combined network. Investigation of the structure of the earth can be extended into the ocean areas. The depth resolution of a tomography study correlates with the spatial distribution of the stations at the surface. Several areas like Iceland only allow a limited depth resolution of the tomography based on recording by land stations because of the distribution of land. A combined network of land and ocean bottom station can provide a far more accurate resolution into the depth through a bigger spatial range of the installed network.

Acknowledgement

First of all I want to thank my supervisor Prof. Torsten Dahm. I have worked with him since I started my diploma thesis at the University of Frankfurt. Torsten gave me the opportunity to join the work for the project "Tyrrhenian Sea" and to broaden my academic horizon in terms of marine geophysics and seismology.

Especially I want to thank the Deutsche Forschung Gemeinschaft (DFG) for financing the project "Tyrrhenian Sea" and my job position.

Many thanks to the leader of the "Tyrrhenian Sea" project Prof. Ernst Flüh from GEOMAR and his team for his support and providing many intruments.

I express my gratitude to the Istituto Nazionale di Geofiscia e Vulcanologia (INGV) of Italy for the cooperation in the project. Especially I want to mention Thomas Braun as my main contact person.

I want to thank Wang for providing his program "qseis" and implementing several new features which I needed.

Christian Hübscher was head of a research cruise in the eastern Mediterranean sea and I was allowed to take part in it. It was a interesting experience. I do not want to miss it. Thanks!

My colleagues at the department of Geophysics of the University of Hamburg were always a big support for me during my work on this thesis. I want to thank them all and will miss the time in Hamburg with them.

List of Figures

List of Tables

Bibliography

Abers, G. A., Hu, X., and Sykes, L. R., 1995. Source scaling of earthquakes in the Shumagin region, Alsaka:time-domain inversions of regional waveforms. Geophys. J. Int., 123:41–58.

Aki, K. and Richards, P., 1980. Quantitative Seismology: Theory and Methods. W. H. Freeman and Co., San Francisco, pp. 1–923.

Allen, R. M., Nolet, G., Morgan, W. J., Vogfjörd, K., Bergsson, B. H., Erlendsson, P., Foulger, G. R., Jakobsdóttir, S., Julian, B. R., Pritchard, M., Ragnarsson, S., and Stefánsson, R., 2002. Imaging the mantle beneath Iceland using integrated seismological techniques. J. Geophys. Res., 107(B12):3–1.

Ammon, C. J., 1992. A comparison of deconvolution techniques. Connaissance des Temps.

Ammon, C. J., Randall, G. E., and Zandt, 1990. On the nonuniqueness of receiver function inversions. J. Geophys. Res., 95(B10):15303–15318.

Amundsen, L. and Reitan, A., 1995. Decomposition of multicomponent sea-floor data into upgoing and downgoing p- and s-waves. Geophysics, 60:563–572.

Barr, F. and Sanders, J., 1989. Attenuation of water-column reverberations using pressure abnd velocity detectors in a water-bottom cable. SEG Expanded Abstracts, pp. 1–4.

Braunmiller, J., Dahm, T., and Bonjer, K., 1994. Source mechanism of the 1992 Roermond earthquake from surface wave inversion of regional data. Geophys. J. Int., 116:663–672.

Brüstle, W., 1985. Der Bruchvorgang im Erdbebenherd — Untersuchung ausgewählter Erdbeben mit beobachteten und synthetischen Seismogrammen. PhD thesis, Institut für Meteorologie und Geophysik, Universität Frankfurt, pp. 1–304.

Brüstle, W. and Müller, G., 1983. Moment and duration of shallow earthquakes from love-wave modelling for regional distances. Phys. Earth and Planet. Inter., 32:312–324.

Burdick, L. J. and Langston, A., 1977. Modeling Crustal Structure Through the Use of Converted Phases in Teleseismic Body-Wave Forms. Bull. Seism. Soc. Am., 67(3):677–691.

Caldwell, J., 1999. Marine multicomponent seismology. The Leading Edge, Nov:1275–1282.

Clayton, R. W. and Wiggins, R. A., 1976. Source shape estimation and deconvolution of teleseismic body waves. Geophys. J. R. Astron. Soc., 47:151–177.

Crawford, W. and Webb, S., 2000. Identifying and removing tilt noise from low-frequency ($< 0.1\,hz$) seafloor vertical seismic data. Bull. Seism. Soc. Am., 90:952–963.

Dahm, T., Thorwart, M., Flueh, E., Braun, T., Herber, R., Favali, P., Beranzoli, L., D'Anna, G., Frugoni, F., and Smirglio, G., 2002. Ocean bottom seismological instruments deployed in the Tyrrhenian Sea. EOS Transaction, 83:309, 314.

Dahm, T., Tilmann, F., and Phipps-Morgan, J., 2004. Seismic broadband ocean bottom data and noise observed with free-fall stations: experiences from long-term deployments in the North Atlantic and Tyrrhenian Sea. submitted.

Gennesseaux, M., Burollet, P., and Winnock, E., 1998. Thickness of the plio-quaternary sediments (ibcm-pq). BOLLETINO DI GEOFISICA TEORICA ED APPLICATA, pp. 243–284.

Godin, O. and Chapman, D., 1999. Shear-speed gradients and ocean seismo-acoustic noise resonances. J. Acoust. Soc. Am., 106:2367–2382.

Goes, S., Giardini, D., Jenny, S., Hollenstein, C. Kahle, H.-G., and Geiger, A., 2004. a recent tectonic reorganization in the south-central Mediterranean. Earth and Planetary Science Letters, 226:335–345.

Greenhalgh, S. A., Mason, I. M., Mosher, C. C., and Lucas, E., 1990. Seismic wave-field separation by multicomponent tau-p polarisation filtering. Tectonophysics, 173:53–61.

Gurrola, H., Baker, G. E., and Minister, J. B., 1995. Simultanios time-domain deconvolution with application to the computation of receiver function. Geophys. J. Int., 120:537–543.

Kennett, B. and Engdahl, E. B. R., 1995. Constraints on seismic velocities in the earth from travel times. Geophys. J. Int., 122:108–124.

Laughton, A., 1954. Laboratory measurements of seismic velocities in ocean sediments. Proc.Roy.Soc, 222:336–341.

Lay, T. and Wallace, T., 1995. Modern global seismology. Academic Press, INC.

Lewis, B. and McClain, J., 1977. Converted shear waves as seen by ocean bottom seismometers and surface buoys. Bull. Seism. Soc. Am., 67:1291–1302.

Li, X., Bock, G., Vafidis, A., Kind, R., Harjes, H.-P., Hanka, W., Wylegalla, K., van der Meijde, M., and Yuan, X., 2003. Receiver function study of the Hellenic subduction zone: imaging crustal thickness variations and the oceanic Moho of the descending African lithosphere. Geophys. J. Int., 155:733–748.

Montabetti, J. and Kanasewich, E., 1970. Enhancement of teleseismic body wave phases with a polarisation analysis. Geophys. J. R. Astron. Soc., 21:119–129.

Morgan, N., 1969. Physical properties of marine sediments as related to seismic velocities. Geophysics, 34:529–543.

Muijs, R., Robertsson, J., and Holliger, 2004. Data-driven adaptive decomposition of multicomponent seabed recordings. in press.

Müller, G., 1969. Theoretical seismograms for some types of point-sources in layered media. Zeitschrift für Geophysik, 35:347–371.

Nafe, J. and Drake, C., 1963. Physical properties of marine sediments. In Hill, M., editor, *The Sea*, Volume 3. interscience, new York.

Neri, G., Caccamo, D., Cocina, O., and Montalto, A., 1996. Geodynamic implications of earthquake data in the south tyrrhenian sea. Tectonophysics, 258:233–249.

Nolet, G. and Dorman, L., 1996. Waveform analysis of Scholte modes in oceanic sediment layers. Geophys. J. Int., 125:385–396.

Osen, A., Amundsen, L., and Reitan, A., 1999. Removal of water-layer multiples from multicomponent sea-bottom data. Geophysics, 64:838–851.

Osler, J. and Chapman, D., 1998. Quantifying the interaction of an ocean bottom seismometer with the seabed. J. Geophys. Res., 103:9879–9894.

Polster, A., 2004. Dispersionsanalyse von Oberflächenwellen im tyrrhenischen Meer mittels der Zwei-Stationen-Methode. Master's thesis, Institut für Geophysik, Universität Hamburg.

Ritter, J. R. R., Jordan, M., Christensen, U. R., and Achauer, U., 2001. A mantle plume below the Eifel volcanic fields, Germany. Earth and Planetary Science Letters, 186:7–14.

Schalkwijk, K., Wapenaar, K., and Verschuur, E., 1998. Decomposition of multicomponent ocean-bottom data in two steps. SEG Expanded Abstracts, pp. 1–4.

Schneider, W. and Backus, M., 1964. Ocean bottom seismic measurements off the California coast. J. Geophys. Res., 4:1135–1143.

Shen, Y., Wolfe, C. J., and Solomon, S. C., 2003. Seismological evidence for a mid-mantle discontinuity beneath Hawaii and Iceland. Earth and Planetary Science Letters, 214:143–151.

Thorwart, M. and Dahm, T., 2005. Wave field decomposition for passive ocean bottom seismological data. Geophys. J. Int., 163:611–621

Vergne, J., Wittlinger, G., Farra, V., and Su, H., 2003. Evidence for upper crustal anisotropy in the Songpan-Ganze (northeastern Tibet) terrane. Geophys. Res. Lett., 30:6–1.

Vinnik, L. P., 1977. Detection of waves converted from P to S in the mantle. Phys. Earth and Planet. Inter., 15:39–45.

Wang, R., 1999. A simple orthonormalizing method for stable and efficient computations of Green functions. Bull. Seism. Soc. Am., 89:733–741.

Wapenaar, C., Herrmann, P., Verschuur, D., and Berkhout, A., 1990. Decomposition of multicomponent seismic data into primary p- and s-wave responses. Geophys. Prosp., 38:633–661.

Webb, S., 1998. Broadband seismology and noise under the ocean. Rev. Geophys., 36:105–142.

Wittwer, A., 2004. Erdbebenlokalisierung im tyrrhenischen Meer mit kombinierten Ozeanboden- und Landdaten. Master's thesis, Institut für Geophysik, Universität Hamburg.

Yan, Y., 2002. Suppression of water-column multiples by combining components of ocean-bottom seismic surveys. Master's thesis, Department of Geology and Geophysics, Calgary.

Appendix A

Reflectivity method

Boundary condition at the interface between two layers relate the complex amplitudes $A_l^{\pm}$ and $A_{l+1}^{\pm}$ of the layers l and $l+1$ with $1 \leq l < n$ (see Fig. 3.3, equation 3.17).

There are two boundary conditions:

1. continuity of displacement:

$$u_l(z_l, t) = u_{l+1}(z_l, t) \tag{A.1}$$

2. continuity of normal stress (using $\alpha = \sqrt{\frac{\lambda+2\mu}{\rho}}$):

$$\begin{aligned} (\lambda + 2\mu)\frac{\partial u_l(z_l,t)}{\partial z} &= (\lambda + 2\mu)\frac{\partial u_{l+1}(z_{l+1},t)}{\partial z} \\ \Leftrightarrow \qquad \rho_l \alpha_l^2 \frac{\partial u_l(z_l,t)}{\partial z} &= \rho_{l+1}\alpha_{l+1}^2 \frac{\partial u_{l+1}(z_{l+1},t)}{\partial z} \end{aligned} \tag{A.2}$$

Inserting equation 3.17 in the boundary conditions yields a equation system for the amplitudes A below and beneath the interface for every frequency:

$$\begin{aligned} A_l^+ \, exp\left[-i\omega\tfrac{d_l}{\alpha_l}\right] + A_l^- \, exp\left[+i\omega\tfrac{d_l}{\alpha_l}\right] &= A_{l+1}^+ + A_{l+1}^- \\ \rho_l\alpha_l\left(-A_l^+ \, exp\left[-i\omega\tfrac{d_l}{\alpha_l}\right] + A_l^- \, exp\left[+i\omega\tfrac{d_l}{\alpha_l}\right]\right) &= \rho_{l+1}\alpha_{l+1}\left(-A_{l+1}^+ + A_{l+1}^-\right) \end{aligned} \tag{A.3}$$

The reference depth is the top boundary of the layer l (see above). Phase terms $exp\left[\pm i\omega\frac{d_l}{\alpha_l}\right]$ consider the time shift caused by the propagation of the waves through the layer l.

The solution of the equation system for A_l^+ and A_l^- is:

$$\begin{aligned} A_l^+ &= \frac{1}{2}\, exp\left[i\omega\tfrac{d_l}{\alpha_l}\right]\left\{\left(1 - \tfrac{I_{l+1}}{I_l}\right)A_{l+1}^+ + \left(1 + \tfrac{I_{l+1}}{I_l}\right)A_{l+1}^-\right\} \\ A_l^- &= \frac{1}{2}\, exp\left[-i\omega\tfrac{d_l}{\alpha_l}\right]\left\{\left(1 + \tfrac{I_{l+1}}{I_l}\right)A_{l+1}^+ + \left(1 - \tfrac{I_{l+1}}{I_l}\right)A_{l+1}^-\right\} \end{aligned}$$

I_l is the impedance of the layer $\rho_l \alpha_l$.

The same equation in the matrix notation is:

$$\begin{pmatrix} A_l^+ \\ A_l^- \end{pmatrix} = \begin{pmatrix} \frac{1}{2}\, exp\left[i\omega\frac{d_l}{\alpha_l}\right]\left(1+\frac{I_{l+1}}{I_l}\right) & \frac{1}{2}\, exp\left[i\omega\frac{d_l}{\alpha_l}\right]\left(1-\frac{I_{l+1}}{I_l}\right) \\ \frac{1}{2}\, exp\left[-i\omega\frac{d_l}{\alpha_l}\right]\left(1-\frac{I_{l+1}}{I_l}\right) & \frac{1}{2}\, exp\left[-i\omega\frac{d_l}{\alpha_l}\right]\left(1+\frac{I_{l+1}}{I_l}\right) \end{pmatrix} \begin{pmatrix} A_{l+1}^+ \\ A_{l+1}^- \end{pmatrix} \quad (A.4)$$

$$= \begin{pmatrix} m_{11} & m_{12} \\ m_{21} & m_{22} \end{pmatrix} \begin{pmatrix} A_{l+1}^+ \\ A_{l+1}^- \end{pmatrix}$$

Equation A.4 describes the relationship between the amplitudes in the layer above and below the boundary. The matrix:

$$m_l = \begin{pmatrix} m_{11} & m_{12} \\ m_{21} & m_{22} \end{pmatrix}$$

is called the layer matrix.
By multiplying the single layer matrices the Amplitude of the top layer A_1^+ and A_1^- are related to the Amplitudes of the lower half space A_n^+ and A_n^-:

$$\begin{pmatrix} A_1^+ \\ A_1^- \end{pmatrix} = \mathbf{m_1} \cdot \mathbf{m_2} \cdot \ldots \cdot \mathbf{m_{l-2}} \cdot \mathbf{m_{l-1}} \begin{pmatrix} A_n^+ \\ A_n^- \end{pmatrix} = \begin{pmatrix} M_{11} & M_{12} \\ M_{21} & M_{22} \end{pmatrix} \begin{pmatrix} A_n^+ \\ A_n^- \end{pmatrix} \quad (A.5)$$

Appendix B

Calibration of PMD

B.1 PMD seismometer

B.1.1 Setting and method

A STS-2/Quanterra-System, three spheres with the PMD-sensors built in a OBS frame and an other PMD-Sensor were placed for two weeks at the old observatory of Hamburg to check the transfer function of the seismographs (PMD sensor & GEOLON data logger). The combination of sensor and data logger were changed to resolve the effects caused by the sensor or data logger.

The comparison showed that all data logger are equal and the differences of the recordings belongs to the PMD sensors.

We assume that the poles and zeros given in the PMD handbook are correct but the generator constant G of 1000 Vs/m is wrong. We also assumed that the two horizontal components have the same generator constant.

The maximum input voltage of the GEOLON Data logger was $1.92V$ ($= 10 \cdot 10^3\Omega \cdot 192 \cdot 10^{-6}A$). This range is divided by $2^{17} counts$. The discretization factor of the data logger is $68266.667 counts/V$.

The STS-2/Quanterra system has a overall sensitivity of $0.6 counts\, s/nm$ and is flat in the frequency range under study.

Both STS-2 and PMD are velocity proportional between 0.02 Hz and 10 Hz. Therefore it is possible to use teleseismic surface waveforms with frequency below 0.1 Hz to determine a relative sensitivity. Teleseismic surface waveforms have general large amplitude and are only less disturbed by noise.

Four teleseismic earthquakes were recognizable (Tab. reftab1). The data of the event on 31.10.2001 couldn't be used because of a storage problem of the Quanterra.

Table B.1: events used for calibration:

date	time	magnitude	region
19.10.2001	03:29	7.4	Banda Sea
21.10.2001	00:29	6.6	North Island of New Zealand
26.10.2001	23:06	6.0	Vanatu Island
31.10.2001	09:10	6.9	New Britain Region

To calibrate the vertical component of the PMD power spectra were plotted relative to the STS-2 in the frequency band of the seismic energy between 0.04 Hz and 0.1 Hz seismic energy occurred. A linear relationship is supposed between both functions. By calculating a linear regression we get the constant of the PMD-seismometers relative to the STS-2. By multiplying it with the absolute sensitivity constant of the STS-2/Quanterra system the absolute sensitivity for the PMD-GEOLON system is determined.
To calibrate the horizontal component we plotted the horizontal amplitude of each sample of the surface waves relative to the STS-2 and calculated also a linear regression to get a relative constant.

B.1.2 Results of the linear regression

vertical component:

sensor	mean constant rel. to STS-2	mean constant in counts s/nm	mean constant in Vs/m
PMD 4129019 sphere 1, OB11	0.166470958	0.099882575	1463.1237
PMD 4129020 sphere 3, OB08	0.202613443	0.121568065	1780.7822
PMD 4129021 sphere 4, OB10	0.13603636	0.079562182	1165.4617
PMD 521	0.204629821	0.122777893	1798.5043
PMD 518	0.260123849	0.156074309	2286.2451

horizontal components:

sensor	mean constant rel. to STS-2	mean constant in counts s/nm	mean constant in Vs/m
PMD 4129019 sphere 1, OB11	0.171531945	0.102919167	1507.6050
PMD 4129020, sphere 3, OB08	0.211183667	0.1267102	1857.9745
PMD 4129021, sphere 4, Ob10	0.18181399	0.109088394	1597.9745
PMD 521	0.256284967	0.15377098	2252.5046
PMD 518	0.226629674	0.135977844	1991.8629

B.1.3 Discussion

Amplitudes of the vertical component of PMD and STS-2 show a clear linear relationship (Fig. B.1), i.e. the PMD is in the frequency band of 0.04 to 0.1 HZ velocity proportional. This is also visible in Fig. B.2 showing traces of the events for the STS-2/Quanterra system and the corrected PMD-sensors.

a.)

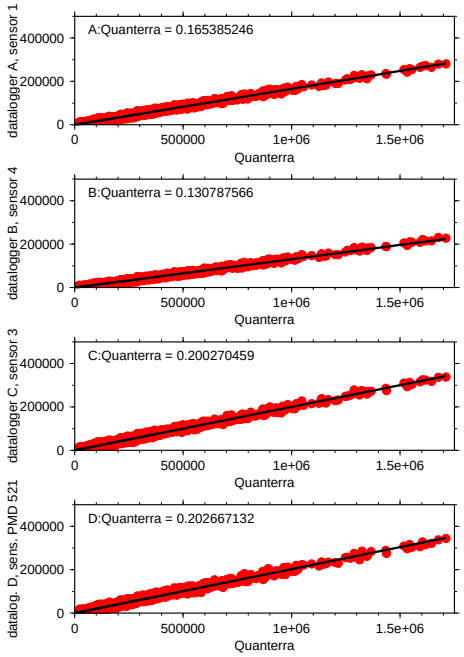

b.)

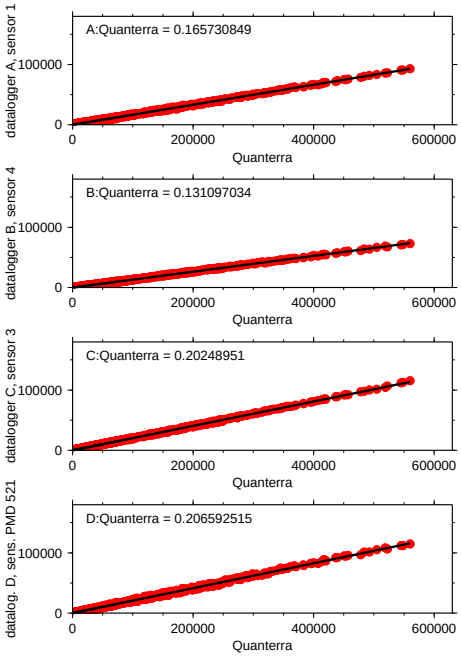

c.)

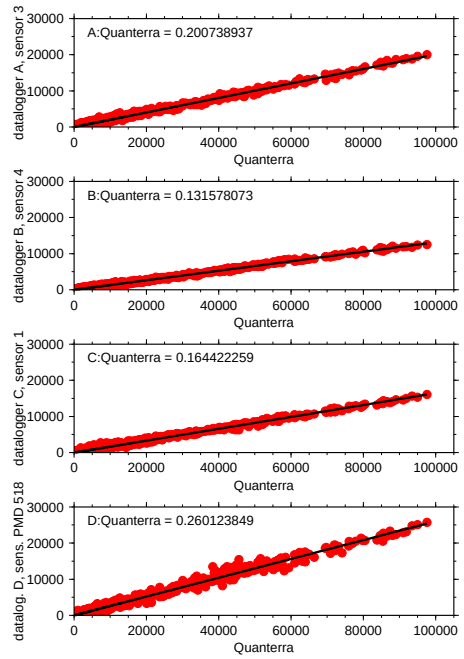

Figure B.1:
Amplitude spectra of the vertical component of PMD seismometers are plotted against the Amplitudes of the the vertical component of the STS-2 seismometer for the 3 events.
Relative sensitivity of the PMD seismometer are written in the upper left corner.

The linear relationship is not so clear on the horizontal components. If the horizontal components have different transfer functions, the estimated relative sensitivity should vary depending to the back-azimuth. But there is no large variation recognizable. Therefore the assumption of equal horizontal components is not disproved.

B.2 OAS-hydrophone

OAS-hydrophone are pressure and therefore velocity proportional. The OAS got a sensitivity of $2.5 \cdot 10^{-4} V/Pa$ and a capacitance of $50 \cdot 10^{-9} F$. There was a resistance of $10^6 \Omega$ parallel to the hydrophone. The hydrophone and the resistance are a high-pass filter with an corner frequency of $3.1831 Hz$, i.e. a zero at $0 Hz$ and a pole at $20 Hz$ in the ω-domain. To fit the dynamic range of the hydrophone/GEOLON system a preamplifier with a factor of 20 ($26 dB$) was used. The hydrophone input channel was adjusted to a peak-amplitude of $1.25 V$, i.e. a discretization factor of $1.048576 \cdot 10^5$.

The over all factor for the hydrophone GEOLON system is the product of the three factors: $1.048576 \cdot 10^5 \cdot 20 \cdot 2.5 \cdot 10^{-4} = 524.288 counts/Pa$.

a.)

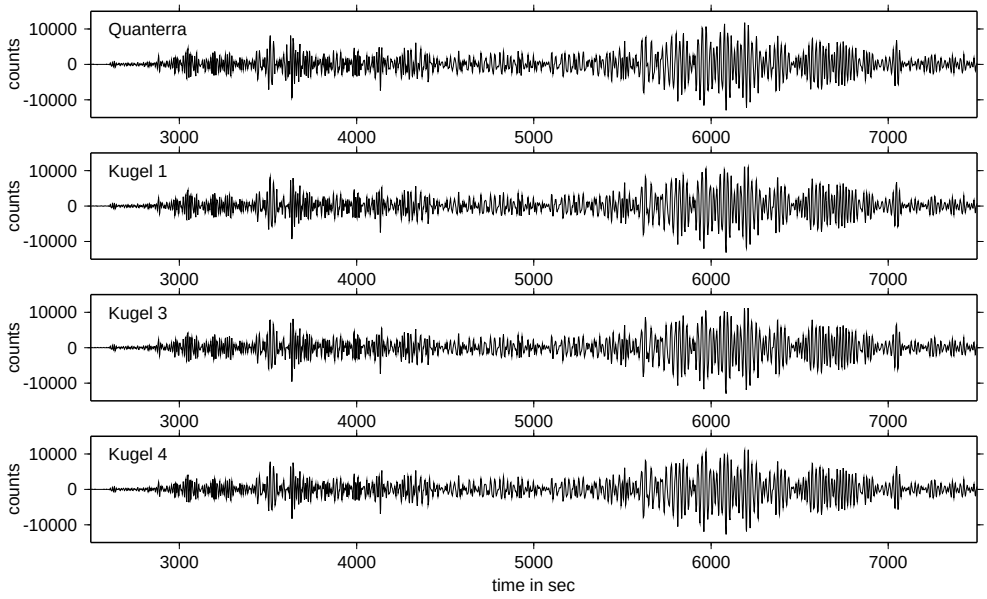

b.)

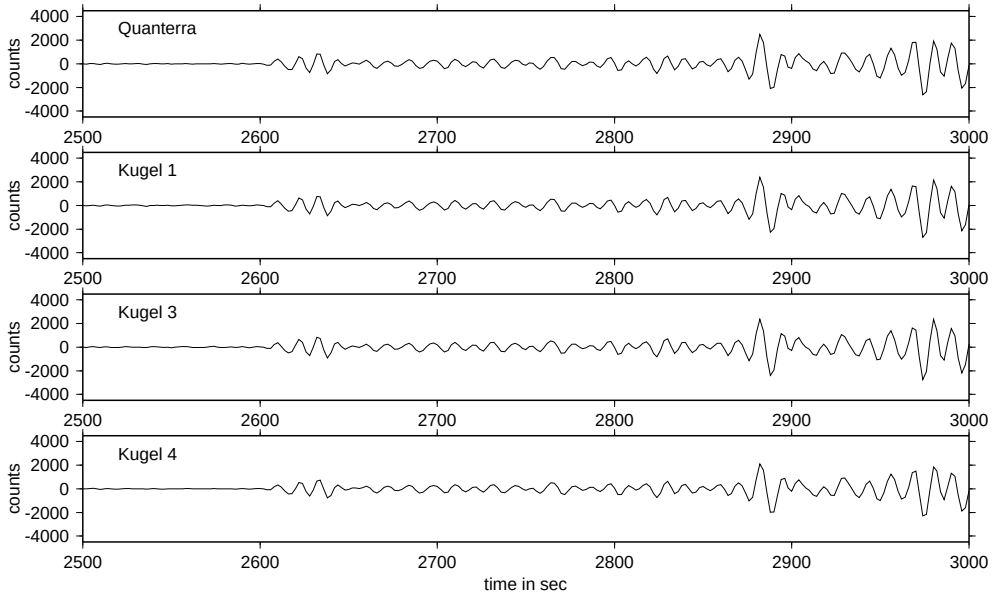

Figure B.2: Traces of the vertical component for the 19.10.2001, M=7.4 earthquake. Time scale since 2 o'clock GMT.

a.) big time window of 5000 s

b.) small time window (500 s) around the P-phase

a.)

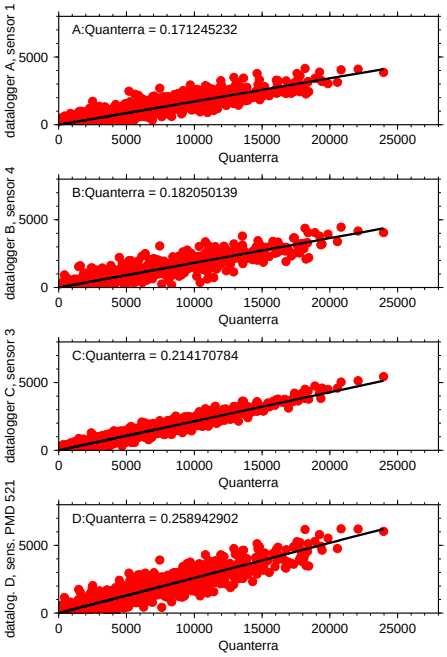

b.)

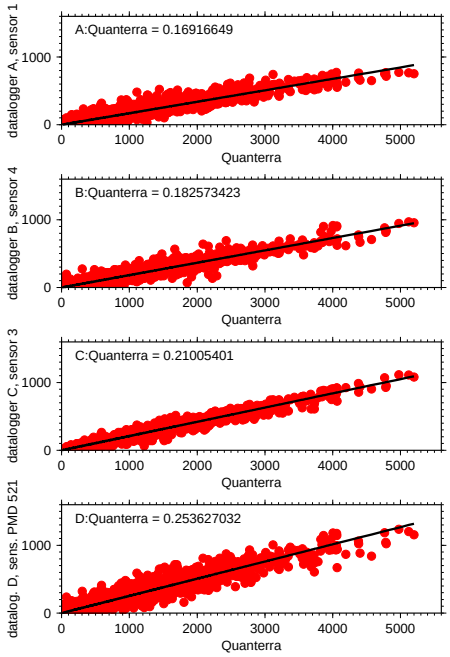

c.)

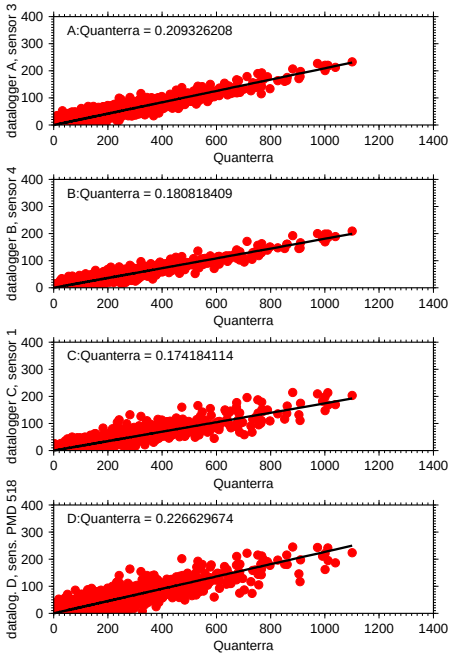

Figure B.3:
The absolute value of the horizontal ground motion recorded on the PMD seismometers are plotted against the absolute value of the horizontal ground motion recorded on the STS-2 seismometer for the 3 events.
Relative sensitivity of the PMD seismometer are written in the upper left corner.

Appendix C

Pole-zero-files

C.1 OBS station of Hamburg

C.1.1 OAS hydrophone

```
# pole-zero-file pressure
# gain factor: (counts / PA)
# pole and zeros in  Laplace domain
#
# data logger preamplifier sensor
2.09716E+5, 20.0, 2.5E-4
1
0.  0.
1
-20.0     0.
```

C.1.2 PMD seismometer

Table C.1: Sensor sensitivity are listed for each station.

Station	vertical	horizontal
OB08	0.121568065E+9	0.126710200E+9
OB10	0.079562182E+9	0.109088394E+9
OB11	0.099882575E+9	0.102919167E+9

Poles and zeros are given in Laplace domain $s_i = 2\pi i \cdot f_i$. The sensor sensitivity out of table C.1 replaces the space-holder "xxxxx" in line 6 of the pole-zero-file.

```
# pole-zero file acceleration
# poles and zeros from PMD sheet in Laplace domain
# gain factor: ( counts/ (m/s) )
#
# sensor   preamplifier  data logger
xxxxx, 1.0, 1.39055375E+13
4
0.  0.
0.  0.
0.  0.
0.  0.
10
0.  0.
-512.242371     -631.10199
-512.242371      631.10199
-238.832672        0.
-134.431259     -264.552277
-134.431259      264.552277
  -0.0730659068   -0.0516599752
  -0.0730659068    0.0516599752
  -0.0142858271   -0.0177966207
  -0.0142858271    0.0177966207
```

Appendix D

Seismicity

D.1 Local seismicity

Following events occurred during deployment and are relocated by Andreas Wittwer using the combined ocean bottom and land station data (Wittwer, 2004).

Table D.1: Local seismicity

date	time	Lat.	Lon.	depth	comments
2000-12-02	12:09:22.337	38.563	14.001	9.38	
2000-12-03	17:00:11.805	39.181	15.416	9.79	
2000-12-04	12:13:10.130	39.336	15.754	219.79	
2000-12-04	19:04:34.747	39.415	15.949	0.40	
2000-12-05	14:11:07.488	38.534	13.955	0.00	Fixed
2000-12-07	09:05:01.041	38.275	15.508	83.58	
2000-12-07	20:36:20.738	38.615	15.789	155.67	
2000-12-09	13:52:38.742	39.215	16.049	4.57	
2000-12-09	23:49:12.726	38.701	13.293	14.54	Fixed
2000-12-10	04:53:14.661	38.321	15.508	120.84	
2000-12-10	06:17:56.703	39.582	15.340	4.95	
2001-01-01	20:30:02.007	38.889	15.944	8.77	
2001-01-02	21:41:04.496	38.292	15.337	149.90	
2001-01-04	23:20:59.219	38.714	14.933	312.37	
2001-01-07	07:26:28.966	39.232	16.032	58.56	
2001-01-07	23:51:30.241	38.453	15.791	35.74	
2001-01-08	15:33:18.749	37.995	14.933	48.33	
2001-01-09	03:51:58.342	37.619	15.105	0.00	Fixed
2001-01-09	19:17:04.392	38.746	14.867	292.79	

2001-01-12	00:06:07.290	38.750	15.510	9.14	
2001-01-12	08:47:54.212	38.146	15.721	3.47	
2001-01-20	02:34:47.578	38.833	15.272	260.49	
2001-01-20	15:54:37.976	38.431	15.542	131.80	
2001-01-23	16:06:44.029	38.564	13.960	6.03	
2001-01-24	01:07:51.598	38.630	13.953	0.00	Fixed
2001-01-24	13:51:17.320	37.818	15.133	48.35	Fixed
2001-01-26	11:04:22.228	37.733	14.971	60.77	
2001-01-26	11:44:27.508	37.891	14.953	0.00	Fixed
2001-02-12	08:59:29.461	37.990	14.136	1.06	
2001-02-14	20:46:27.000	38.821	15.408	154.61	
2001-02-14	23:19:29.756	38.429	13.522	21.02	
2001-02-15	09:32:39.880	37.834	13.828	8.33	
2001-02-18	21:29:53.732	38.646	15.700	165.60	
2001-02-18	23:02:49.480	38.271	16.036	12.74	
2001-02-21	05:27:51.873	38.534	14.794	11.16	
2001-02-21	06:12:47.190	38.442	14.873	12.79	
2001-03-03	00:47:25.678	38.757	15.836	104.68	
2001-03-07	18:20:27.038	37.983	14.862	11.29	
2001-03-10	09:16:52.481	38.199	15.044	3.64	
2001-03-10	14:23:29.769	39.148	15.978	15.45	
2001-03-12	23:46:22.628	39.487	14.449	1.59	Fixed
2001-03-15	07:35:24.242	37.841	15.654	13.17	
2001-03-15	08:48:28.279	37.817	14.987	0.00	Fixed
2001-03-15	10:22:00.972	37.719	14.910	8.55	
2001-03-21	09:08:53.811	38.523	15.984	2.34	
2001-03-25	07:05:32.763	37.769	15.107	0.00	Fixed
2001-03-25	16:19:35.547	38.087	15.134	0.00	Fixed
2001-03-26	18:40:33.473	38.156	15.390	28.82	
2001-03-26	18:44:37.801	38.071	15.306	4.28	
2001-03-26	19:08:32.449	38.081	15.321	30.71	
2001-03-27	02:12:16.500	38.282	15.227	140.93	
2001-03-27	19:14:31.507	38.143	15.443	25.78	
2001-03-27	21:43:33.680	38.128	15.314	10.16	
2001-03-27	23:18:56.444	38.118	15.319	30.75	
2001-03-28	01:09:44.185	38.128	15.359	18.28	
2001-03-28	03:32:13.019	38.009	15.293	34.86	
2001-03-28	05:18:54.113	38.114	15.327	21.81	
2001-03-28	05:47:26.511	38.166	15.381	19.27	

2001-03-28	07:03:17.065	38.162	15.378	10.95	
2001-03-28	07:37:59.959	38.206	15.364	0.10	
2001-03-28	17:32:38.155	38.303	15.052	134.66	
2001-03-28	19:52:14.610	38.139	15.333	4.22	
2001-03-28	20:00:44.981	38.189	15.349	25.47	
2001-03-29	03:02:46.173	38.093	14.506	0.00	Fixed
2001-03-30	07:48:16.675	38.095	15.398	9.72	
2001-03-30	19:41:11.326	37.626	15.069	0.00	Fixed
2001-04-02	21:08:36.667	39.488	14.440	7.98	
2001-04-04	20:13:46.475	39.528	14.421	0.00	Fixed
2001-04-06	08:52:08.083	37.887	14.890	10.00	Fixed
2001-04-06	11:40:21.641	39.411	15.499	316.95	
2001-04-07	12:55:00.770	38.240	15.218	101.28	
2001-04-10	15:56:18.572	39.227	15.989	12.53	
2001-04-16	02:31:01.651	38.611	14.616	201.09	Fixed
2001-04-16	13:24:23.469	37.558	14.932	0.00	Fixed
2001-04-16	14:58:39.508	38.130	14.467	0.00	Fixed
2001-04-18	05:07:38.891	38.313	15.428	117.52	
2001-04-24	00:43:46.722	39.251	15.520	4.45	
2001-04-28	13:41:15.015	37.811	15.011	10.00	Fixed
2001-04-29	21:00:19.737	37.730	14.935	0.00	Fixed
2001-04-30	12:40:09.598	38.169	14.292	172.55	
2001-05-02	08:48:23.396	37.678	15.099	5.51	
2001-05-03	01:13:15.854	38.939	14.419	12.36	
2001-05-03	10:52:58.289	38.290	15.400	114.93	
2001-05-04	02:16:00.037	38.544	15.544	152.19	
2001-05-05	03:01:22.864	39.089	15.996	13.03	
2001-05-05	11:19:59.985	39.242	15.503	7.26	
2001-05-08	04:52:59.217	38.190	14.829	2.73	
2001-05-09	01:22:08.963	37.510	15.159	4.72	

The comment "fixed" means that the depth was fixed during the localization. Date and hour are given in MET (Middle European Timezone)

D.2 Teleseismic events

Teleseismic events with a magnitude larger than 6 occurred during the deployment are listed next (NEIC of the U.S. Geological Survey, http://neic.usgs.gov). Normally only events larger 7 are usable:

Table D.2: teleseismic event

date	time	Lat.	Lon.	depth	Magnitude
2000-12-03	12:55:16.70	51.67	-178.16	43	6.00 (ML)
2000-12-04	04:43:09.59	14.88	-93.94	33	6.10 (Mw)
2000-12-06	17:11:06.40	39.57	54.80	30	7.50 (Ms)
2000-12-06	22:57:40.04	-4.22	152.73	31	6.70 (Ms)
2000-12-12	05:26:45.94	6.01	-82.68	10	6.60 (Me)
2000-12-15	16:44:47.66	38.46	31.35	10	6.00 (Mw)
2000-12-18	01:19:21.65	-21.18	-179.12	628	6.70 (Me)
2000-12-19	13:11:47.37	11.77	144.76	33	6.30 (mb)
2000-12-20	11:23:54.10	-39.01	-74.66	11	6.50 (Mw)
2000-12-20	16:49:43.30	-9.23	154.35	33	6.60 (Mw)
2000-12-21	01:01:27.77	-5.71	151.12	33	6.60 (Ms)
2000-12-21	02:41:23.13	-5.35	154.13	386	6.00 (Mw)
2000-12-22	10:13:01.11	44.79	147.20	140	6.30 (Me)
2000-12-23	07:13:24.30	-7.87	135.82	61	6.00 (Mw)
2000-12-28	04:34:28.45	-4.05	152.31	33	6.20 (Mw)
2001-01-01	06:57:04.17	6.90	126.58	33	7.50 (Mw)
2001-01-01	08:54:31.58	6.63	126.90	33	6.80 (Mw)
2001-01-02	07:30:03.78	6.75	126.81	33	6.40 (Mw)
2001-01-02	23:17:41.97	-11.16	162.44	33	6.00 (Mw)
2001-01-09	16:49: 28	-14.93	167.17	103	7.10 (Mw)
2001-01-10	16:02:44.23	57.08	-153.21	33	7.00 (Mw)
2001-01-11	00:04: 03	48.89	-129.31	10	6.00 (Mw)
2001-01-13	17:33:32.38	13.05	-88.66	60	7.80 (Ms)
2001-01-15	05:52:16.25	-40.34	78.36	10	6.40 (Mw)
2001-01-16	13:25:01.08	-3.96	101.75	33	6.00 (mb)
2001-01-16	13:25:09.83	-4.02	101.78	28	6.90 (Mw)
2001-01-19	01:12:52.08	15.40	-92.72	93	6.00 (Mw)
2001-01-19	08:10:14.75	-11.66	166.38	50	6.30 (Mw)
2001-01-19	09:04:34.56	-58.16	-9.47	33	6.00 (Mw)
2001-01-26	03:16:40.50	23.42	70.23	16	8.00 (Ms)
2001-01-29	23:21:25.94	-0.68	133.33	33	6.20 (Mw)

2001-02-01	18:19:30.39	51.44	-177.80	33	6.00 (Mw)
2001-02-13	14:22:05.82	13.67	-88.94	10	6.60 (Mw)
2001-02-13	19:28:30.26	-4.68	102.56	36	7.40 (Mw)
2001-02-14	14:04:25.61	-19.49	177.33	10	6.10 (Mw)
2001-02-14	14:16:59.18	-19.69	177.39	10	6.20 (Mw)
2001-02-16	05:59:09.48	-7.16	117.49	521	6.10 (Mw)
2001-02-17	20:11: 30	53.92	-133.61	20	6.20 (Mw)
2001-02-18	13:04:53.42	-47.46	32.39	10	6.00 (Mw)
2001-02-24	07:23:48.73	1.27	126.25	35	7.10 (Mw)
2001-02-24	16:33:44.68	1.55	126.43	33	6.20 (Mw)
2001-02-25	02:21:59.59	36.42	70.88	202	6.20 (Mw)
2001-02-26	05:58:22.43	46.81	144.52	392	6.10 (Mw)
2001-02-28	12:30:14.05	-21.99	170.21	10	6.70 (Mw)
2001-02-28	13:05:31.64	-22.00	170.11	10	6.30 (Mw)
2001-02-28	18:50:13.02	13.28	-88.83	65	6.10 (Mw)
2001-02-28	18:54:32.83	47.15	-122.73	51	6.80 (Mw)
2001-03-06	09:17:36.08	-54.59	157.27	10	6.40 (Mw)
2001-03-07	18:10:58.65	-6.81	-12.91	10	6.00 (Mw)
2001-03-14	18:56:18.88	0.45	121.89	109	6.00 (Mw)
2001-03-15	01:22:43.37	8.66	94.01	33	6.00 (Mw)
2001-03-15	13:02:42.11	-32.32	-71.49	37	6.10 (mb)
2001-03-19	05:52:15.89	-4.03	128.02	33	6.50 (Ms)
2001-03-23	11:30:10.52	44.07	148.05	33	6.00 (Mw)
2001-03-24	06:27:53.58	34.08	132.53	50	6.80 (Mw)
2001-04-04	07:44:11.20	-5.18	132.37	33	6.40 (Mw)
2001-04-07	23:17:37.92	-27.55	-176.34	33	6.20 (Mw)
2001-04-09	09:00:57.17	-32.67	-73.11	11	6.70 (Mw)
2001-04-13	15:33:53.55	-59.72	-25.59	26	6.20 (Mw)
2001-04-14	23:27:26.66	30.09	141.77	10	6.00 (mb)
2001-04-19	03:13:25.58	-7.45	155.89	12	6.00 (mb)
2001-04-19	20:58:26.14	-7.31	155.96	20	6.20 (Mw)
2001-04-19	21:43:42.28	-7.41	155.87	17	6.70 (Mw)
2001-04-26	17:48:57.47	43.10	145.92	86	6.00 (Mw)
2001-04-28	04:49:53.43	-18.06	-176.94	351	6.90 (Mw)
2001-04-29	21:26:54.54	18.74	-104.54	10	6.20 (Mw)
2001-05-07	00:33:23.80	-56.19	-144.47	10	6.20 (Mw)
2001-05-09	17:38:26.12	-10.32	161.23	67	6.30 (Mw)